Development of microfluidic sensing platforms for microbial contaminants and protocells

Ph.D. Thesis
Mads Clausen Institute
University of Southern Denmark

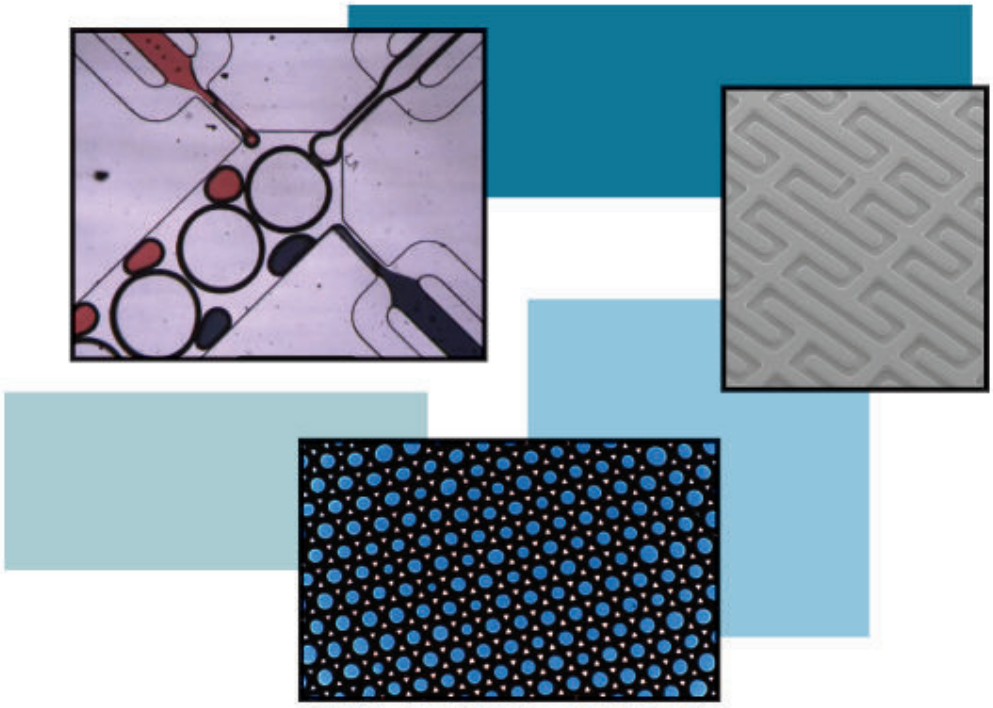

Casper Kunstmann-Olsen

May 1. 2012

Preface

This thesis is part of the requirements for achieving the Ph.D. degree at the University of Southern Denmark (SDU). The main part of this work has been carried out at the Mads Clausen Institute at SDU in Sønderborg, while a smaller part has been performed at SDU in Odense. At the Mads Clausen institute (MCI) I have been working in the NanoSYD group. The Ph.D. project has been supervised by Professor Horst-Günter Rubahn as main supervisor and Dr. James D. Hoyland as project supervisor. Apart from this thesis, a number of other publications has also been made during this project; these are listed in appendix A.

I have been working together with some collaborative groups, to whom I owe thanks. These are Steen Rasmussen and his group *FLiNT* at Department of Physics, Chemistry and Pharmacy, SDU in Odense and Helmut Erdmann and his group from Flensburg University of Applied Sciences, Germany.

The project has been partially financed by the Europena Regional Development Fond through the INTERREG 4-A program Syddanmark-Schleswig-K.E.R.N.

I would like to acknowledge several people for their support during this project. In particular a special thanks goes to Horst-Günter Rubahn for his help, support and assistance on several aspects. I would also like to thank my colleagues at NanoSYD for their help and kindness along the way. Ideas and creative solutions to scientific problems often come along more informal discussions within a group, this I have experienced personally during this project. A special thanks to James Hoyland for help and advice on a number of different aspects. Furthermore, I would like to thank Martin Hanczyc for support and discussions regarding the protocell aspects of the project. Also, a special thanks to Ralf Frese who was an immense help during the first year of the project.
Additionally, a special thanks to my girlfriend Lauren, without whose support and encouragement this work would not have been possible. Finally, I would like to dedicate this thesis to my parents, who have always been there for me and supported me every step of the way.

Casper Kunstmann-Olsen

Abstract

This thesis is focused on the development of a microfluidic lab-on-a-chip (LOC) sensing platform. Polymer (PDMS) LOC devices can be realized by direct replication of a micro-structured SU8 master that is created using custom made photonegative masks. This is done using photolithography (a classic clean room top-down technique). The LOC devices are interfaced using a novel chip-chuck interconnection method, while fibers are used to excite and detect optical signals.

The LOC device is connected to a setup capable of controlling microfluidic flows, exciting fluorescence by laser light, whilst detecting and measuring both fluorescent and scattered events using optoelectronic devices connected to a PC.

Optical detection methods, such as flow cytometry (FCM), has proven to be a fast and powerful tool in characterizing large biological samples, which can be especially useful with regards to food contamination and environmental monitoring. In this project, the FCM method is applied to the microfluidic LOC devices to develop a sensing platform capable of detecting small quantities of micro-organisms in large biological samples. Detection of both artificial samples (polymer beads) as well as Baker's yeast and listeria is demonstrated successfully. It is believed that this method, with some improvements, can be adapted for use in a wide range of manufacturing and processing industries.

The developed microfluidic LOC platform is also applied to investigations into protocells. Protocells are artificial non-biological life-like systems consisting of a minimum amount of simple chemical components [1]. In this thesis, oil droplet systems containing fatty acids are used as simple models for protocells. Implementing a full protocell life cycle in to a LOC device, in combination with a detection and sorting system would enable a range of interesting investigations.

By utilizing the unique flow conditions in the microfluidic devices, formation of mono-disperse oil droplets are established. Droplet fusion is presented as a simple method of delivering resources to the system. This is realized by destabilizing droplets in narrow channels and forcing them to fuse on contact. Droplet splitting is demonstrated using a simple T-junction structure, where a cross-flow shears elongated droplets into smaller elements. Droplet sorting is demonstrated in a simple y-shaped micro-channel structure, while the developed FCM LOC device can be used to distinguish droplet populations by fluorescence. All of these elements can now, with minor improvements, be implemented into a multicomponent LOC system that enables studies of protocell development.

Dansk Resume

Denne afhandling fokuserer på udviklingen af en mikrofluid lab-on-a-chip (LOC) sensorplatform. Polymer (PDMS) LOC enheder kan fremstilles ved direkte replikation af en mikrostruktureret SU8 form, som er fremstillet ud fra brugerdefinerede fotonegativ masker. Dette gøres vha. fotolitografi, som er en klassisk renrum top-down mønsteroverførsels-teknik. LOC elementerne forbindes vha. en unik *chip-chuck* metode, mens optiske fibre bruges til at excitere og detektere optiske signaler.
LOC enheden tilsluttes en opstilling, som er i stand til at kontrollere mikrofluide flows og excitere fluorescens vha. laser, mens detektion og måling af fluorescens og spredt lys foretages af optoelektroniske apparater, der er tilsluttet en PC.
Optiske detektionsmetoder, såsom flow cytometri (FCM), har vist sig at være et hurtig og nyttigt redskab til karakterisering af biologiske prøver, hvilket kan være specielt brugbart med hensyn til madforgiftning og miljøovervågning. I dette projekt bliver FCM anvendt på de mikrofluide LOC enheder, for at udvikle en sensorplatform, som er i stand til at detektere små mængder mikroorganismer i store mængder biologiske prøver. Karakterisering af både kunstige prøver (polymer kugler), samt gærceller og listeria (bakterier) er demonstreret med succes. Det forventes at denne metode, med visse forbedringer, kan tilpasses til brug i en lang række fremstillings- og behandlingsmetoder i fødevareindustrien.
Den udviklede LOC platform er også anvendt til undersøgelse af såkaldte protoceller. Protoceller er kunstige, ikke-biologiske livs-lignende systemer, som består et minimum af simple kemiske komponenter [1]. I denne afhandling bliver oliedråbe-systemer indeholdende fedtsyrer brugt som modelsystem for protoceller. Fuld implementering af en protocelles livscyklus, kombineret med optisk detektion og et sorteringssystem, kan åbne op for en række spændende undersøgelsesmuligheder.
Ved brug af de unikke flow-betingelser i den mikrofluide chip kan oliedråber med meget lav størrelsesfordeling fremstilles. Fusion af dråber præsenteres som en simpel metode til at overføre ressourcer til systemet. Dette er realiseret ved at destabilisere dråberne i en snæver kanal og tvinge dem til at fusionere ved kontakt. Delingen af dråber er demonstreret ved brug af en simpel T-formet struktur, hvor tværgående flows deler langstrakte dråber i mindre enheder. Sortering af dråberne er demonstreret i en simpel y-formet mikrokanal-struktur, mens den udviklede LOC sensorplatform kan bruges til at skelne dråbebestande vha. fluorescens. Alle disse elementer kan nu, med mindre forbedringer, implementeres i et multikomponent-system, hvilket muliggør undersøgelser af protocellers udvikling.

Contents

Chapter 1

Introduction

1.1 Lab-on-a-Chip Systems

Throughout the last century miniaturization has played a crucial role in modern technology and revolutionized society. Great advances has been made in both technology (micro- and nanotechnology), but also within the fields of biology and chemistry, where improvements in optical systems has opened a world of new possibilities.
Advances in top-down fabrication using photolithography and similar methods has made it the standard for fabrication of microelectronics and integrated circuits. Which has had a huge impact on the computer and electronics industry, starting with the invention of the transistor at Bell labs in 1947 [2].
The continued success of microelectronics can be attributed to a combination of miniaturization and integration of complex functions. While the driving force for continued downscaling has often been the desire to increase computational capacity (as predicted by Moore's Law [3]), a wide range of other disciplines has also benefited from these advances, such as MEMS (micro-electro-mechanical systems) or optical systems that uses microstructures to manipulate light.
In 1979 S.C. Terry *et al.* presented *A Gas Chromatographic Air Analyzer Fabricated on a Silicon Wafer* [4], which was the first publication discussing the use of techniques borrowed from the microelectronics industry for chemical analysis. In 1990 Manz *et al.* introduced the concept of micro total-analysis systems (μTAS) [5], which triggered a rapidly growing interest for the development of microsystems in which all stages of chemical analysis could be performed (preparation, reactions, separation, detection and data analysis), in an integrated and automated fashion. Devices that are able to perform

all of these advanced and complex steps are also often referred to as lab-on-a-chip (LOC) devices, as they integrate a number of classic laboratory functions into an integrated chip (see figure 1.1 for an example).
The main reason LOC systems triggered such a great interest some 20 years ago, is found in the increasing number of demands on conventional chemical analysis. This is driven by the rapid development and growing interest in e.g. medicine, drug delivery, biotechnology, environmental monitoring etc. And has in turn spurred a movement towards decentralization of chemical analysis that puts large demands on analyzing equipment to be easier to use for non-experts, cheaper to produce and give faster results. In the extreme case, the LOC device can be regarded as a black box, where the user simply needs to apply the sample, press a button to start the analysis and receive the results.
Central to all μTAS is the microchip itself, which through the advances in microfabrication can be tailored and designed to function in a wide range of applications. On these chips, tiny volumes of samples are handled and can be moved around very precisely using microfluidics. This is one of the key advantages of LOC systems over traditional analysis methods, as handling of small sample volumes often means a dramatic reduction in cost. Furthermore, once a μTAS method has been developed, the sheer size of the LOC devices makes reproduction and manufacturing in large numbers easier, that in turn enables parallelization of analytical investigations. This is extremely useful in drug-screening and medical production where thousands of samples have to be tested against each other (known as high throughput screening - HTS) [6].

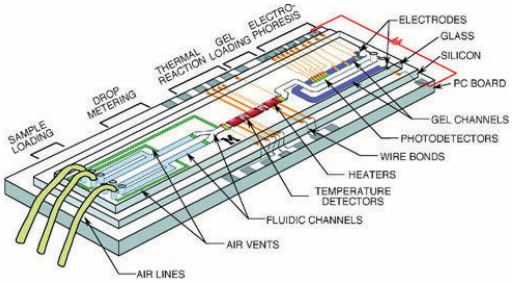

Figure 1.1: Example of advanced LOC device containing numerous lab functions. From [7].

For production of LOC devices, a wide range of methods are available, most of which are based microelectronics production schemes. Furthermore, a range of different materials can be used, all of which have certain advantages and

limitations. The right choice in production method and material is highly application dependent.
Generally LOC devices are made of either silicon, glass or polymers. Silicon has the obvious advantage of extensive processing knowledge from the semiconductor industry, while glass substrates maintain some of the same advantages as Si (first of all chemical inactivity), but also has obvious optical advantages over silicon. Glass substrates are however harder to process and require either mechanical methods (blasting or milling) or high energy optical methods (laser ablation) [8].
Polymer substrates are often better suited for LOC devices and have some major advantages in terms of processing compared to both Si and glass substrates. Polymer structures can be mass produced at a significantly lower cost and comes in various types and shapes, offering a wide range of options in terms of mechanical, optical, chemical and thermal properties [8].

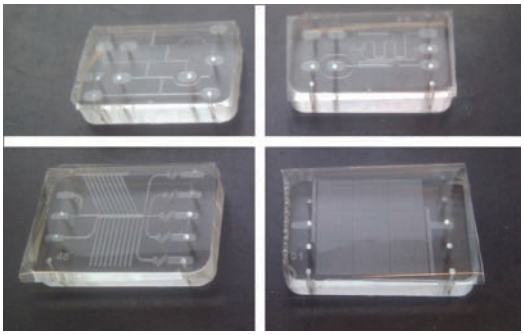

Figure 1.2: Four polymer (PDMS) chips with various microfluidic structures.

Elastomer based polymers, especially poly(dimethylsiloxane) (PDMS), have been widely used in the scientific community for experimental microfluidics since G.M. Whiteside's group at Harvard developed a simple replication production method in the mid 1990's [9]. The method can be directly adapted for photolithography and is a simple master-replication technique. This enables rapid prototyping, as a single master structure can be used for multiple replications in a short period of time.
PDMS has a number of features that makes it unique and well suited for a range of different applications. PMDS is flexible, but still mechanically strong with a typical Young's modulus of around $0.75GPa$, compared to values of $1 - 5GPa$ for most other typically used polymers [10]. This is caused by longer bond lengths and wider bond angles of the $Si - O - Si$, compared to $C - C - C$ or $C - O - C$, which most organic polymers consist of [10]. This means that PDMS conforms well to surfaces, forms tight seals around

inlets and is easy to release from molds [11].
Furthermore, PDMS is optically transparent from $230nm$ to $700nm$ [12], which makes it a good candidate for LOC systems utilizing optics. PDMS is impermeable to water, nontoxic to biological samples and permeable to gases [13]. PDMS also has low solubility (little or no swelling) with most alcohols and sulfoxids (like DMSO) [14]. Investigations also show that very little unlinked PDMS (oligomers) dissolves in contact with organic solvents (less than 0.05%) [14]. Finally, PDMS is very hydrophobic, which prevents wetting of aqueous solutions [9]. Figure 1.2 shows four PDMS microfluidic chips with a range of different microfluidic structures.

Contribution

The first part of the work presented in this thesis will be concerned with creating a fast, flexible and reliable production scheme for PDMS microfluidic LOC systems. It is desired to establish a LOC platform that enables a wide variety of experimental work concerned with any possible fields that can benefit from microfluidic integration.

1.2 Flow Cytometry

Advances in the field of optics has always pushed for the limits for the observable, ever since the first optical systems some 3000 years ago. By the early 20'th century microscopes were so developed that microscopic biological samples, cells and bacteria were detectable for the first time. This happened with the invention of the ultramicroscope in 1903 that enabled observation of objects close to the wavelength of visible light [15].
It is, however, mostly desirable to see these microorganisms in their natural aqueous environment, which can be difficult in static microscopy. The invention of flow cytometry (FCM) changed this, and is generally attributed to A. Moldovan who in 1934 published a paper entitled *Photo-Electric Technique for the counting of microscopical cells*. Here a simple setup was proposed where a microscope was connected to a photo-electric counter and focused on a thin glass capillary in which suspended sample (red blood cells) were forced through using pressurized air [16].
Since then a lot has happened with the technology, but the fundamental idea remains the same. Flow cytometry is an optical method for characterizing mainly biological samples based on their optical signature, as measured while being cycled through the system in suspension [17]. The basic principle of a modern flow cytometer is shown in figure 1.3 and draws on both fluid dy-

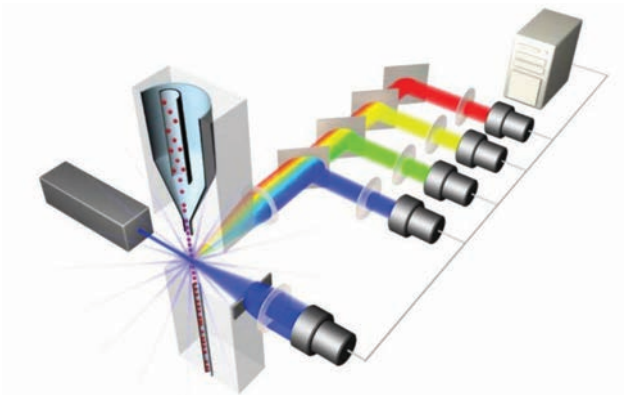

Figure 1.3: Schematic drawing showing the basic principle of flow cytometry.

namics, optics and electronics.
The principle of operation will be discussed in more detail later, but in essence, flow cytometry is a high throughput flow-through optical detection method. Suspended biological samples are focused into a narrow stream using a flow nozzle and then passed through the optical detection area, ideally one sample at a time, like beads on a string. In the measurement volume the samples interact with one or several focused lasers, which excites fluorescence and is furthermore scattered by the sample itself [17]. Both fluorescence and and scattered light are then optically filtered (using dichroic filters) and each light channel detected individually using photomultipliers (PMTs). The filter block uses a row of dichroic mirrors, each filtering a certain wavelength range out, making the whole setup act as a crude spectrometer. Signal intensities are saved for each event, creating multidimensional data-structures of the overall sample. By plotting various optical channels against each other in a *scatter plot*, samples can be distinguished based on a number of different inputs (size, composition, viability, fluorescent markers etc.) [17].

One of the main advantages of creating LOC flow cytometry devices, apart from the obvious reduction of samples sizes, is device integration. The amount of integration depends highly of the level of sophistication of the LOC device, but potentially everything from flow elements (pumps, valves etc.), optics (lasers, photo diodes etc.) and electronics (integrated circuits) can be implemented into microfluidic devices [18].
Simple sample handling is done easily on-chip by utilizing laminar flows and hydrodynamic focusing [19], but more advanced sample processing steps can also be integrated. These include chemical reactors, mixers, diluters and sorting mechanisms which create highly advanced LOC systems that can handle

samples directly from raw specimen to finished data [18]. By developing multiflow devices, LOC systems can also be used for automated processes such as cell staining, enrichment etc. [18].
Finally, using microelectronic processing, the LOC device can be interfaced with systems of similar scale, such as integrated electronics or planar optics that utilizes optical fibers, waveguides or even surface plasmonic structures [18].
In times where public health and environmental awareness is becoming an increasingly important matter, the flow cytometer has become one of the major tools in the fight against dangerous microorganisms and bacterial contaminants [20]. The ability to process large sample numbers (at rates up to $100kHz$) with high precision and a wide range of experimental parameters makes FCM a serious competitor to traditional dish cultures in a period where time is money and speed is everything. Combined with lower production costs and increased mobility offered by modern integrated LOC systems, flow cytometric methods are looking to become an integral part of every major food and consumer product production line [21].

Contribution

In the second part of this thesis work, microfluidics platforms are used as a starting point for development of LOC flow cytometric devices. To realize this, an optical detection system is established and optimized for fluorescent signals. To understand and control samples behavior in the LOC devices, fluid dynamics and hydrodynamic focusing is investigated in detail. Finally, the microfluidic flow cytometry system is used to conduct measurements on both artificial and biological samples with the goal of identifying potential contaminants in large sample volumes by fluorescent staining.

1.3 Protocell

The big question about life, is not one easily answered, and yet scientists have struggled with the basic mystery of existence for millenia. On the blackboard of Nobel price winning physicist Richard Feynman, the words *what I cannot create, I do not understand* was found after his death in 1988 [22]. This line of thought is today one of the leading catalysts in modern synthetic biology where the hunt to understand life has become a quest to create life.
Protocell directly translated means *first cell*, but instead of taking the term literally as is done in *Origin of life* studies, the protocell is rather a reinvention of the first cell, the most simple cell, constructed by a bottom-up

approach from simple chemical components [1]. These elements are all non-biological and are individually well understood. The basic protocell has three main constituents that all interact via physical and chemical interactions in a complex thermodynamical cycle, the protocell life cycle. The three categorical components of the protocell are *container*, *information* and *metabolism*. These components are combined by a large variety of complex chemical and physical pathways [1].
As any thermodynamical system, the protocell draws energy from the outside, while at the same time being dependent on addition of certain resources (nutrients) [23]. The continued intake of energy and resources allows the protocell to grow and divide. Figure 1.4 show a concrete protocell life cycle (proposed by Rasmussen *et al.* [1]).

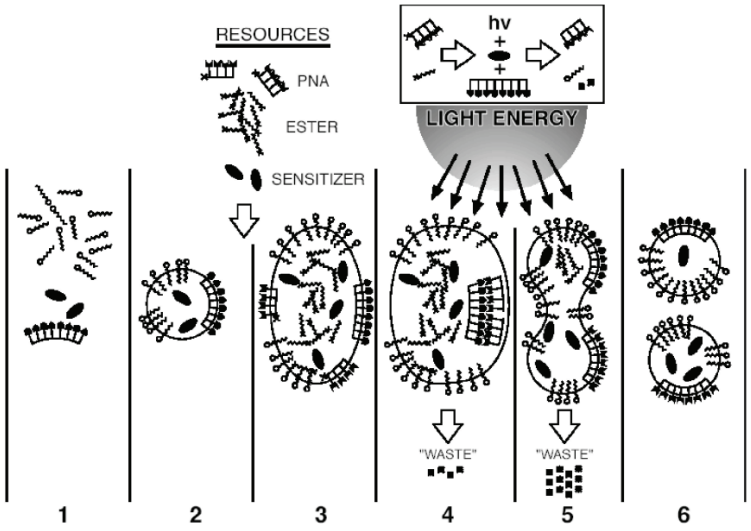

Figure 1.4: Suggested protocell life cycle, beginning with self-assembly of components (1-2), addition of resources (3), addition of optical energy that drives metabolism (4-5) and finally division (6). From [1].

Protocell development can however be taken a step further and not only mimic minimal living systems in function, but also in behavior. Fatty acid vesicles and oil droplets can be made to mimic simple interactions of living cells, such as growth and division [24] or movement [25].
In general, oil droplets or vesicles consisting of fatty acid systems make interesting protocell containers as fatty acids can be synthesized in the metabolism (see figure 1.4). Learning to manipulate these structures physically and chemically can go a long way in terms of fulfilling a complete protocell life cycle and understand the underlying mechanics.
Figure 1.5 shows a schematic drawing of a possible microfluidic LOC imple-

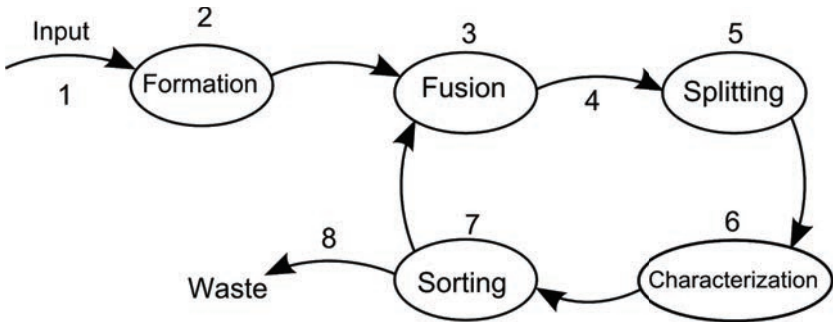

Figure 1.5: Concept showing possible protocell life cycle.

mentation of the protocell life cycle The desired protocell components (1) are added to the system and droplets are formed (2). These can be fused (3) together with other droplet populations containing resources. Protocell growth (4) can now occur (induced thermally, optically or by other means). Larger droplets can be split (5), and characterized (6), for instance with the flow cytometry setup. Based on characterization output, droplets can then be sorted (7) according to certain parameters, and either be discarded (8), or re-introduced into the cycle where the process can start again.

Contribution

The final part of this thesis is concerned with using the established microfluidic PDMS devices as a platform to create and manipulate (fuse, split and sort) microscopic fatty acid based oil droplets, which serve as model systems and containers for more advanced protocells. The use of microfluidics offer precise control over a wide range of chemical and physical parameters and therefore enables interesting effects not observable in dish experiments. Lastly, the optical detection setup established in the FCM part can be applied to a population of oil droplets and the outcome used to distinguish these (based on fluorescence). These results can serve as interesting first step in an integrated feedback controlled life cycle scheme.

Chapter 2

LOC Development

In this chapter the LOC development process is presented and discussed, along with optical optimization initiatives The entire experimental setup will furthermore also be presented.
The aim of the LOC development process is to create a flexible and fast production method for the microfluidic PDMS chips. First, a novel photo-lithographic mask production is discussed, followed by a detailed step-by-step description of the remaining elements required to produce the microfluidic chips. After production, the chip is interfaced and integrated with the remaining setup. This is achieved with the novel *chip-chuck* device.
In the second section the optical detection setup is presented. This includes a discussion about optimization of collected light via different means, along with a presentation of the optical and experimental setup.

2.1 Microfluidic Device Production

2.1.1 Photonegative Masks

A novel method has been developed for creating fast, cheap and flexible photo-lithography masks. These masks are used in a clean-room process that produces SU8 masters used for replication molding of PDMS. Contact-mask photolithography is able to produce excellent high-resolution structures in various types of resists, on an assortment of different wafer materials [26]. However, microfluidic devices rarely have structures in the sub-micron range and for many applications, channel dimensions of the order of tens or hundreds μm are sufficient [8]. This also applies to the applications in this project, and so the demands on the photo-lithographic masks are more lenient.

Standard procedures for creating masks involves preparing a chromium plated fused silica mask and exposing a SU8 coated substrate with UV-light through the mask. Properly optimized, this technique can produce superb high-aspect ratio (over 1 : 10) SU8 structures with smooth, vertical side-walls [27]. However, the preparation of the masks is itself a rather specialist task beyond the capabilities of many institutions. Furthermore, they are rather expensive and take considerable time to prepare. This greatly affects the flexibility and speed of the microfluidic chips production.

Photographic films

As an alternative, conventional black and white photographic negative films are used as contact masks for photolithography. These black and white films consist of silver halide particles embedded in an organic matrix on a polymer substrate. Development of the film causes silver halide crystals exposed to light to reduce to metallic silver particles. Further chemical treatment (*fixing*), causes unexposed halides to dissolve. The silver particles are of the order of $200 - 600nm$ and are generally distributed randomly throughout the thickness of the emulsion layer. The random distribution of the particles gives rise to varying optical density over the surface and visual "grain" [28]. Film sensitivity is rated by an ISO speed. Whether a silver halide particle turns to metallic silver during development or not is somewhat independent of the grain size. Lower speed film generally has a high density of smaller grains giving greater resolution, but requiring more light to expose. The resolution of these analogue films remain far above modern digital cameras and line-widths of a few μm are theoretically obtainable [28]. It is therefore possible to use negatives as contact masks, provided the optical properties of the films are suitable at the UV wavelengths used in SU8 development [27].

Film investigations

In order to create the optimal mask, three commercially available monochrome films are investigated. Two distinct features are of interest for creating the best mask; contrast and resolution.
The three investigated films are Agfa Copex Rapid *(AGFA)*, Bluefire Police *(BF)* and Rollei ATP *(Rollei)*, which are all sold as high-resolution low speed films. Film contrast and resolution is strongly dependent on the developer, therefore several different developers are also used. Bluefire Micro Developer *(MD)* is designed for *BF* and is a hydroquinone based microfilm developer. *Rollei DC* is a 'document reproduction' developer and *SPUR Modular UR*

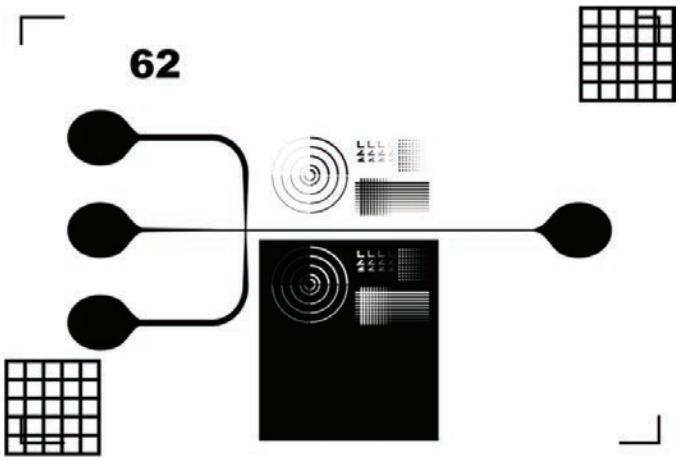

Figure 2.1: Mask design 62. Used for testing photo negative quality. Contains flow focusing channels and various geometric structures of size down to $10\mu m$.

(SPUR) is a general high-resolution developer. Finally, Ilford Microphen *(MP)* is also a popular high resolution developer. Based on manufacturer's data-sheets, six combinations of film and developer are selected and tested. For film investigation and comparison, a test structure is defined (see figure 2.1), using a commercial vector-graphics program *(CorelDraw 11)*. The image is printed on $A1$ sized paper with a resolution of $1200dpi$ using an *HP DesignJet T1100* printer. At this resolution and paper size the printer pixels are considerably smaller than the resolution of the camera and any of the films. The design includes a simple microfluidic flow focusing structure as well as a number of test structures including reticles, grid lines, angles and dots of various sizes down to $10\mu m$ [29].

As the best negatives are to be used as a contact mask, the design needs to be correctly scaled onto the film. The structure is designed to fill a full frame of the standard $35mm$ film ($36mm \times 24mm$). Alignment grids are prepared in the corners of the film to determine the correct positioning of the image within the camera viewfinder. A range of pictures are taken using different grid lines and the resulting negatives measured in a microscope. The alignment mark producing dimensions closest to the design size of the structures are then used for the actual experiments [29].
The pictures were taken using a *Pentax MZ30 SLR* camera with a $80mm$ zoom lens in telephoto mode. The camera is mounted on a tripod and pictures are taken with a delay shutter to reduce camera-shake. The printed design is photographed under controlled lighting at a range of exposures, from 2 stops below to 3 stops above the level determined by the camera's

internal light meter for correct exposure.
The exposed film is developed in a clean-room environment, ensuring stable temperature and humidity conditions. These films are developed according to the manufactures specifications for the given films and developers. The films are first submerged in the developing agent for $5 - 12min$ and then replaced by an acidic stop bath *(Ilfostop)* which terminates the development process. Finally the negatives are placed in a fixing agent *(Ilford Rapid Fixer)* that removes the unexposed halides.

Film Contrast

To determine film contrast transmission measurements on the negatives are made. This is done at $365nm$, the standard photolithographic exposure wavelength, in an optical microscope *(Nikon Eclipse ME600)* equipped with a Hg-lamp and spectrometer *(OceanOptics Maya 2000 Pro)*. All measurements are averaged over 5 scans and obtained during a $13ms$ integration window. For each individual film the intensities are normalized with respect to the lamp intensity at $365nm$. Transmission is measured in both clear and dark areas of the negatives and used to calculate the contrast.
The transmission of both clear (T_{clear}) and dark areas (T_{dark}) of the mask design are obtained for all six different films, and for all possible light exposures (-2 to 3) [29]. These are plotted in figure 2.2. A big variation is

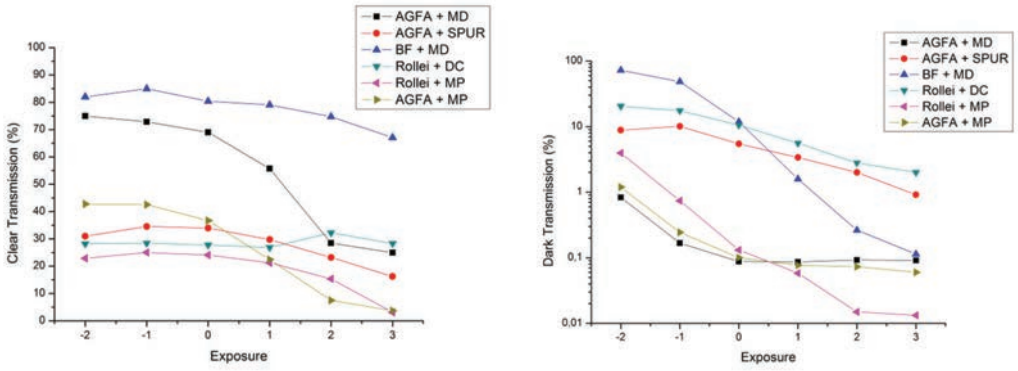

Figure 2.2: Transmission of photo negatives for clear *(left)* and dark *(right)* areas for all six combinations of films and developers.

obvious for T_{clear}. Most film combinations show a fairly stable transmission versus different exposures, while the *AGFA+MD* and *AGFA+MP* show a stronger dependency. All combinations do however show decreasing transmission with increasing light exposure. This is to be expected since more

light (longer opening times of the camera's aperture) will reduce more silver halide crystals in the film, resulting in more silver crystals. The transmission of the film is also a function of other factors; the two most important being the transmission of the substrate polymer itself, and the development procedure.
While the UV-transmission of the polymer is an inherent property, the developer clearly has a big influence as well. Comparing the three *AGFA* film combinations there is up to 40% difference, which is attributed to the developer. This indicates that the *SPUR* and *MP* developer has overdeveloped the film, resulting in a higher fraction of silver halide particles being turned in silver crystals. This also accounts for the difference between the two *Rollei* films. The *MD* developer show the best overall results with regard to UV-transmission for both the *AGFA* and *BF* films [29].
Regarding T_{dark} (figure 2.2 *right*) a huge variation is observed (note the logarithmic scale). Again, the light exposure is clearly an important factor. Transmission ranges from fairly transparent (72% for BF) to virtually non-transparent (below 0.1% for both *AGFA* and *Rollei*). Furthermore, some films are less sensitive and maintain similar values for all light exposures, while others span a wide range.
In order to fully estimate and evaluate the quality of the negatives, the transmission data for clear and dark areas are combined, giving the contrast of the different film and developer combinations. The values are plotted in figure 2.3 for all different light exposures [29]. A large contrast difference is ob-

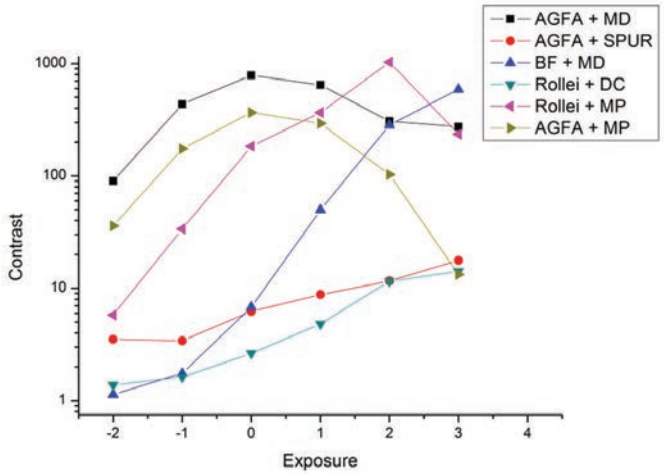

Figure 2.3: Contrast of negatives for all six film and developer combinations.

served, both across the different film/developer combinations and exposure times. Generally, a longer light exposure results in better contrast. Very high

contrasts (over 1 : 300) are recorded for both *BF* and *AGFA* films (developed in both *MD* and *MP*). The *Rollei ATP* and *MP* combination also results in nice contrasts (almost 1 : 1000), whereas contrasts less than 1 : 10 is observed for both the *Rollei + DC* and *AGFA + SPUR* combinations.

Photoresist Quality

Negatives with the highest contrast, for each type of film and developer, are used to fabricate SU8 structures in a standard clean-room process. Film transmission is used to adjust the UV-exposure time for the individual films. The produced SU8 structures are covered with a thin Au film and investigated using SEM *(Hitachi S-4800)*.
All SU8 structures are manufactured on Si wafers with a nominal thickness of $100\mu m$. Bluefire Police film and Agfa Copex Rapid, both developed in the Bluefire Micro developer, produces the best defined structures. In both cases the $100\mu m$ wide microfluidic test channel is clearly reproduced and very mechanically stable following hard-baking [29].
Some limitations of the approach are however also clear (see figure 2.4 and 2.5). First, the walls of the SU8 show a clear "wrinkled" effect, while all

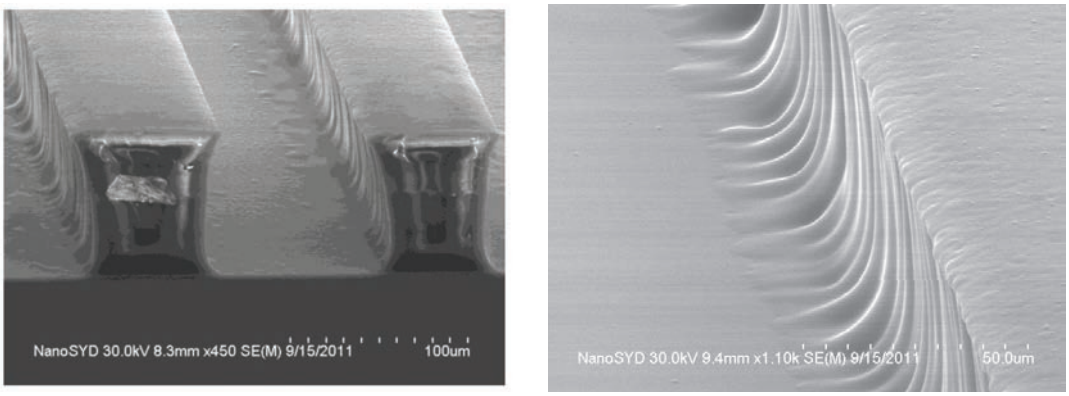

Figure 2.4: SEM images of SU8 channel structures *(left)* and zoom of structure boundary with ripples *(right)*.

structures appear to be significantly undercut (figure 2.4). For free-standing structures such as those used to mold channels, this resulted in the loss of structures smaller than approximately 40 or $50\mu mm$, depending on how well the feature is supported by surrounding material (figure 2.5 *left*). For inverse structures the undercutting leaves well defined holes and trenches in the SU8 (figure 2.5 *right*). It appears that the finer features are properly cross-linked

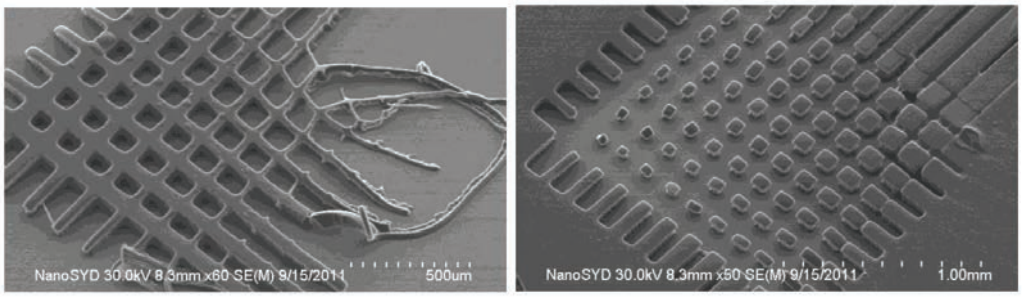

Figure 2.5: SEM images of SU8 grid structure. Developed on same wafer, showing undercut of free standing structures *(left)* and the inverse imprinted structure *(right)*.

during the UV exposure, but they are lost during development, caused by undercutting [29].
All structures show a clear tendency to produce overhangs at the edges (see figure 2.4), and surface debris is often left on the Si substrate after development. As the black masking areas of the negatives does not form a continuous film and are not completely opaque to the UV, cross linking begins in all areas of the film as soon as light exposure begin. SU8 cross-linking commences at the surface and works down toward the substrate. Thus, exposure must continue until the areas under the "clear" parts of the negative have been completely exposed. If contrast is poor, the areas under the dark parts of the negative may be significantly exposed as well. The partially exposed surface will cure and produce debris during development [29].
Since the features edges on the film are not perfectly abrupt, graduation of UV exposure from black to white can also be expected. This produces both the undercut walls and the overhanging surfaces observed. It could also be responsible for the wrinkled texture of the walls. As figure 2.6 shows, maximum contrast is not enough to produce well defined SU8 structures. Consider the fully exposed *Agfa* film developed in *MP (right)* and compare with *BF* developed in the *MD (left)*. Both have the same contrast of approximately $1 : 300$. However the *Agfa+MP* combination produces an very poor SU8 structure in comparison with the other *BF* film. The principal difference is that *Agfa+MP* has considerably lower transparency in the clear areas compared with the other negatives, and this requires considerable increase in exposure time. As well as prolonging exposure in the dark areas, this may also lead to surface heating of the SU8, which is known to induce partial curing [30].

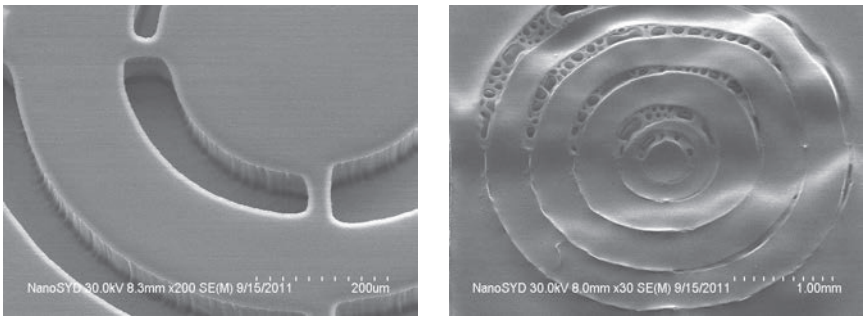

Figure 2.6: SEM images of fully developed (left) and underdeveloped (right) SU8 reticle structure.

Final Considerations

Bluefire Police and Agfa Copex Rapid films are both able to produce SU8 masters of sufficient quality for microfluidic device production. Both films are characterized by high contrast and exceptionally clear underlying base [29].
While the investigations have been limited to one design, there is really a huge range of possible designs that can be created with the method, as the manufacturing procedure is the same. This is regardless of the purpose of the final device. From the presented results a few limitations are proposed for the initial mask and hence, chip design:

- Chip size is limited by dimensions of the photonegative ($24mm \times 36mm$).
- Design structure must be planar 2D.
- Single step photo-lithography - the negatives are not suited for multiple-step processes as alignment is complicated.
- Structure dimensions should not be smaller than $50\mu m$ and properly supported by surrounding structures.
- Inlets and outlet should be at least $1mm$ wide to accommodate fluid port connections.

2.1.2 SU8 Masters

The photo negatives are used as masks in a standard photolithograpic cleanroom process, that creates SU8 microstructures on a Si surface. The process consists of the following steps:

1. SU8 epoxy is spincoated on a cleaned Si wafer. Spin-speed determines thickness of the layer [27]. Spinning at $1500rpm$ for $1min$ corresponds to a $100\mu m$ thick layer.

2. Baking of SU8 to harden the epoxy and evaporate some of the solvent ($5min$ at $65°C$ followed by $10min$ at $95°C$).

3. UV exposure through the mask. Time is determined by recommended dose, UV lamp intensity and mask-transmission at $365nm$ [27].

4. Another baking step to evaporate more solvent ($3min$ at $65°C$ followed by $10min$ at $95°C$)

5. The Su8 is developed under rigid stirring/agitation to remove unexposed SU8 (70% SU8 developer in IPA).

6. Hard baking to remove remaining solvent ($15min$ at 150°C). This makes the epoxy irreversibly solid and mechanically stable.

While steps $1, 2, 4$ and 6 are adapted more or less directly according to the manufacturers guidelines [27], steps 3 and 5 require closer investigation. As the results in section 2.1.1 clearly indicate, film choice and development process greatly influences the UV-transmission of the mask. For all results presented in this work, the Bluefire Police film and Micro-Developer has been used. While optimal contrast is achieved at +3 light exposure, this still only results in a 72% transmission of light at $365nm$. Taking this into consideration, an exposure time of around $50s$ is found optimal.
As each mask design is different, and comes from different $A1$ printouts, certain variation is expected in density in the dark areas of the negatives. This is furthermore influenced by the negative development procedure and non-continuous nature of the negative itself. The effect of this is that not all areas of the SU8 is exposed equally to UV and hence development of the structures is a process that requires close visual inspection. Development times range from $3min$ to $5min$ depending on the above factors and the level of manual agitation.
All structures are investigated in an optical microscope after hard baking to ensure a defect free structure. The two most common type of defects are undercutting and cracks. Figure 2.7 show microscope images of both effects.

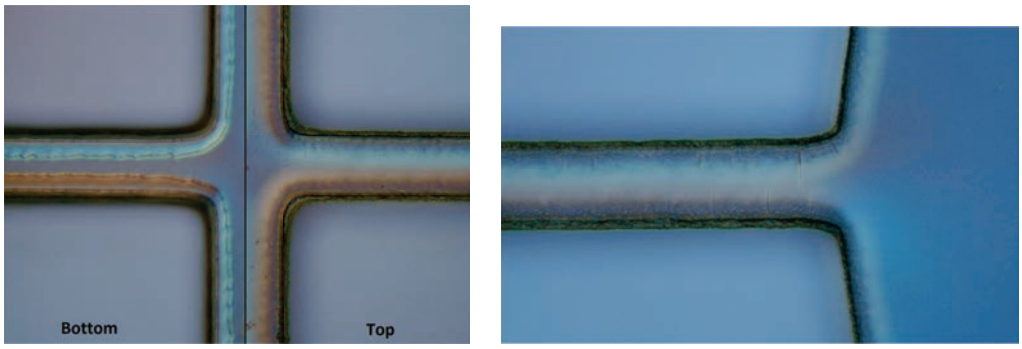

Figure 2.7: Microscope images showing the two most common SU8 defects. Undercuts *(left)* showing top and bottom focus, illustrating missing material near Si surface. Stress cracks *(right)* on the surface of large horizontal structures.

Undercutting *(left)* is, as already mentioned in section 2.1.1, mostly an effect of the grainy transition between dark and blank areas on the photo negatives, but also a side effect of long development time. The stress cracks *(right)* typically occurs on larger planar structures like inlet and outlet pads and is an effect of material stress induced during post-curing and development. During hard baking however, the SU8 becomes slightly less viscous and some degree of self-repair occurs. Stress is relieved and surface cracks close, while undercutting is somewhat smoothened out.
Optical inspection can sometimes deceive as figure 2.8 illustrates. The *left*

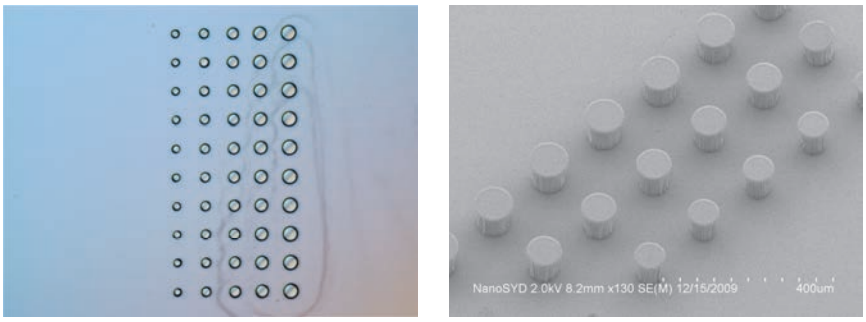

Figure 2.8: Microscope image showing free standing circular structures *(left)*. Tilted SEM image *(right)* of same circular structures showing undercutting.

image shows what appears to be nice looking SU8 dots in a microscope image. Investigating the same structure with an SEM and by tilting the stage, heavy undercutting is observed *(right)*. Figure 2.9 show two SEM images of a space filling channel structure and illustrates how SEM can be used to ensure the quality of more advanced structures.

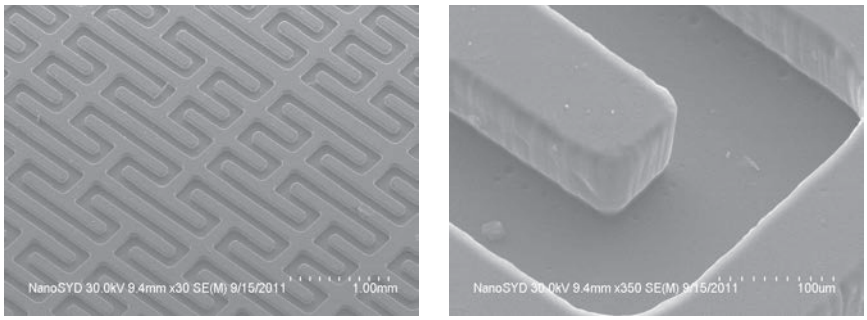

Figure 2.9: SEM images of space filling structure *(left)*, illustrating how SEM is used for inspecting SU8 masters, while precisely measuring dimensions. Closeup of wall texture *(right)*.

While SEM is a great method for investigating SU8 structures for both structural features and size measurements, it is rather time consuming and moreover requires the structure to be covered in a thin conductive coating that can affect PDMS molding.
A profilometer *(Dektak 150 Surface Profiler, Veeco)* is a quick and very useful tool for measuring the SU8 structures to ensure proper calibration of design dimensions, while measuring channel and structure sizes. Figure 2.10 shows a scan across a $100\mu m$ wide SU8 channel structure. The non-symmetrical

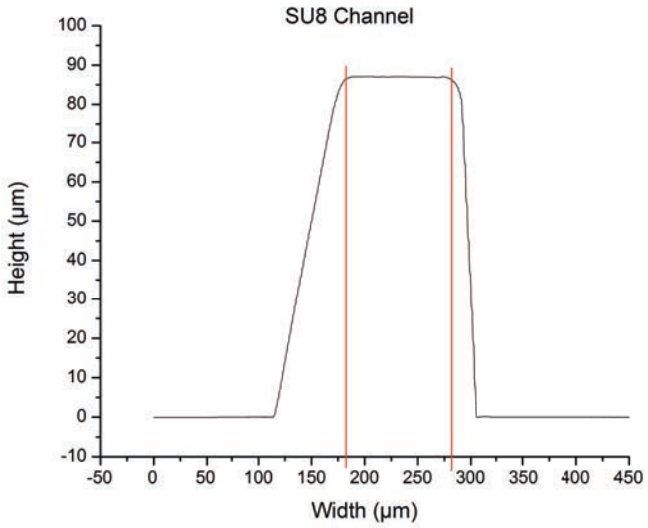

Figure 2.10: Scan profile of $100\mu m$ wide $90\mu m$ high SU8 channel structure obtained with a profilometer.

profile is an effect of the scan-direction (right to left) caused by the size of the needle used for scanning and the sharp features of the SU8 structure. This also causes the tilted edges on the profile, meaning that the real width is closer to the value at the top (illustrated by two red lines). The height measurement is on the other hand more reliable. Generally, the SU8 structures are found to shrink a few μm during hard baking as the last solvent is driven out of the polymer.

2.1.3 PDMS Molding

The hard baked and solid SU8 structures can now be used as master structures in a replication process of PDMS. By molding PDMS onto the SU8 structured Si wafers the inverse pattern can be replicated repeatedly, producing many chips from a single master [11].
For each chip around $7g$ of liquid PDMS is used. In order to prepare the polymer, a 1 : 10 weight ratio mixture of PDMS *(Dow Coring Sylgard 184)* and curing agent is measured out and stirred well. Mixing introduces a lot of air-bubbles, so to eliminate these the mixture is out-gassed for $30min$ in a glass vacuum bell (pressure $75mBar$). Failing to remove all air from the mixture can lead to trapped pockets or air during curing which can serve as unwanted scattering points for the optics, or simply distort the microstructures.
The Si wafer containing the SU8 structures are cut into $25.8 \times 37.8mm$ rectangles using a diamond-bladed dicing saw *(Disco DAD 2H5, Jongshiann Enterprise Ltd.)* and are mounted inside a custom made (by *Sønderborg Værktøjsfabrik*) stainless steel mold (see figure 2.11). The $0.5mm$ thick Si wafer (1) is mounted in a $0.45mm$ deep recess (2) and clamped down using an O-ring (3) *(NBR 70)*. A lid (4) containing 14 $1.1mm$ diameter holes are mounted on top using four $M5$ bolts. Small steel pins (5) can be inserted into these holes and are used to mold the fluid inlets and outlets of the chip. The 14 holes are arranged in two rows of 5 plus two rows of 2 (internal spacing $5mm$), making a wide range of inputs and outputs geometries available. A small top plate (6) is mounted on the pins to prevent them from sliding out during curing.
The out-gassed liquid PDMS mixture is poured into the assembled mold through an orifice (7) in the side and out gassed for $10min$ to remove any air bubbles induced during pouring. To cure the PDMS the mold is placed on a hotplate and heated at $100°C$ for at least $30min$ [31].
When cooled off sufficiently (to room temperature), the mold is disassembled and the PDMS chip is peeled off. The smooth surface of both Si and SU8

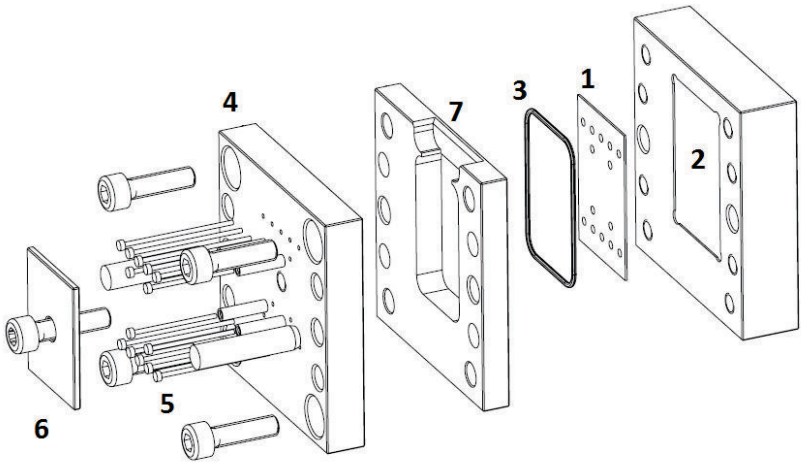

Figure 2.11: Expanded view of custom made stainless steel mold for PDMS chip molding. The Si wafer containing the SU8 master structure is mounted using an O-ring and 14 pins are used to mold flow connectors.

ensures easy release of the PDMS, without the use of release agents or other treatment. This is also attributed to the low Young's modulus of PDMS [11].

2.1.4 Chip Sealing

The final step in completing the PDMS chip is sealing of the liquid channel structures. Depending on chip material, literature offers a wide range of solutions [8]. For chips made of PDMS the process is straight forward and can be done without adding any glue or epoxy [9].
PDMS can be made to bond with a range of materials, most importantly silicon, glass and PDMS itself. This enables creation of pure PDMS chips that react uniformly to external influences (heat, humidity etc.) as well as any chemical (reagents in solution, pH changes etc.) or physical (laser light, electrical fields etc.) interactions.
For sealing with PDMS, thin sheets ($2mm$ to $5mm$) are molded onto glass objective slides (see figure 2.12) and cured, using the same parameters as for the chip itself. After curing, the sheet is peeled of the glass slide and flipped over as the surfaced molded against the glass is completely flat. While a slight curvature is noticeable near the edges (due to surface tension), this is rarely a problem in the final application as most structures are placed centrally on the chip.
In order to ensure proper bonding of the lid to the PDMS chip, the surface is chemically activated. This is done by surface oxidation, which exposes silanol

Figure 2.12: Picture of glass slide with thin layer of PDMS, used as lids for PDMS chips.

(OH) groups on the surface. When two activated surfaces are brought together, covalent siloxane ($Si-O-Si$) bonds are formed. This method works for a range of materials containing Si, including glass substrates and Si-wafers [9].
In practice, activation is done using a low pressure oxygen plasma [12]. Before being exposed to the oxygen plasma, both PDMS chip and the lid are thoroughly cleaned. This is done by submerging both parts in 20% HCl and sonicating for $8min$. After being dried, the parts are placed in a plasma asher (*LFE Plasma Asher 120*). The chamber is pumped down to below $50mTorr$ and $15sccm$ of pure oxygen is vented into the chamber, resulting in a base pressure around $100mTorr$. A $80W$ RF-plasma is induced and maintained for $10-15s$ which is amble time for the PDMS surface activation [12]. After this procedure the PDMS surface stays activated for up to $15mins$ and then slowly starts recombining. The chip and lid are now manually joined and firmly pressed together (by hand) to avoid trapped bubbles etc.
If needed, post-sealing alignment can be made using methanol that enables the lid to be moved into the correct position [12]. After evaporation of the methanol the seal then establishes. As the lids used in this work contain no structures only very coarse alignment is necessary. The procedure can be useful when creating stacked devices.
Experience shows that the sealing needs at least $24hours$ to be fully established and strong enough to withstand the pressures the experimental conditions apply.
No rigid investigations have been made into the strength of the seals, but from experience, the bonding withstands any reasonable input flow speeds (up to and over $0.5mL/sec$). Figure 2.13 show a cross sectional cut of a PDMS chip, indicating the strong and homogeneous bonding of the lid. The shape of the microfluidic channel is also visible *(right)*. The shape corresponds well with the slightly undercut features observed in the SU8 masters in section 2.1.2.

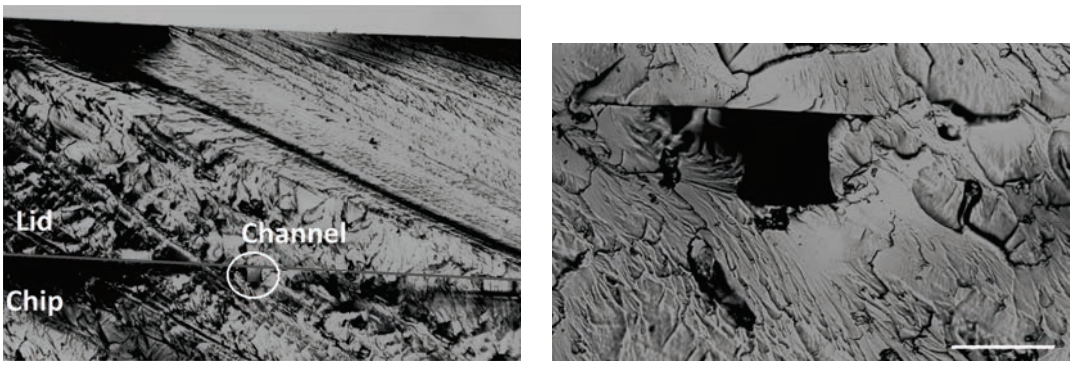

Figure 2.13: Microscope images show a channel cross section and chip lid *(left)*, and closeup of channel shape *(right)*. Scalebar 100μm.

2.1.5 Chip Chuck

For interfacing the LOC device with the remaining flow setup a novel device has been developed [32]. This *chip chuck* consists of a flat plate with an array of blunt stainless steel tubes that align with the fluid ports in the chip channel structure (figure 2.14 *(middle)*). To mount the chip, it is simply

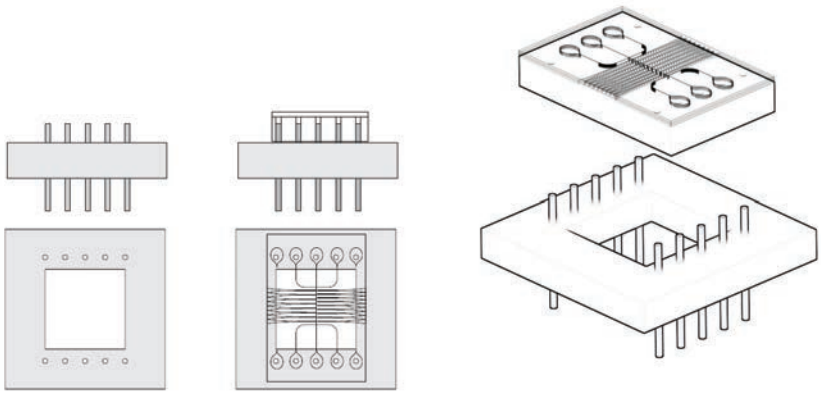

Figure 2.14: Schematic drawing showing the principle idea of the 'chip-chuck'. Steel tube connectors are mounted in the chuck *(left)* and the PDMS chip can be directly pushed fit onto the connectors *(middle)*. 3D view of PDMS chip and chuck *(right)*.

pressed onto the steel tubes (figure 2.14 *(right)*). The tubes are slightly wider (1.2mm) than the holes, and combined with the elasticity of the PDMS, this is sufficient to seal the chip to the tubes and hold it in place while allowing it to be easily removed and replaced. The chuck plate has a central window to

allow illumination of the chip from below and facilitate microscopic imaging of the fluids in the chip.
The chip is connected to the external syringe drivers by either one of two polymer tubes, depending on experiments. For straightforward connection PDMS tubing is used. The tube has an internal diameter of $1mm$ and can be fitted directly onto the stainless steel tubes in the chip chuck. The slight expansion of the tube ensures a water tight seal. The tube is also mounted onto a $18gauge$ ($1.270mm$) blunt needle that enables connection to any *Luer-Lok* or *Luer-Slip* type syringe.
When using more reactive chemicals or small volume samples, FEP (fluorinated-ethylene-propylene) tubing is used. This tube has an inner diameter of only $200\mu m$ and $1mm$ outer diameter. To interfaced this thin tube with the *chip chuck*, it is glued inside a stainless steel tube, that works as an adapter (see figure 2.15). Figure 2.16 shows oil droplets of different sizes traveling inside the $200\mu m$ thin FEP tube.

Figure 2.15: Picture of FEP tube glued inside a steel tube adapter.

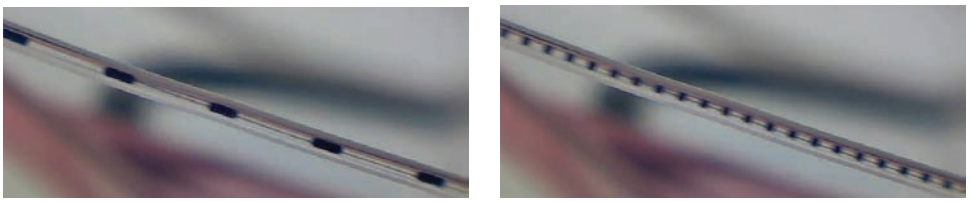

Figure 2.16: Picture of oil droplets (blue) traveling inside the $200\mu m$ I.D. FEP tube.

2.2 Optical Detection

In this section the optical detection system will be discussed. Laser light is used to induce fluorescence in the microfluidic LOC setup, while opto-electrical components are used to convert the collected optical signals into analogue signals, which are then converted to digital signals on a PC. Optical fibers are used to guide light in and out of the LOC system and serves as the link between the microscopic device and macroscopic detection setup.
There are a few reasons why fiber optics are favorable over conventional open air optics. For one, it ensures that the input laser light is delivered directly at the correct position without using extensive open air optics to focus a beam down to a narrow spot. While a microscope objective is still needed to couple the light into the fiber, it is only done once and is not affected when changing chips. Secondly, as the fibers are positioned in-plane with the microfluidic channel and are always in the correct position, no alignment is needed. Furthermore, in regards to collecting scattered light, and more importantly, fluorescent light, this method is more effective as light can be collected closer to the source and with a higher intensity. Several approaches to increasing this will be discussed later. In the first section however, the experimental setup is presented, along with a closer look into each component and its function.

2.2.1 Experimental Setup

A schematic presentation of the entire setup is shown in figure 2.17. The setup consists of the following parts.

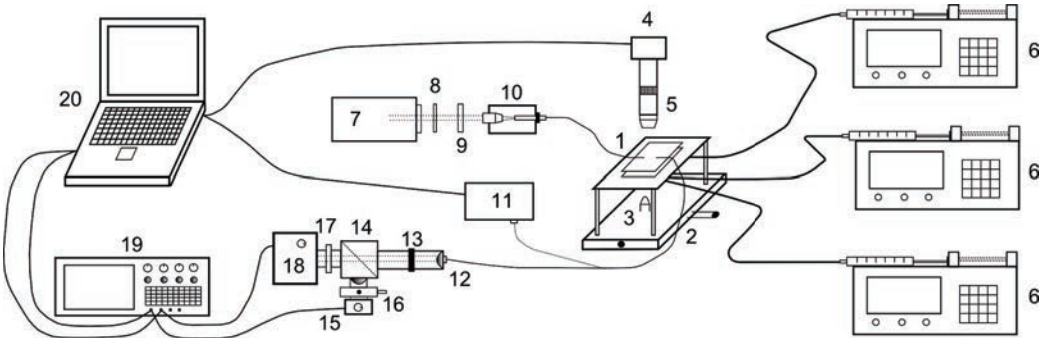

Figure 2.17: Schematic drawing of the experimental setup. Numbers are explained in the text.

LOC Stage The LOC device is mounted on the chip chuck (1). The chuck is mounted on a XY stage (2) with $1cm$ travel in each direction. A white LED (3) is positioned under the chuck for illumination. A USB CCD camera (4) *(Infinity 1, Lumenera)* is mounted above the chip, along with a $5\times$ microscope objective (5) for visual inspection.

Fluid Control Up to three syringe drivers (6) *(Harvard Apparatus PHD2200, MA, USA)* are used to control volumetric flow through the chip. These are connected to the LOC device as mentioned in section 2.1.5.

Laser Source Two different lasers (7) are used in the experiments. The mostly used is an Ar-ion laser (*161 LGS, LG Laser Tech*) emitting $488nm$ laser light with a maximum power of $30mW$. Alternatively, a $40mW$ $405nm$ GaN laser *(LD-WL206, Roithner Lasertechnik)* can also be fitted into the setup. Both lasers are passed through a laser-line filter (8) to select to correct line and optionally an attenuator (9) to reduce intensity. To guide the laser-light into the optical fibers (described in section 2.2.3), a $10\times$ microscope objective is used to focus the light down into the fiber tip (10). The tip of the fiber is mounted in an xyz-adjustable holder, that allows precise alignment.

Detection Optics Emitted fluorescence and scattered laser light is collected in a multi-mode fiber and guided either into a spectrometer (11) or a detection block. In the block the light is collimated using a spherical lens (12) and then passed though an adjustable pinhole (13). A dichroic mirror (14) ensures that scattered laser light is reflected, while fluorescent light passes through. The scattered laser light is focused onto a photo-diode (15) *(PDA36A-EC, Thorlabs)*, using another spherical lens. The photo-diode is mounted on an XY-stage (16) to enable optimization of light collection. Fluorescent light is passed through a laser-line longpass filter (17) to eliminate any scattered light that might have passed through the dichroic mirror. The light is collected using a photo-multiplier-tube (18) *(R928, Hamamatsu)*.

Electronics and Data Analysis The photodiode is a relatively large area ($13mm^2$) PIN photodiode in reverse bias, which uses a build in op-amp based transimpedence amplifier to convert photocurrent into voltage signals. The PMT is mounted in a C6270 socket with integral high voltage supply, controlled by an external potentiometer. Signals from both PMT and the PD are plotted on an oscilloscope (19) *(GDS-2204, GW Instek)*. This allows immediate inspection of signal amplitude and shape, and helps determine correct trigger levels. Both signals are also passed directly to a PC (20),

where an analog-to-digital converter (ADC) card *(PCI-17-14U, Advantech)* collects the data. The card itself is capable of simultaneous conversion on four channels each with its own 30MHz 12 bit ADC.
The data is loaded continuously into a circular buffer in the PC memory and scanned for trigger events. When one is found it is copied into a second buffer where the peak value is measured. The data from each channel is scanned independently in case peaks in different channels are not simultaneous due to different detector rise times. The peak value for each channel is separately recorded for each event. Ten events per second are copied in their entirety into a separate buffer for graphical display in a virtual oscilloscope window in the software.

Software A custom made program (written in C++) is used to control trigger rate, data plotting and other important factors. The UI of the program is shown in figure 2.18. Main features include a live scope (i) showing

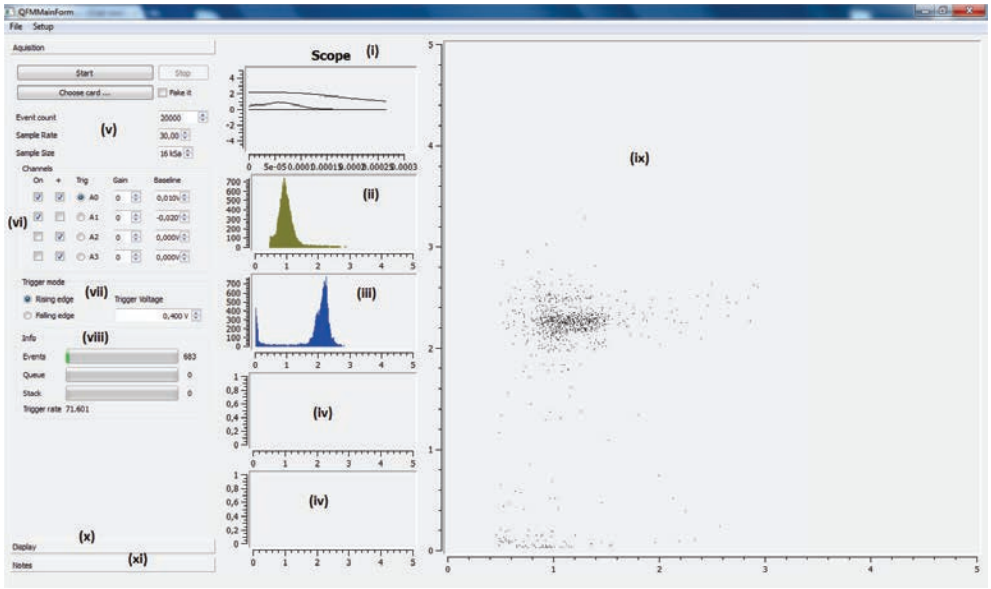

Figure 2.18: Screenshot showing the UI of the custom made flow cytometry software. Numbers are explained in the text.

every 50 data-set (to limit CPU use), accumulated histograms for both scatter (ii) and fluorescence (iii), and potentially two more channels (iv). Data acquisition can be controlled in detail (v), while each signal can be adjusted individually (vi). Finally, the trigger value (vii) can be set (all peak-finding is done in software), while trigger-rates, event count and memory stacking values can be observed (viii). The scatter plot (ix) show the last 500 obtained

data points. Plotting ranges can be adjusted in the 'Display' menu (x) where data is also saved, while Notes (xi) adds custom notes to the saved data file.

2.2.2 Detection Area

In this section the optical detection area of the chip is investigated. The exact geometry and physical conditions around the optical measurement volume is crucial to optimizing optical signals in the device. Figure 2.19 shows a schematic drawing of the detection area. The two optical fibers are positioned

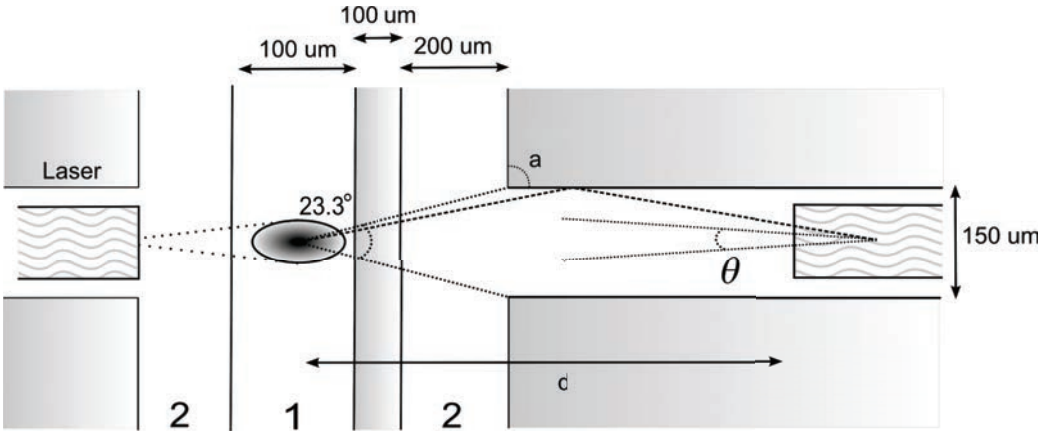

Figure 2.19: Schematic drawing showing the optical detection area of the microfluidic chip. The area contain two optical fibers with individual flow channels (2), as well as the sample flow channel (1).

within the detection area, where the main flow channel crosses the optical axis. The optical measurement volume is the cross sectional volume between the sample flow and the laser beam path. The beam shape is conical, but truncated by the sample flow. The exact size of the volume depends on flow focusing and the input fiber. On figure 2.19 the single mode input fiber (left) emits laser light in an angle θ_{AC}, the acceptance angle of the fiber, given by

$$\theta_{AC} = \arcsin\left(\frac{NA}{n_m}\right) \tag{2.1}$$

where NA is the numerical aperture of the fiber $(0.10 - 0.14)$ and n_m is the refractive index of the surrounding media (in channel 2). For an empty channel (containing air) $\theta_{AC-in} = 6° - 8°$. After leaving the fiber, light passes through a thin $(100\mu m)$ PDMS wall and enters the liquid sample channel. Here the light interacts with the flow focused sample.
A quick geometric calculation (disregarding changes in refractive index) gives

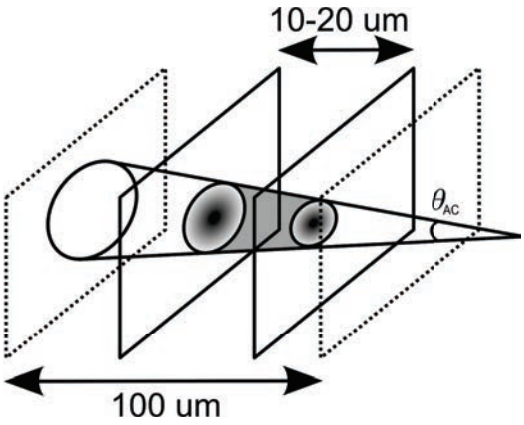

Figure 2.20: Schematic drawing of the measurement volume, compromised by the overlap between focused flow and the cone of laser light emitted by the input fiber.

an estimated sample volume of $0.15nL$, where the volume is assumed to be a truncated cone with top-radius $17.8\mu m$, base-radius $23.7\mu m$ and height $100\mu m$ (the channel width). See figure 2.20. If a focused sample flow is assumed (20% of the total width), the sample flow volume is by comparison $0.096nL$ (for the circumscribed square). The overlapping volume (inscribed circle) is however only $0.046nL$ (grey area on figure 2.20), which corresponds to 48%. Hence, at any given time, the laser light only illuminates roughly half of the passing liquid volume. This holds for any width of the focussed flow and is worth considering in later experiments.
In the optical measurement volume scattering of the laser light and emission of fluorescence occurs. The resulting light now passes through another PDMS wall into the optical output channel (channel 2) where it is collected using a multi-mode fiber ($NA = 0.22$). The total amount of light that can be collected in the output fiber is limited by its acceptance angle, which in turn depends on the refractive index of the media in the optical channel. In the case of air ($n_{air} = 1.00$),

$$\theta_{AC-air} = \arcsin\left(\frac{NA}{n_{air}}\right) = 12.83^{\circ}. \tag{2.2}$$

By changing the media in the optical channel and increasing n, higher acceptance angles and more collected light can be achieved. Another way to maximize the amount of light is by introducing optical elements (lenses) in the light pathway. Both approaches are explored in the following sections.

2.2.3 Optical Fiber Connection

As with the fluid connections, fiber integration is done quite easily in this system, utilizing the properties of the soft PDMS material [33, 34]. Guiding channels are molded directly into the chip as part of the mask design. Optical fibers are slid into the these channels, one on each side of the main flow channel (see figure 2.21). The fibers come to a natural stop at the correct position

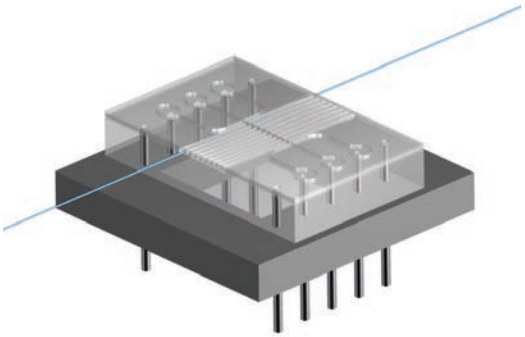

Figure 2.21: 3D concept drawing of mounted PDMS chip with optical fibers inserted (blue lines).

when encountering the thin PDMS wall separating the guiding channel from the flow channel. Several parallel guiding channels are molded into the chips to facilitate multiple fibers, or as backup if the fibers get blocked or break. All guiding channels are interconnected to prevent air getting caught in front of the fiber, creating a piston-like effect. This separated channel system is also connected to an inlet and outlet, making it possible to inject material for waveguide investigations. An example of such a chip design is shown in figure 2.22. As an input, a narrow core ($4.3\mu m$) single-mode fiber is used (*F-SV 50*, Newport Cooperation). This ensures a narrow exit angle that in term ensures a small, but focused measurement volume. As output fiber a multi-mode ($100\mu m$ wide core) fiber is used *(manufacturer)*, which ensures maximum amount of collected light. Fiber cleaving and insertion are done under $5\times$ microscope magnification, to ensure that the sharp fibers do not penetrate into the main flow channels.
Investigations have been made into the optimal way of clamping the optical fibers. The best design is a tapered channel, going from $2.5mm$ in width at the point of entry, down to $150\mu m$ near the flow channels. The wide mouth ensures easy insertion while the tight end clamps the fiber in place. This is enough as the channel is only $100\mu m$ high, while the fibers are $125\mu m$ in diameter. Hence, the PDMS around the fiber is slightly compressed and works as a seal.

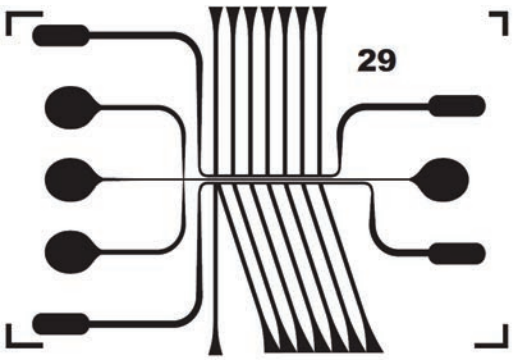

Figure 2.22: Chip design 29, featuring three flow inlets *(left)*, one outlet *(right)*, connected by channels *(horizontal)*. With separate inlets and outlets for optical fiber channels (*up* and *down*) as well as tapered fiber guiding channels (*vertical* channels).

2.2.4 Angled Output Fibers

One major drawback of using in-plane excitation and detection is background signals. When using out of plane excitation, the only laser light that passes into the output fiber is whatever is scattered sideways by samples in the fluid channel. This is because of the narrow acceptance angle of the optical fiber. When the input and output fiber are positioned opposite each other (like in figure 2.19), a considerable amount of the laser light, that does not directly interact with the sample, still couples directly into the output fiber. The excited fluorescence can be considered as a uniform spherical source, is therefore omni-directional and can be collected anywhere near the sample volume.
By angling the output fiber with respect to the optical axis, the fluorescent light can still be collected, while the amount of directly coupled laser light is reduced. Meanwhile, laser light scattered from samples in the flow will mainly be spread in a forward direction, but still over a fairly wide angle, and can consequently still be collected in the output fiber.
To investigate the influence of angle on laser light and fluorescence, a chip with different angled output fiber channels is created (see figure 2.23 *left*). The angles (with respect to the optical axis) are $0°, 9°, 13.75°, 18°, 27.5°, 36°$ and $45°$ (left to right). The sample channel is filled with a fluorescent dye (*Pyridine 2* in $DMSO$ $[0.85g/l]$) and input and output fibers are positioned as shown on figure 2.23 *right*. Laser light ($488nm$) is guided into the input fiber and the emitted fluorescence and scattered light is collected using a spectrometer (*Ocean Optics USB4000*) connected directly to the output fiber. The fluorescence signal is integrated for $100ms$ and averaged over 10

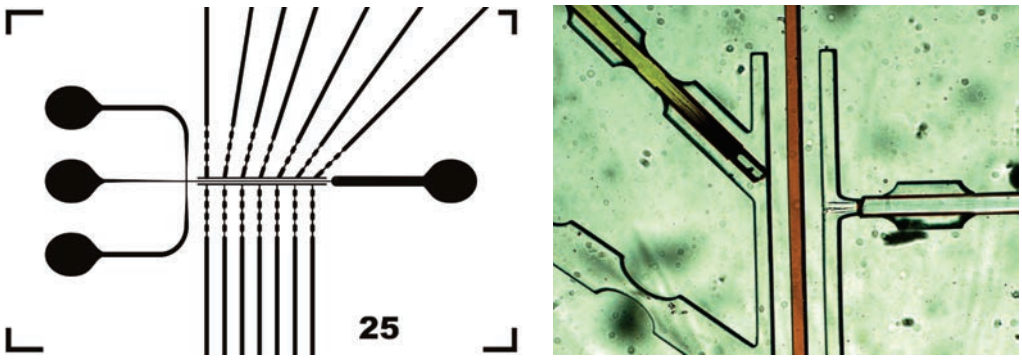

Figure 2.23: Chip design 25 *(left)* featuring fiber guiding channels with different angles. Microscope image *(right)* showing optical fibers in angled channels during measurements.

measurements. The obtained results are shown in figure 2.24 *left*. The right plot shows a non-linear dependence between angle and intensities for the fluorescence.

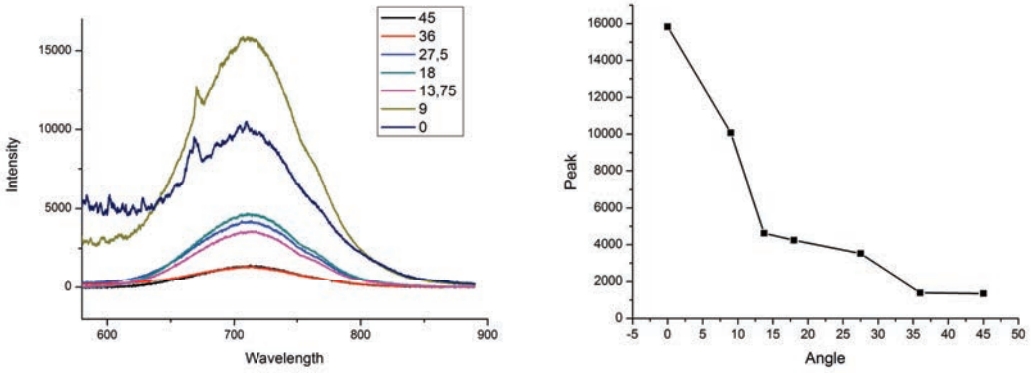

Figure 2.24: Plot showing fluorescent spectrum for angled fibers *(left)* and maximum intensities as function of angle *(right)*.

To measure the absolute intensity of the laser peaks, the laser is attenuated and the peak centered around $488nm$ measured. The measurements are plotted in figure 2.25 for the four lowest angles $(0°, 9°, 13.75°, 18°)$. As expected, the laser intensities also decrease with the increase in angle.
As the fluorescence peaks for 13.75° and 18° are almost identical, the difference is still noticeable for their laser peaks. Therefore, the 18° angled output fiber channel is estimated as being an optimal compromise between loss in fluorescence and the reduction in laser light background. This angled fiber channel design is adapted into all following chip designs.

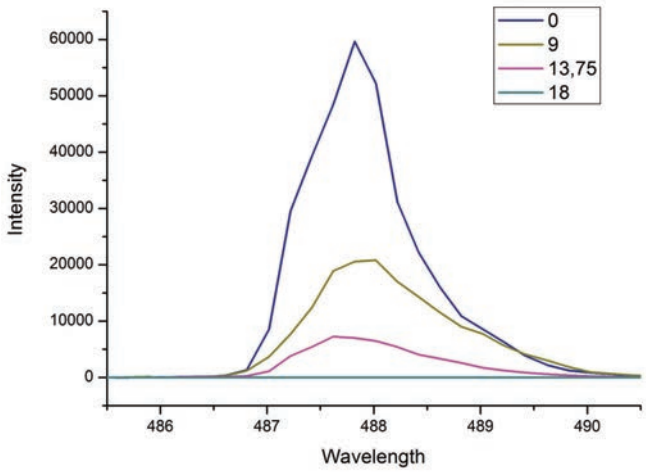

Figure 2.25: Spectrum of attenuated laser peaks for angled fibers.

2.2.5 In-plane Lenses

As mentioned earlier, there are several ways to increase the amount of collected light in the optical output fiber. The use of planar optics have been successfully adapted by several groups, focusing on positioning lenses at the input fiber to increase fluorescence excitation [35, 36]. Here, in-plane optical lenses are added in the path of the scattered and fluorescent light (on the output side). By doing so, the spatial angle from which light is collected in the multi-mode fiber can be increased. In-plane lenses are not true optical lenses, but rather curved 2D surfaces in the plane of the microfluidic chip. For this reason, they are very easy to incorporate into the chip design as they can be molded into the PDMS along with the other chip features.
The optical behavior of these 2D lenses can be described using paraxial optics. Using simple ray-tracing and transfer matrix analysis, the complete path from source (measurement volume) to end-point (output fiber) can be described using linear algebra.
Designs with either three or five lens-elements (curved planes) are investigated. Due to manufacturing effects and optical considerations, certain constraints on the systems are necessary. No features are smaller than $100\mu m$. This is due the the resolution of the photo-negative masks. Furthermore, due to the acceptance angle of the output fiber and the size of the output fiber channel (which creates an aperture), the maximum width of a lens is restricted to $200\mu m$. This also applies for the remaining lenses. Lastly, all structures are considered as thin lenses (which have negligible thickness compared to their focal length).

Lens	Type	Amount	Distance	Radius	Focal-length
1	Ball	2	100	100	400
2	Ball + Biconvex	2.5	80, 100	50, 200	1000
3	Ball + Biconvex	2.5	80, 100	100, 200	700
4	Ball + Biconvex	1.5	300	100, 200	600
5	Biconvex	2.5	300	200	600
6	Ball	1.5	300	100	400

Table 2.1: Calculated feature sizes (all in μm) for all six lens structures.

Based on the above restrictions and dimensions a number of different designs have been calculated by ray tracing through an $ABCD$ matrix system. Tracing is done in a simple C++ coded program, varying parameters such as fiber distance x, number of curved surfaces (3 or 5), radius of curvature R etc. By restraining some parameters, others are varied within the set limits and the optimal design is found in each case. In figure 2.26 six optimized designs are shown. Table 2.1 show the values used to construct these lenses.

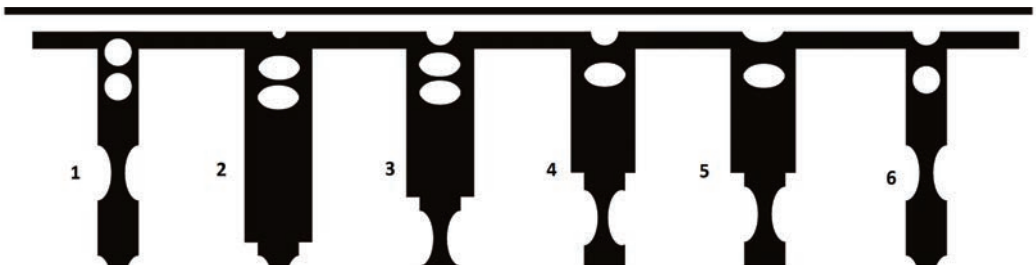

Figure 2.26: CAD drawing of all six lens designs.

To test the lens structures the main fluid channel is filled with a fluorescent dye (*Pyridine 2* in $DMSO$ [$0.85g/l$]), which is excited by the $488nm$ laser light from the single-mode input fiber. The output fiber is inserted in front of the lens structures at the correct focal length (see figure 2.27 *left*) and directly coupled into the spectrometer (*Ocean Optics USB4000*). A full spectrum is recorded ($100ms$ integration time, averaged over 10 measurements) for all six lens structures and a seventh unstructured fiber channel. The spectra are normalized by attenuating the laser beam and measuring the laser peak between each lens measurement. The obtained results are plotted in figure 2.28.
The results clearly indicate that the lenses do not have the desired influence on the amount of obtained light, as all fluorescence peaks are lower than the reference. It is also noted that the lens structures consisting of only three

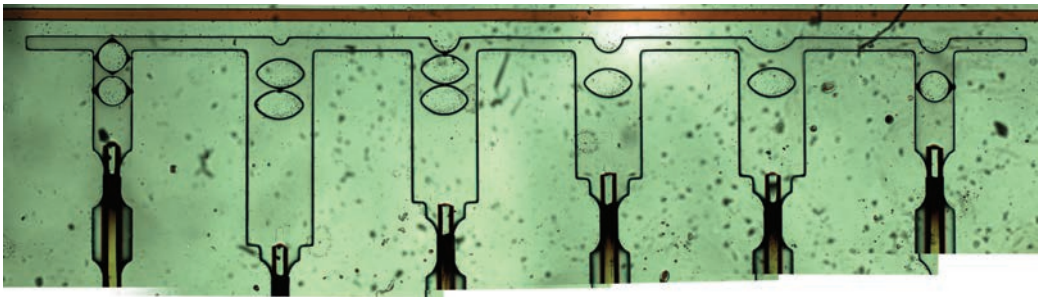

Figure 2.27: Microscope images showing the optical output fiber mounted at the focal point of all six lens structures. Comprised of six overlapping images.

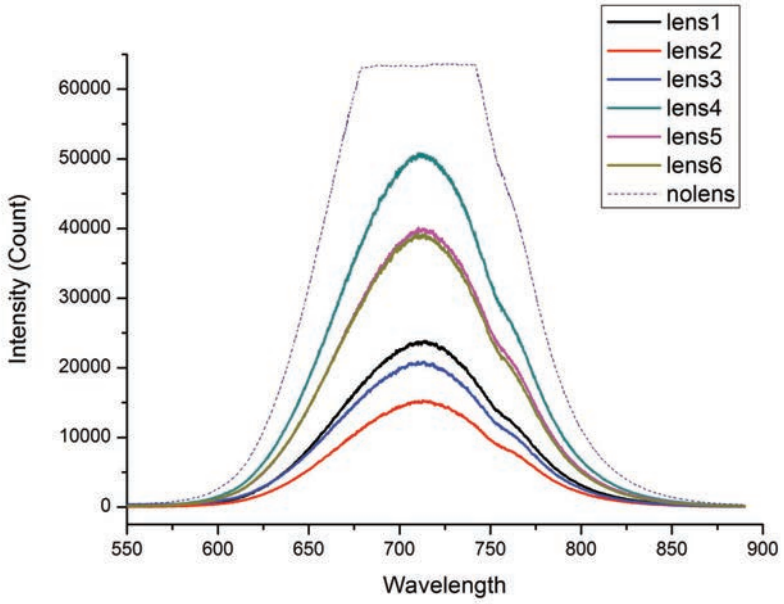

Figure 2.28: Spectrum showing the fluorescence intensity measured using the six lens structures (and one without).

curved surfaces (lens 4, 5 and 6) gives better results than those with more curved surfaces.
The PDMS chip is consequently investigated with SEM (*Hitachi S4800*) and the obtained images (figure 2.29) help explain the observed negative results. The SEM images reveal two distinct complications (also observed in section 2.1.1). Firstly, the curved surfaces are not as smooth as expected and ripples are clearly visible along the surfaces. This is most likely carried over in the PDMS during the molding procedure from the SU8 and can be ascribed to the grains of the photo-negative mask, creating discontinuous transitions. Furthermore, it is clear from the images that the initial SU8 structures have been undercut during development. This creates overhangs and lips on the top of the PDMS structures, which interconnect the lens surfaces in certain points.

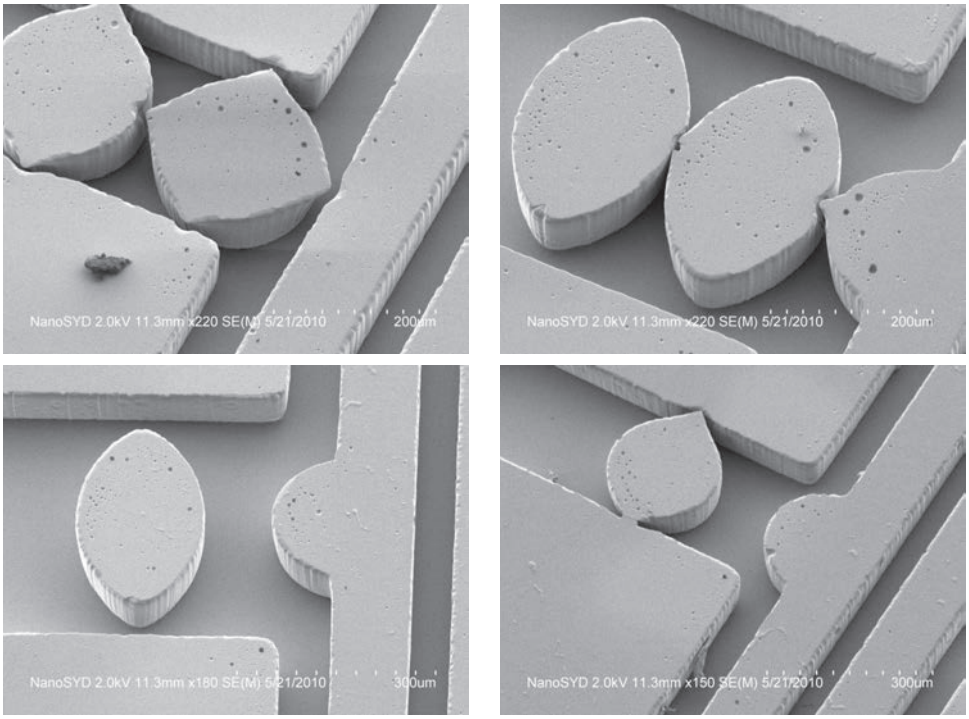

Figure 2.29: SEM images of PDMS in-plane lenses. Lens 1 (*topleft*), Lens 3 (*topright*), Lens 4 (*bottomleft*) and lens 6 (*bottomright*).

Both effects contribute to an uneven and rough surface where each feature serves as scattering points for the emitted fluorescent light. This is supported by the fact that structures with more curved surfaces (lens 1, 2 and 3) provides the least amount of light.
While this approach should work (both according to calculations and sources

in literature), it sadly proves less successful than expected. The reason for this is the limitations imposed on the system by which the microfluidic chips are produced. In order to improve the lens quality, there are two fundamental steps that can be taken. A commercial mask can be used instead of the photo negatives, and while an expensive and time consuming step, this is guaranteed to improve lens quality immensely. As a compromise, an alternative method can be developed, where the photo negative masks are used to define a photo-resist structure on Si, which is then used as an etch mask in a ICP-RIE process. The etched Si wafer can then be use to directly mold PDMS lenses. Both suggestions are however outside the scope of this work and no further investigations into improvement of lens quality has been made.

2.2.6 Index Matching

As mentioned, another way to increase the amount of fluorescent light that couples into the output fiber, is by utilizing index matching between the interfaces along the optical path. Furthermore, by choosing the correct refractive index, total internal reflection and waveguiding can be achieved [37]. Microfluidic chips with straight and angled (18°) fiber inlet channels are used in this experiment (see figure 2.22). The fluorescence signal is considered a point source in the middle of the fluid channel, and the aperture of the output fiber channel is calculated to 23.3° based on the dimensions of the chip. Again, *Pyridine 2* in $DMSO$ ($n = 1.4785$) is used as fluorescent dye and is excited by $488nm$ laser light. As the light travels from the source to the tip of the optical output fiber, it passes through three interfaces. First, from the fluid channel (1 on figure 2.19) into the PDMS wall ($n = 1.4348$ [38]) and then into channel 2. This channel is per default empty and contains air, but can be filled with any liquid (as described in section 2.2.3). The last interface is from channel 2 to the core of the optical fiber ($n = 1.458$). By filling channel 2 with liquids of different refractive index, index matching and waveguiding effects can be investigated. Apart from air ($n = 1.000$), ethanol ($n = 1.36$) and gelatin ($n = 1.536$ [39]) is selected. Ethanol is mainly selected as it can also be used as lubricant when inserting the optical fibers into the chip as well as a refractive index fairly close to that of PDMS. Gelatin is specially selected to investigate waveguiding, as the refractive index is higher than PDMS.

First, the direct transmission of fluorescence across the different interfaces from the source (Pyridine 2) to the pickup fiber is considered. This is straight forward, as transmission coefficients are multiplicative. By using the Fresnel conditions, the coefficient of transmission T for any EM-wave normal to an interface, is given by

$$T = \left(\frac{2n_1}{n_1 + n_2}\right)^2 \cdot \frac{n_2}{n_1} \tag{2.3}$$

where n_1 is the index of refraction of the initial medium, n_2 is the medium that the wave is transmitted into [40].
Considering the optical path for the emitted fluorescence (see figure 2.19), three interfaces are crossed. The total transmission over all three interfaces, can be calculated for all three cases:

$$T_{Air} = 93.78\% \tag{2.4}$$

$$T_{Ethanol} = 99.77\% \tag{2.5}$$

$$T_{Gelatine} = 97.61\% \tag{2.6}$$

These results assume 100% transperancy in all media. No major differences are observed, even though it is clear that the low refractive index for air is a disadvantage here.
To investigate if waveguiding is possible into channel 2 the critical angle θ_c is calculated. Incident light (with $\theta > \theta_c$) can be total internally reflected, so no light is lost out into the chip. By applying Snell's law [41] and considering the difference in refractive index between the two media (PDMS and waveguide material), the critical angle can be found as

$$\theta_c = \arcsin\left(\frac{n_2}{n_1}\right) \tag{2.7}$$

Doing this gives a value of 44° for gelatin, while no total internal reflection is possible from neither air nor ethanol, as their refractive index is smaller than that of PDMS.

Two simple experiments are conducted to investigate waveguiding effects from gelatin. In the first experiment the optical output fiber is moved further and further away from the source and the fluorescence signal is measured at each position using a spectrometer. This is done for air, ethanol and gelatin. The exact distance is calculated from a stacked image with all positions superimposed (see figure 2.30). The results are plotted in figure 2.31. Intensities are normalized with respect to the maximum value measured at the first position of the fiber. The measurements for air however,

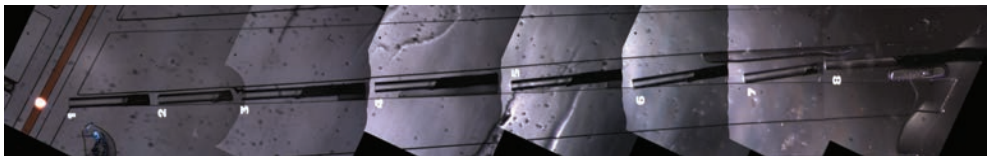

Figure 2.30: Microscope images showing the output fiber position in the gelatin waveguide channel. Composed of eight superimposed images.

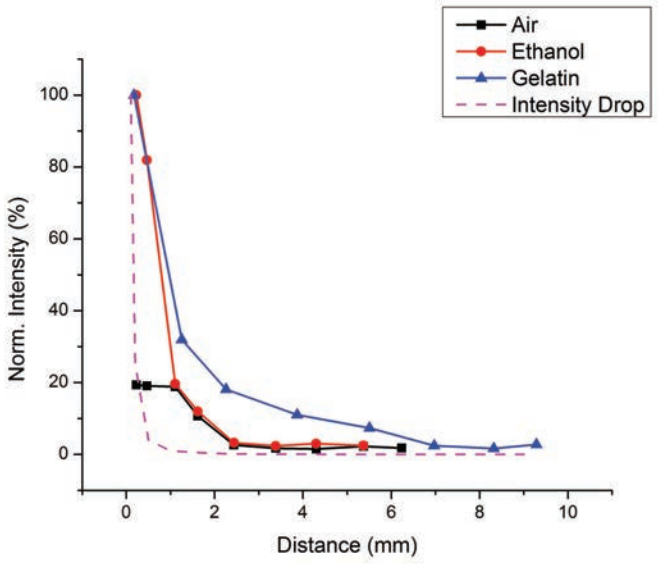

Figure 2.31: Plot showing peak fluorescence intensity as function of output fiber distance for various waveguide materials. Dashed line show $1/d^2$ for comparison.

are normalized with respect to the maximum value for ethanol as the data is obtained under the exact same experimental conditions.
Even though the intensities drop off quite quickly they are still all better than $1/d^2$ (intensity reduction from a spherical wave [40]), which is also plotted in figure 2.31 (dashed line). This indicates, that even for air, some light is scattered on the air-PDMS interface along the channel and is collected by the fiber. This is the same case for ethanol, although slightly more light is collected. Gelatin however makes a real difference and further than $5mm$ away from the fluorescent source, over 10% of the collected light is still being measured. This indicate that gelatin is indeed able to guide light by total interal reflection. This effect is interesting as it extends the options for getting light out of the chip. Even though some light intensity is lost, the possibilty exists for negelting the optical fibers and simply collect the light directly at the chip edge. This would however require some optimization of the setup.

To confirm that the reported measurements are indeed the result of waveguiding, another experiment is conducted. A chip with curved channels is created for this purpose (see figure 2.32). Curve bending radius' range from $R = 5mm$ to $R = 17.5mm$, with curve one having no bend. This design

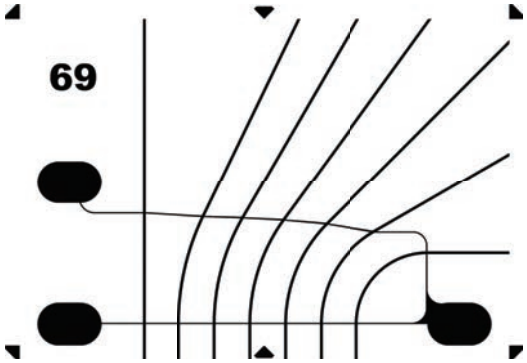

Figure 2.32: Chip design 69 with bent waveguide channels. From $5mm$ to $17.5mm$ bend radius.

has no flow channels, only channels for waveguide material. Laser light intensity is therefore measured directly instead of fluorescence. The chip is designed so that the two horizontal lines have the same distance along the curve ($7.85mm$). The two optical fibers are placed pairwise in the vertical channels and positioned at the horizontal channels. The system is filled with either ethanol or gelatin and the absolute amount of laser light in the output fiber is measured for each curve. Some attenuation of the laser light is required to not saturate the spectrometer.
Figure 2.33 show the results for all six curves, where curve 1 is omitted as the signal is orders of magnitude higher than the rest and saturates the spectrometer even at heavy attenuation. Again the gelatin results indicated waveguiding properties. Both intensity curves drop off as a function of smaller bend radius, which is expected as less and less light is scattered along the interface under increasingly higher angles. The decrease is, however, slower for the gelatin filled channel, indicating that some total internal reflection takes place in this channel. These results confirm those presented above and support this new interesting way of enhancing light collection in microfluidic devices.

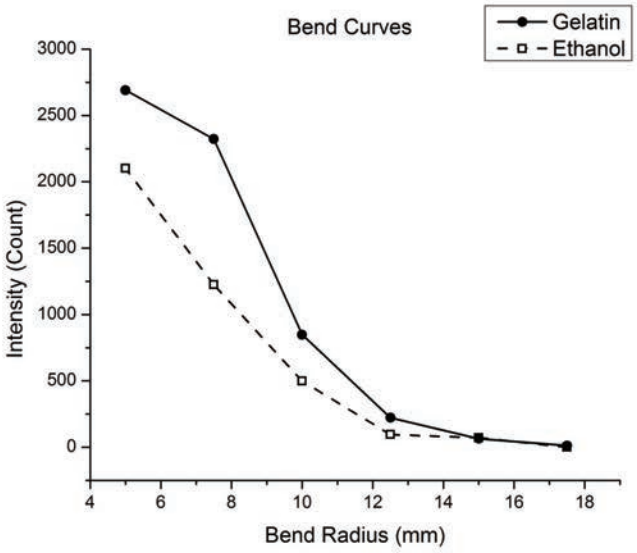

Figure 2.33: Plot showing laser peak intensity in chip design 69 for various bending radius' (5mm to 17.5mm). Plotted for both ethanol and gelatin.

2.2.7 Optical Filtering

As only one optical fiber is used to collect light from the sample volume, the optical signal contains a lot of information. Apart from the fluorescence, scattered laser light is also collected. In order to detect these two signals as distinct events, the optical output is split according to wavelength using a dichroic mirror. This is essentially the same way collected light is treated in a commercial FCM, where a series of filters and dichroic mirrors acts as a crude spectrometer which serves to quantify as much optical information as possible [17].
The mirror (*MD555, Thorlabs*) is specially coated to only reflect light with a wavelength below 595nm, while letting anything longer through. This means that scattered laser light is reflected ($< 99.999\%$) and the remaining flourescent light passes thourgh. However, as observed in section 2.2.4 the laser light intensity is huge compared to the fluorescence. A special laser-line longpass filter (*NT47-503, Edmund Optics*) is used to reflect 93% of the light that does pass the dichroic mirror. Coated optical filters are very sensitive to the direction of incidence and the promised reflection values are therefore to be considered maximum values [42].
The optical output fiber collects and guides all light collected within its acceptance angle and therefore a certain angular spread is expected when the

light leaves the fiber. The angular spread is preserved, meaning that light collected into the fiber at large angles also leaves at large angles [43]. To collimate the light from the LOC device, a spherical lens is placed in front of the fiber output. The collimated light is then passed through the dichroic mirror and long-pass filter with minimum loss.
A variable pinhole (an *iris*) is introduced before the dichroic mirror to reduce the high angle scattered light that randomly makes it into the optical fiber. Figure 2.34 shows the complete optical setup.
By mounting a CCD camera (*Infinity 1, Lumenera*) directly behind the long-pass filter, the effect of the iris can be illustrated (see figure 2.35).

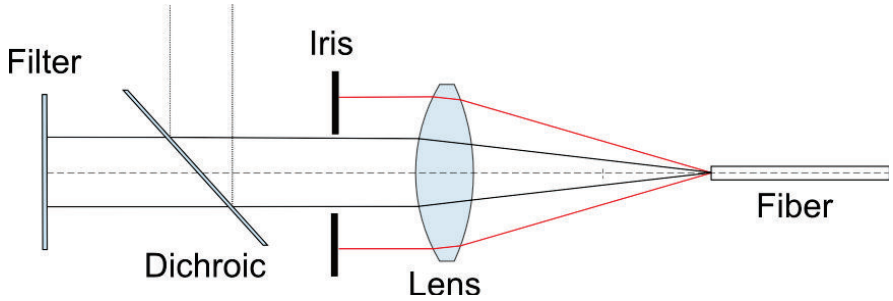

Figure 2.34: Schematic drawing illustrating the effect of using a pinhole to block high angle light from the optical output fiber.

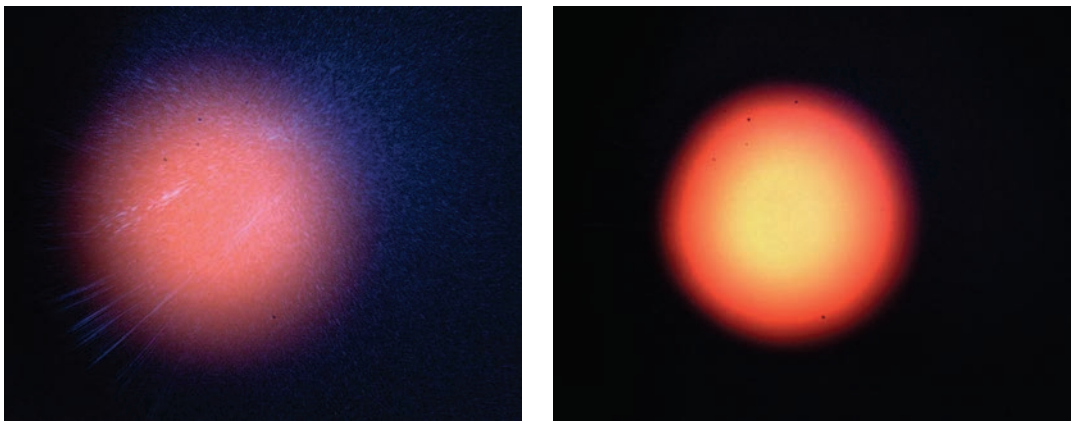

Figure 2.35: CCD images obtained from the optical output fiber with open *(left)* and closed iris *(right)*. A sample of fluorescent PS beads is used.

A sample containing $6\mu m$ fluorescent beads (*Red Fluorescent Polymer Microspheres*) is flowed through the channel slowly ($5\mu l/min$) and the images are integrated for $10s$ to obtain sufficient light and average the scatter and

fluorescent events. The effect is clear and the remaining scattered laser light entering at high angles and otherwise passing through both filters are effectively eliminated.
Figure 2.36 shows a spectrum obtained by replacing the CCD with a spectrometer. These results show that some scattered laser light can pass through the long pass filter and only by combining both filters (long-pass and dichroic) is the laser light suppressed while the fluorescence peak remains.

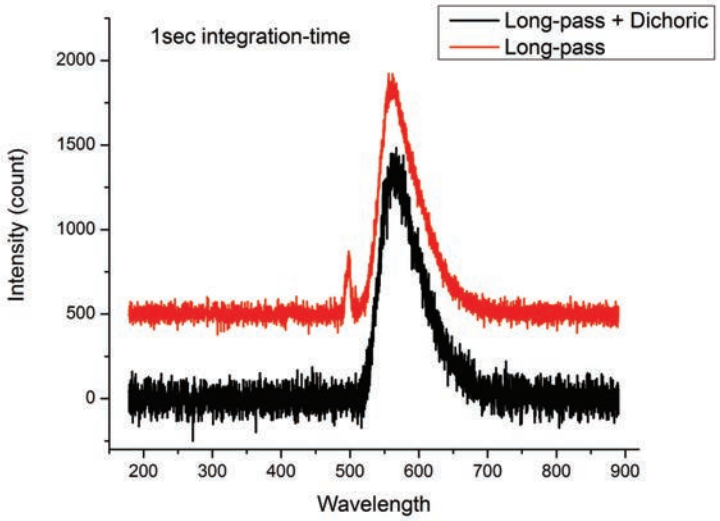

Figure 2.36: Spectrum of fluorescent peaks with and without use of a dichroic (DC) filter. Results shifted for clarity.

Chapter 3

Fluid Dynamics

In this chapter some basic elements of fluid dynamics will be shortly introduced and subsequently used to explore the phenomenon of hydrodynamic focusing. This effect is essential in conducting flow cytometry experiments and will be investigated both experientially and in FEM simulations.

3.1 Velocity Fields

Fluid motion is fundamentally governed by conservation laws, specifically conservation of mass (I), conservation of linear momentum (II) (Newton's second law of motion) and conservation of energy (III) (first law of Thermodynamics), which are all based on classical mechanics. Fluids can be assumed to behave according to the continuum assumption, which means that even though the liquid consist of individual molecules, it can be considered as one continuous phase. From this follows that density, pressure, temperature, and velocity are considered to be well-defined at infinitesimally small points, and are assumed to vary continuously from one point to another.
The Navier-Stokes equation (NSE) describes the motion of fluids and is basically an extension of Newtons second law applied to the above mentioned conservations laws, coupled with the assumption that the fluid stress is a sum of, a viscous term (proportional to the gradient of velocity) and a pressure term. The NSE is a second order differential equation that solves for the velocity field, i.e. the velocity of a fluid at a given point in time and space [44].
In its most general form the NSE takes the form of

$$\rho\left(\frac{\partial \boldsymbol{v}}{\partial t} + \boldsymbol{v}\cdot\nabla\boldsymbol{v}\right) = -\nabla p + \nabla\cdot\mathbb{T} + \boldsymbol{f}, \tag{3.1}$$

where ρ is the density of the liquid, $\boldsymbol{v}$ is the velocity field, p is the pressure, $\mathbb{T}$ is the stress tensor and $\boldsymbol{f}$ represents body forces. It is quite obvious that this equation is a statement of Newtons second law, where the left side describes an acceleration of mass, and the right side is in effect a summation of body forces and divergence of stress (pressure and shear stress) [44].
A few assumptions and generalizations can be made to simplify the NSE. The primary body force acting on a system is gravity (unless external electric or other fields are applied), and when working with microfluidic systems, gravity can be neglected due to the small fluid volume. A *Newtonian fluid* is a liquid in which the stress-strain curve is linear and passes through zero. The proportionality constant is known as the viscosity μ of the fluid. A *incompressible flow* is a fluid flow where the divergence of the fluid velocity is zero i.e. the fluid density is constant within an infinitesimal volume moving in the velocity field.
For an homogeneous incompressible flow of a Newtonian fluid assuming constant viscosity and neglecting body forces, the NSE can then be simplified to [44]

$$\rho\left(\frac{\partial \boldsymbol{v}}{\partial t} + \boldsymbol{v}\cdot\nabla\boldsymbol{v}\right) = -\nabla p + \mu\nabla^2\boldsymbol{v} \tag{3.2}$$

If a constant temperature is assumed, (III) is satisfied and the only remaining equation needed for a full description of the system (since NSE satisfies (II)), apart from specific boundary conditions, is conservation of mass (I). If an incompressible flow is assumed then the density is constant and it follows that

$$\nabla\cdot\boldsymbol{v} = 0 \tag{3.3}$$

Even with the above assumptions and simplifications, there are no general analytical solutions to the NSE. Only when applied to a few very simple systems are analytical solutions available. For most cases the NSE must be solved numerically [44].
Computational Fluid Dynamics (CFD) is often utilized when attempting to solve the NSE for complicated fluid systems. A typical CFD system requires strict definition of geometry and boundary conditions, and uses this information to divide the investigated volume (fluid) into discrete cell (mesh) of appropriate size and shape. When the physical conditions are established (equations of motion, conservation of energy, electrical fields etc.) a simulation is started and the equations are solved iteratively either as a steady state or transient.
An important factor is the discretization method used, as it has to handle discontinuous solutions correctly. A wide range of methods are available, including the finite volume method (FVM), finite element method (FEM), finite

difference method (FDM) and the spectral element method. Each method has distinct advantages depending on the problem to be solved. FVM is often used in solving fluid dynamics simulations as the problem is split into discrete control volumes and hence guarantee the conservation of fluxes. Although greater care must be taken when setting up FEM, the method is also widely used as it is more stable than FVM [45]. In this work FEM is utilized through commercially available software, *COMSOL Multiphysics 4.2* (COMSOL Inc.).
Using COMSOL, fluid dynamics problems can be addressed by using FEM to solve the NSE for a wide range of 2D and 3D geometries and flow conditions. As mentioned earlier, solving the NSE yields the velocity field of the fluid and can consequently be used to help predict flow behavior in the system. This is a powerful tool when designing LOC systems as the influence of geometry and volume flows can be tested before chip production.

3.2 Reynolds Number

Much of the mathematical complexity of fluid dynamic phenomena can be attributed to the non-linear term $\rho\left(\boldsymbol{v}\cdot\nabla\right)\boldsymbol{v}$ (from equation 3.1). This term is also mostly responsible for the lack of general analytical solutions to the NSE. However, in the limit of low flow velocities (which can be highly relevant for microfluidic systems), this non-linear term can be neglected. In this regime of so-called *Stokes* or *creeping flows*, analytical solutions are possible for a number of flow problems [44].
The proper way to determine whether the non-linear term is negligible is by performing a dimensional analysis on the NSE. This is done by expressing all physical variables in units of characteristic scales (such as L_0 for length and V_0 for velocity). If the system is characterized by only one length and velocity scale, the quantities can be written in terms of dimensionless expressions [44]

$$\boldsymbol{r} = L_0\tilde{\boldsymbol{r}} \tag{3.4a}$$

$$\boldsymbol{v} = V_0\tilde{\boldsymbol{v}} \tag{3.4b}$$

This now allows the scales for time T_0 and pressure P_0 to be defined

$$t = \frac{L_0}{T_0}\tilde{v} = T_0\tilde{t} \tag{3.4c}$$

$$p = \frac{\eta V_0}{L_0}\tilde{p} = P_0\tilde{p} \tag{3.4d}$$

By inserting equation 3.4 into the NSE for incompressible flows of Newtonian liquids (equation 3.2) and using the straightforward scaling of the derivatives $\partial_t = (1/T_0)\tilde{\partial}_t$ and $\boldsymbol{\nabla}(1/L_0)\tilde{\boldsymbol{\nabla}}$, the NSE reduces to [44]

$$Re\left[\tilde{\partial}_t\tilde{\boldsymbol{v}} + \left(\tilde{\boldsymbol{v}}\cdot\tilde{\boldsymbol{\nabla}}\right)\tilde{\boldsymbol{v}}\right] = -\tilde{\boldsymbol{\nabla}}\tilde{p} + \tilde{\boldsymbol{\nabla}}^2\tilde{\boldsymbol{v}}, \tag{3.5}$$

where the **Reynolds Number** Re is defined as

$$Re \equiv \frac{\rho V_0 L_0}{\eta}. \tag{3.6}$$

It is now obvious when observing equation 3.5 that for $Re \ll 1$ the term $\tilde{\boldsymbol{\nabla}}^2\tilde{\boldsymbol{v}}$ dominates, whereas for the stead-state, where $Re \gg 1$, the inertia term $\left(\tilde{\boldsymbol{v}}\cdot\tilde{\boldsymbol{\nabla}}\right)\tilde{\boldsymbol{v}}$ is the more important [44].
The Reynolds number is for this exact reason, a good indicator to which physical forces are dominant in the fluid dynamical problem. Consider the limit of low Reynolds numbers, the non-linear NSE is reduced to the linear Stokes equation [44]

$$0 = -\boldsymbol{\nabla}p + \eta\nabla^2\boldsymbol{v}, \tag{3.7}$$

for which numerous analytical solutions can be derived depending on the problem at hand. In general, for low values of Re (below 2040), the flow is considered as being *laminar*, or streamlined [46]. When this occurs the fluid flows in parallel layers with no disruption between the layers. There are no cross currents perpendicular to the direction of flow, nor eddies or swirls of fluids and the fluid flow without lateral mixing [47]. In the case of microfluidics where L_0 is quite small, laminar flow is almost always dominating under normal conditions. Figure 3.1 shows an example of laminar flows in a microfluidic nozzle structure (notice streamlines and flow field).
For large values of Re, inertia becomes dominating and the flow is considered *turbulent* or chaotic. Turbulent flow is characterized by low momentum diffusion, high momentum convection, and rapid variation of pressure and velocity in space and time, leading to vortices and unpredictable local flow behavior. Turbulent flow is normally a macroscopic phenomena and is not considered further in this work.

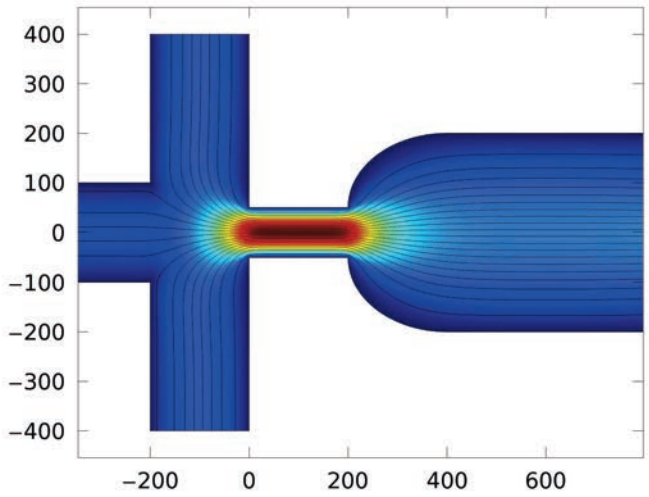

Figure 3.1: The result of a 2D COMSOL simulations of a narrow flow junction, showing streamlines and velocity field in a droplet formation nozzle.

3.3 Hydrodynamic Focusing

In this section 2D hydrodynamic focusing is investigated in more detail. Hydrodynamic focusing is a key technique used widely throughout this work and it is essential that a thorough investigation into the effect is conducted. This is done on a one-layer microfluidic chip, using a simple two sidechannel geometry (see figure 3.2).

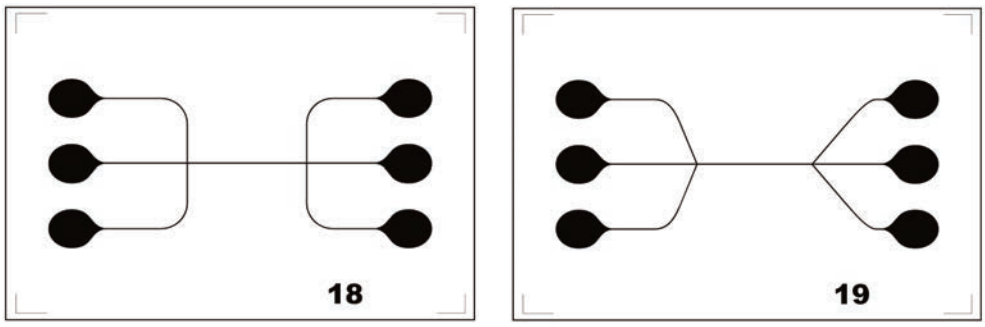

Figure 3.2: Chip design 18 (with 90° side flow angles) *(left)* and design 19 (with 67.5° and 45° side channel angles, respectively) *(right)*.

Previous investigations of similar geometry have mainly focused on flows in high aspect-ratio T-junctions (both for gases [48] and liquids [49]) and have shown that angles between sample and side channels have some influence

on concentration gradients and mixing. Therefore, the local geometry of the channel-junction is investigated, especially the influence on the hydrodynamic focusing and, consequently, long-range divergence of the sample stream. This is of interest since many designs utilize the entire length of the channel either for flow processing or various measurements, and stable focusing is desirable.

3.3.1 Theoretical Analysis

In this section, current theoretical models [50] are applied to hydrodynamic behavior in rectangular microchannels, in order to predict the width of a hydrodynamically focused sample stream in a two-flow system (see figure 3.3 *left*). It is assumed that all liquids are Newtonian and have equal density (ρ) and viscosity (η). Furthermore, all channels have the same height (h) and square cross-sections ($w \cdot h$). All flows are in effect steady and laminar since the Reynolds number in the current geometry and flow conditions is between 10 and 40, depending on the exact flow conditions.

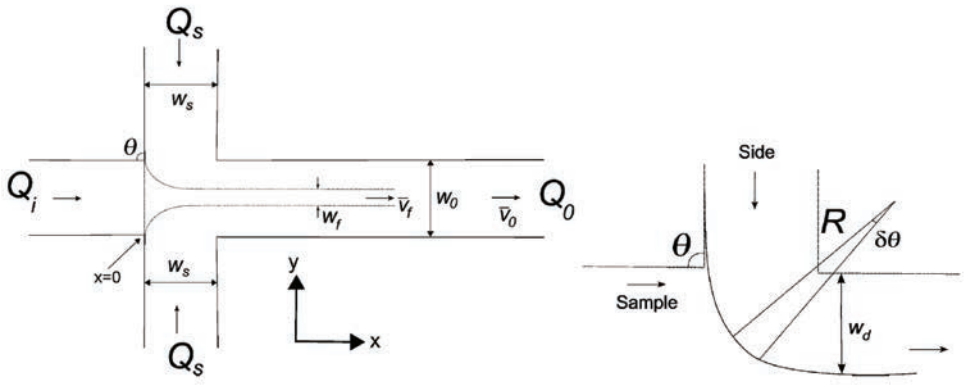

Figure 3.3: Schematic drawing of flow focusing geometry *(left)*, and geometry of the bend side flow during focusing *(right)*.

From the conservation of mass (and figure 3.3) the focusing fraction f can be found as [50]:

$$f = \frac{w_f}{w_0} = \frac{1}{\lambda} \cdot \frac{Q_i}{Q_i + Q_S + Q_S}, \tag{3.8}$$

where Q_i and Q_S are the volume flow rate of the sample inlet and side channels, respectively. The mean flow speed ratio $\lambda = \overline{v}_f/\overline{v}_0$ is an unknown parameter. The flow fraction is defined as the relative volume flow fraction

between side and sample flows $r = Q_S/Q_i$. In order to predict the width of the focused stream (w_f) in equation 3.8, the velocity ratio λ must be determined. This is done by solving the NS equation for the system. As mentioned earlier, in most cases the NS equation does not have an analytical solution and has to be solved numerically. This can be done using finite-element modeling (FEM) in COMSOL.

The angle θ's influence on the hydrodynamic focusing effect, is of particular interest in this system. Based on the above, a very simplistic model for the effect of θ on f can be derived. This is done by neglecting 3D effects and velocity profiles across the flows and by considering the change in momentum undergone by the side flow as it turns the corner into the output channel. This change in momentum leads to a pressure difference between the inside and outside of the flow, which is impressed on the sample flow. Furthermore, approximating the trajectory of the side flow as a circular arc, an estimate of this pressure can be derived via the centripetal force from the side fluid on a small section of the side flow, as it rotates through a small angle $\delta\theta$ with radius of curvature R (see figure 3.3 *right*) [19].

$$\frac{m\bar{v}^2}{R} = \frac{(\rho w_s h R\delta\theta)(\bar{v}_f r)^2}{R} \tag{3.9}$$

Here the average velocity of the sheath is found using r, the volume flow ratio. This force is applied across an area of $hR\delta\theta$ and so the excess pressure exerted at the sheath-sample interface is

$$P_{centripetal} = \frac{\rho\bar{v}_f^2 r^2 w_s}{R} \tag{3.10}$$

An exact expression for R is difficult to determine as the curve is not really a circle. On average though, if the circle, defined by using the side-sample interfaces at the input and output flows as tangents, (see figure 3.3 *right*) a radius can be obtained [19]

$$R = \frac{w_d}{\sin\theta}\left(\frac{1}{\sin\theta}\right) = \frac{w_d}{\sin^2\theta}, \tag{3.11}$$

which leads to a pressure of

$$P_{centripetal} = \frac{\rho\bar{v}_f^2 r^2 w_s \sin^2(\theta)}{w_d} \tag{3.12}$$

This pressure is in addition to the base pressure difference for the side flow, from input to output. This difference is found by applying Bernoulli's equation [41] to the side flow, to give

$$P_{Bernoulli} = \frac{3}{2}\rho\bar{v}_f^2 r^2, \tag{3.13}$$

where f is assumed to be very small.
The effect of the total pressure $P = P_{centripetal} + P_{Bernoulli}$ on the sample can now be determined. By setting the output as zero pressure, Bernoulli's equation for the sample flow can be written as

$$P + \frac{1}{2}\rho\bar{v}_f^2 = \frac{1}{2}\rho\frac{\bar{v}_f^2}{f^2} \tag{3.14}$$

And so the focusing fraction f can be expressed as

$$f = \sqrt{\frac{1}{1 + \frac{2P}{\rho\bar{v}_f^2}}} \tag{3.15}$$

Substituting these pressures (equation 3.12 and 3.13) into equation 3.15 gives

$$f = \sqrt{\frac{1}{1 + 3r^2 + 2r^2\sin^2\theta}} \tag{3.16}$$

which can now be used to estimate the flow fraction f as a function of either angle θ or flow ratio r [19].
This is a very simple model of the flow, which takes no account of 3D behavior or of the velocity profiles of the various streams. It deals only with the average inertial forces on the liquids. However, the equation gives a fair approximation to the data and so is of practical use in estimating flow focusing effects in these simple 2D systems.

3.3.2 Experimental

All experiments are done using deionized water in the side channels and deionized water mixed with 5% red food colour as the sample fluid. The side fluids are injected from $10mL$ plastic syringes while the sample fluid is dispersed from a $1mL$ plastic syringe. All three syringes are driven by two syringe pumps. This allows for individual control of volumetric flow of side and sample flows, and in effect the flow ratio r.
The flow in the chip is characterized via images obtained using an optical microscope *(Nikon Eclipse ME600)*, equipped with a CCD camera *(PL-B873-CF, PixelLINK)*. A 10× objective is used. Due to the thickness of the PDMS seal and the limited working distance of the objective, higher magnification is not possible. For image analysis, *SPIP (Image Metrology)* is used to obtain cross-sectional plots of the light intensity. Data fitting and statistics on the data are done in *Origin Pro 8*. An example of a microscope image, cross-sectional line and a fitted curve are shown in figure 3.4.

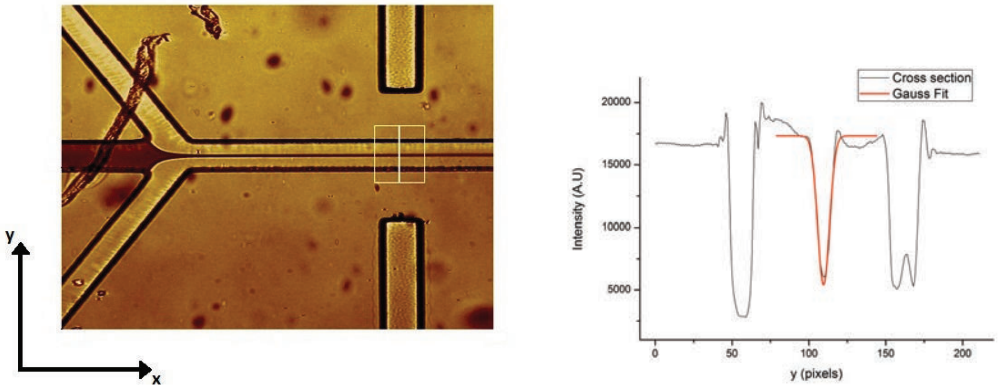

Figure 3.4: Microscope image showing the focused red dye and the cross-section line *(left)*. Plot showing x-averaged pixels cross-sectional scan and the corresponding fitted Gaussian curve *(right)*.

3.3.3 COMSOL Modeling

To interpret the experimental data, numerical values are obtained by finite-element-modeling in COMSOL. A 2D COMSOL model is used to simulate the flow behavior in a microfluidic channel junction. Such a model is mostly sufficient to describe the entire 3D system due to symmetry in the z-direction. This is mainly done due to computational limitations as the amount of finite elements increases drastically when adding a third dimension. Some key calculations are however conducted in a full 3D model to support and expand the presented results.

2D Model

The model geometry consists of a $3mm$ long channel with two side channels forming a junction $0.5mm$ from the inlet end. The angle between sample and side channels θ is parameterized and individual simulations are run for each selected value in the desired range. All channels are $100\mu m$ wide. The geometry is meshed with an ultra fine free triangular mesh (maximum element size $5\mu m$), resulting in around 40000 finite elements.
All liquid flow modeling is handled using the *Laminar Flow* package from the MEMS-module. All liquids are modeled as water at room temperature. No-slip boundary conditions are applied to all side-walls. The three inlets (two side and one sample channel) are treated as laminar inflows with a set flow rate and a long entrance length ($1cm$) to ensure stable laminar flow. The flow rate in the main channel is fixed at $10\mu l/min$, while the side channels are varied from 0.1 to $110\mu l/min$, depending on the desired flow-ratio.

The outlet is fixed at a pressure of $0Pa$. The model equations are solved by finding a stationary solution for the velocity field of all flows.
To visualize the hydrodynamic focusing the *Transport of Diluted Species* package is added to the model. All walls are set to no flux and the diffusion constant to $2.2 \cdot 10^{-11} m^2/s$ (self-diffusion of water). The velocity field is set to $u(y, z)$ from the previous simulation step. The concentration of the virtual sample liquid is set to 0 at side-channels and output, and $1 mol/m^3$ in the input.
After a solution has been obtained, cross sectional plots of the concentration are obtained and treated the same way as those obtained from the CCD images in section 3.3.2. Figure 3.5 show a simulated result with mesh overlayered.

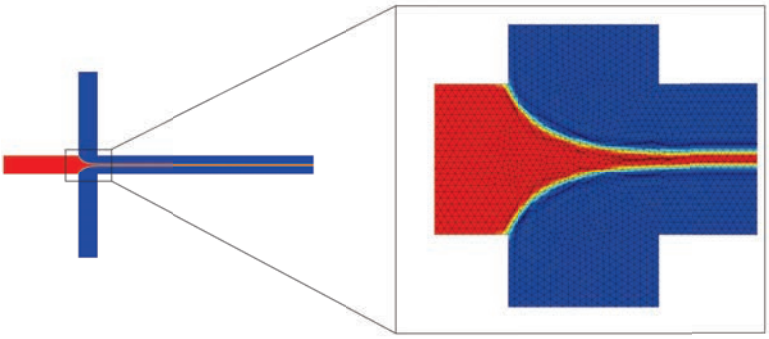

Figure 3.5: 2D COMSOL simulation of flow focusing *(left)*, with close up showing the fine mesh in the junction *(right)*.

3D Model

A limited amount of 3D simulations has also been performed while having access to a dedicated simulation PC. This is done to investigate the exact flow profiles. Simulation results in literature [51, 52] on similar hydrodynamic focusing systems indicate a non-homogeneous flow profile along the vertical axis with a strong dependence on total volume flow.
The simulations conducted in this section are virtually similar to those used in the 2D simulations, except for a great increase in element numbers. All channels are modeled as having a square cross section ($100\mu m$ high). Figure 3.8 shows the result of a simulation on a $\theta = 90°$ junction with $r = 5$. The slices show a clear flow profile change as the liquids move along the channel, but also a very dispersed concentration profile for the artificial sample fluid in the vertical plane. This is in accordance with results from Nasir *et al.* [51] where a slightly hourglass formed profile is obtained in the z-direction. These

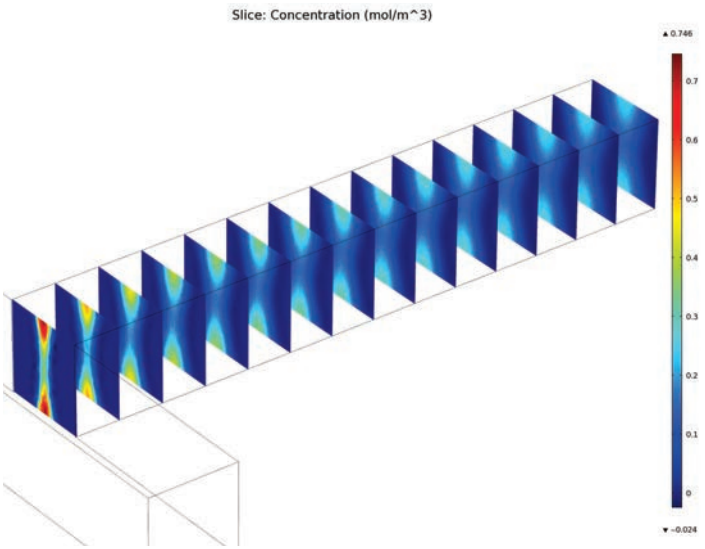

Figure 3.6: 3D COMSOL simulation of flow focusing ($r = 5$) in a 90° junction. Slices showing concentration of artificial sample flow and a distinct hourglass shaped flow profile.

results also indicate that a higher Re increases the amount of sample-fluid pushed towards top and bottom of the channel.
To investigate this phenomena, three simulations are run for constant $r = 5$ and with $\theta = 90°$, but increasing total volume flow. Figure 3.7 show the simulated flow profile (obtained at $x = 100\mu m$) for total volume flows of $11\mu L/min$ *(left)*, $55\mu L/min$ *(middle)* and $110\mu L/min$ *(right)*, corresponding to $Re = 20$, $Re = 102$ and $Re = 204$, respectively. The hour-glass profile

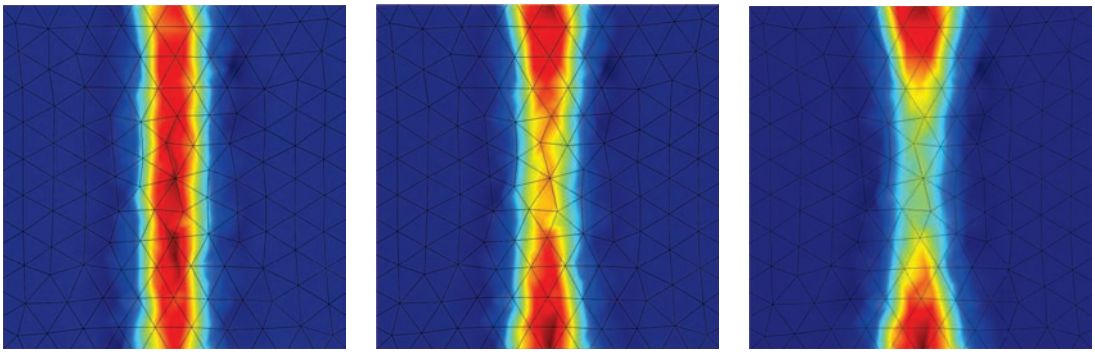

Figure 3.7: Slice from 3D COMSOL simulation of 90° focusing geometry, for various total volume flows (all $r = 5$). *Left:* $11\mu L/min$ ($Re = 20$), *middle:* $55\mu L/min$ ($Re = 102$) and *right:* $110\mu L/min$ ($Re = 204$).

show a clear dependence on Re, but is however less pronounced than in a one side channel geometry [51]. None the less, the results are highly interesting and should be taken into consideration when utilizing hydrodynamic focusing.
Two further simulations are run to investigate the effect of θ on the 3D flow profiles. This is done by directly comparing the obtained profiles for $\theta = 90°$ and $\theta = 45°$ at two different flow ratios ($r = 2$ and $r = 9$). The four resulting profiles are plotted in figure 3.8. For $r = 2$ *(left)*, the difference is minimal,

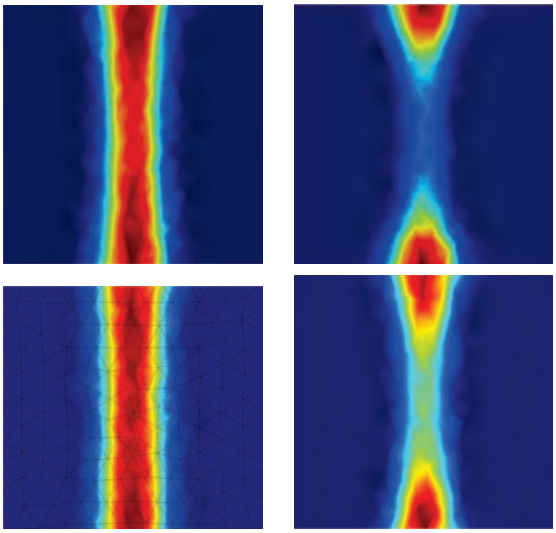

Figure 3.8: Slice from 3D COMSOL simulation, obtained just after the junction, for 90° junction *(top)*(with $r = 2$ *left*, $r = 9$ *right*) and 45° junction *(bottom)* ($r = 2$ *left*, $r = 9$ *right*). Sample flow $10\mu L/min$ for all plots.

but still noticeable with the 90° junction *(top)*, having a slightly more curved profile. For $r = 9$ *(right)* the difference is bigger and again more pronounced for the 90° junction. Both profiles are, however, highly hourglass shaped in accordance with the investigations regarding the influence of Re.

3.3.4 Results

Influence of r on f

The first experiment focuses on investigating how the volumetric flow rates of side (Q_s) and sample (Q_i) fluids influence flow fraction f. This is expressed as a function of the flow-ratio of the system (r). For this purpose a simple hydrodynamic focusing chip is used (figure 3.2 *left*). Images are obtained for flow ratios from $r = 0.01$ to $r = 11$, and analyzed. The width of the

sample flow w_f is measured at a distance of $x = 500\mu$m (see figure 3.3) and is defined as the full-width-half-max (FWHM) of a Gaussian fit to the peak in a cross-section of the light-intensity of the image (see figure 3.4) [19].
An identical structure is recreated in COMSOL and using identical parameters for volumetric flow and geometry, the hydrodynamic focusing has been modeled in a 2D cross-sectional view. Data points are obtained by extracting the intensity data of a virtual colored liquid in the sample flow and then calculating the FWHM from a Gaussian curve fit.
Finally, the flow fraction f is calculated for different values of r based on equation 3.16. The results from all three methods are shown in figure 3.9 [19].

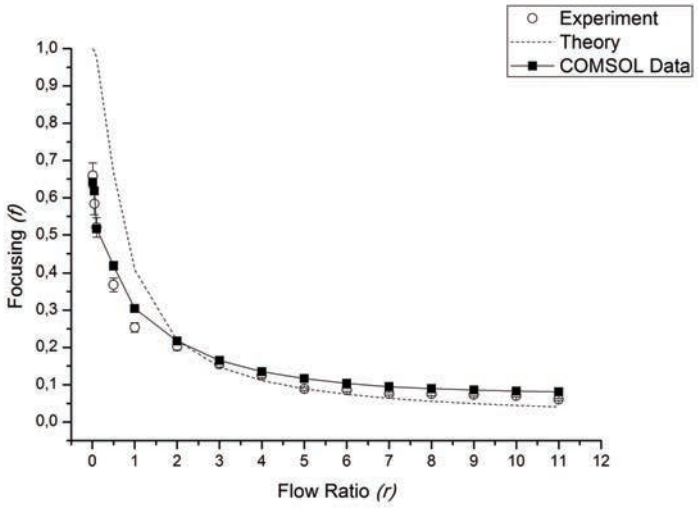

Figure 3.9: Focusing fraction f in a 90° junction, data measured as the FWHM of a cross-sectional cut as a function of increasing flow ratios (r). Experimental data, modeled COMSOL data and calculated values are plotted.

A clear correlation between all three sets of data is visible. The behavior of $f(r)$ agrees with the results found by Lee *et al.* [53] and general observation throughout all experiments. The focusing fraction f decreases from 0.65 down to 0.10 with increasing values of r (figure 3.9). Obviously, efficient hydrodynamic focusing only occurs for $r > 1$, meaning that the side-channel flow (Q_s) must always be at least equal to or bigger than the sample flow (Q_i), in order to achieve focusing. A non-linear behavior is apparent and shows that for higher values of r, a further increase has little or no influence on the hydrodynamic focusing. At low r however, the effect is quite pro-

nounced [19].
When comparing the calculated values (based on equation 3.16) with the experimental data and numerical simulations we see fair agreement particularly at higher values of r. The agreement is further off at low r where the side fluid undergoes greater acceleration than assumed in the calculation.

Influence of θ on f

The experiments in this section investigate how the geometry of the channel junction affects the hydrodynamic focusing effect. More precisely, how different values of the side- and main-channel angle θ affect the focusing fraction f.
A constant flow ratio of $r = 6$ is selected, mainly because it is sufficiently high to give good focusing and is thereby a realistic value for use in experimental setups. As in the previous section, the chip is mounted in a microscope-setup and images of the flow behavior are obtained during focusing in each of the three different channel-junctions (figure 3.2). The images are analyzed using *SPIP* and *Origin Pro 8*, and the averaged width of the focused stream w_f is measured at points along the main channel. The measured values are converted to micrometers based on a profilometric measurement of the channel width. The results are plotted in figure 3.10.

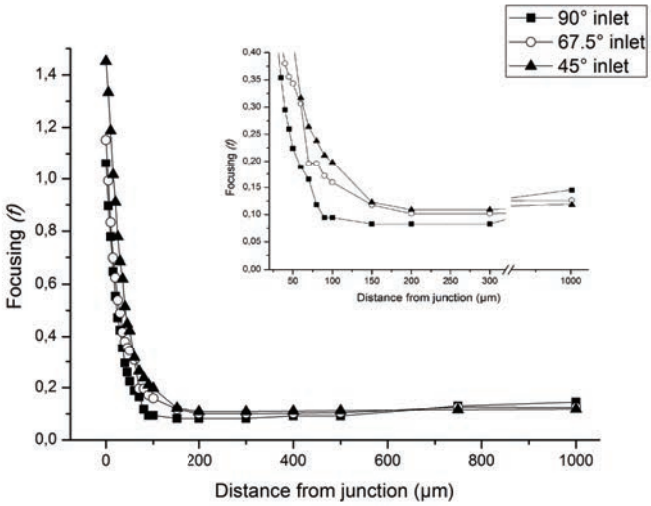

Figure 3.10: Focusing fraction f as a function of distance from the junction for $r = 6$, showing the rapid decrease in width along the channel and a stabilization-effect after $100 - 200\mu m$. Close-up of the area of particular interest. Shown for three values of θ.

A clear tendency to rapid focusing is observed for all three angles. Within $100 - 200\mu m$ of the junction the width of the sample flow has decreased by a factor of 10 and remains constant thereafter. The close-up on figure 3.10 also reveals that the lowest absolute value for f (0.083) and maximum flow focusing is obtained with the 90° angle design. As θ becomes lower, f_{min} increases, up to 0.109 for 45°. For all three angles the minimum value is obtained around $200\mu m$ from the junction. Towards 1000 μm f increases slightly for all three values of θ [19]. The results are summarized in table 3.1.

Angle θ	Minimum f	f at $1000\mu m$	% increase
90°	0.083	0.145	42.7
67.5°	0.102	0.125	18.4
45°	0.109	0.119	8.4

Table 3.1: Focusing fraction f from measured FWHM, for three different angles at different positions along the main channel.

It is noted that the f value increases with increasing distance from the junction. The effect is slightly increased for the flow that has been focused down to the smallest value. Over the first millimeter, the flow width in the 90° side-channel chip increases by 42.7%, while the 45° design only induces a 8.4% increase in width. This long range behavior will be investigated further in the next section.
The influence of the angle on focusing is further investigated using numerical modeling (in COMSOL). The model used in the previous section is maintained and a parametric sweep of θ is added. The flow ratio is maintained at $r = 6$. Focusing fraction f is obtained by using the FWHM value of a Gaussian curve fit of the individual data-sets measured $200\mu m$ from the junction [19]. The results are shown in figure 3.11. The simulations show a steady decrease in f as the θ is increased toward 90°, corresponding to a 55% reduction in f between the smallest and largest angle. The three experimental points obtained at this value of r are also added to the plot and seem to agree reasonably well with the simulations.
The simple theoretical model introduced in equation 3.16 to calculate f (*Theory* curve in figure 3.11) produces poor correlation with the numerical simulation and experiment. As discussed previously this model introduces a number of simplifications. Most notably it takes no account of 3D behavior like the hourglass profiles discussed in section 3.3.3. This profile increases the apparent width of the focusing as seen through top-down imaging and would explain the discrepancy of the calculated with the observed width.

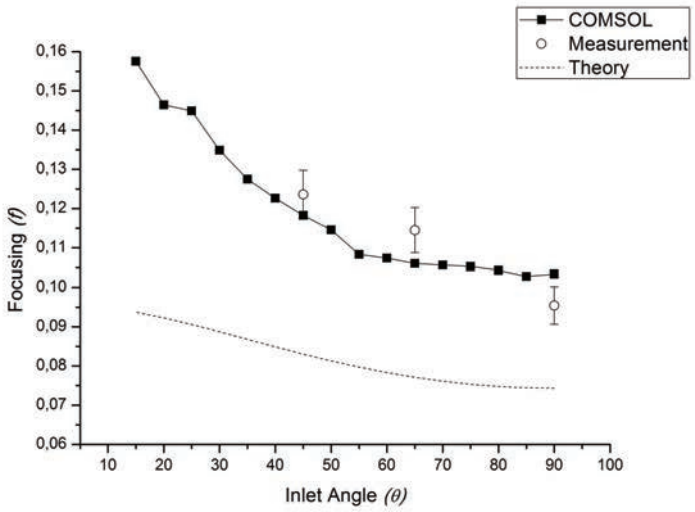

Figure 3.11: Focusing fraction f as a function of angle θ between side and sample channels, for $r = 6$, from COMSOL model (filled squares). Experimental results (open circles) are shown for comparison. Also shown is calculated data based on the modified Bernoulli's equation (dotted line).

It cannot however account for the discrepancy between the calculation using equation 3.16 and the COMSOL model, which is also 2D and produces a closer fit to the data. It is more likely that another assumption such as that of a flat velocity profile across the channels is responsible for the difference. Nevertheless, the trend given by the simple equation is quite similar to the COMSOL model and suggests that the pressure due to redirection of the side flows is a factor in determining the short range focusing behavior.

Long-range flow behavior

The previous section indicates that the angle θ has an influence on the hydrodynamic focusing effect, and in turn f. Clearly a side-channel angle of 90° produces the biggest reduction in the sample flow width immediately after the junction (w_f). However, they also show in figure 3.10 that the degree of focusing further along the channel varies for the different angles.
In order to investigate the above effect, the focusing fraction f is measured along a $1cm$ long channel for two different angles ($\theta = 45°$ and $\theta = 90°$). The measurements are replicated on six different chips (three for each angle) in order to eliminate random variation in the chip production method. The influence of r is also investigated for values of $r = 3, 6, 10$, as they represent a wide spread of focus widths w_f (see figure 3.9). Images are obtained for all

three values of r, and for both angles, along the $10mm$ of the main channel. Mean values for f are plotted in figure 3.12, with error bars indicating the sample standard deviation of all three measurements [19]. The tendency observed in the previous experiment is consistent with this experiment, for all three values for r. The measurements indicate that f is considerably smaller for $\theta = 45°$ for a wide range of distances, for all three values of r. In all three series of measurements the data supports the previous results, where the minimum value of f is found near the junction and in the perpendicular design. At the far end of the channel there is a crossover and the perpendicular design again provides the best focusing (smallest value for f). The region of interest is however the one ranging from $1mm$ to $5mm$, where an interesting effect occurs.
This observed effect can be attributed to a sum of different effects [19]. As observed in section 3.3.3, the hourglass shaped flow profile depends on both Re and to a lesser degree θ. As Re is constant in each of the three measurements, the observed effect can to a certain extend be attributed to the influence of θ. Since the hourglass profile is less pronounced for a lower angle, a top-down measurement would make the focused flow appear slightly smaller. This is however not enough to account for the big difference in long range flow behavior. While diffusion of the color molecules used to map the flows does have a diffusion length of around $4.5\mu m$ for the current setup, this effect should be the same for both flows [19].
Apart from the 3D flow profile, the observed effect can be attributed to a Venturi-like effect [19]. As the 90° design results in a tighter focus (smaller f) a bigger pressure gradient across the channel is expected, compared to the 45° design. When this pressure equalizes the focused stream expands, which is observed in the measurements.

Overall, the results presented in this chapter are quite significant, since it is often of interest in lab-on-a-chip systems to utilize the entire length of the chip for different measurements or further flow processing. Hence it is important to be aware of the fact that the effective size of the focused flow might change along the channel, as well as being careful regarding using too high total volume flows, as this enhances the hourglass profile that in effect pushes the sample away from the central axis of the channel.

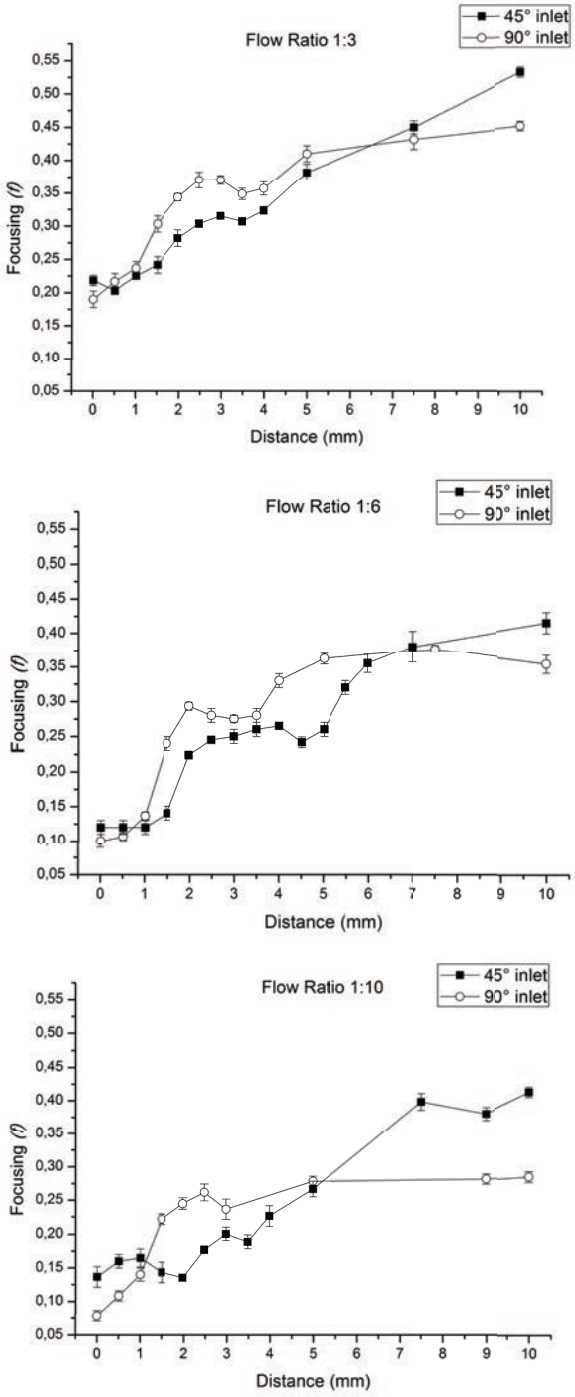

Figure 3.12: Focusing fraction f along the channel for both 45° and 90° side-channel angles for three values of r (3, 6 and 10).

Chapter 4

Flow Cytometry

In this chapter flow cytometry (FCM) will is investigated. While there are many aspects to this technique, and commercial flow cytometers (FC) require extensive knowledge and experience to operate, the goal of this project is to develop a microfluidic LOC device capable of the same core-abilities as the macroscopic, expensive and sophisticated modern FC machinery.
The main focus of this chapter is experimental results, which in turn are heavily tied to the development of the optical detection system (see section 2.2). After a short introduction to the basics of FCM, results for a variety of suspended samples are presented, along with a discussion of the outcome and limitations or problems with the specific samples.

4.1 Basics of Operation

Traditionally FCM is a widely used method for analyzing cellular surfaces, intra-cellular molecules or bacterial populations in order to define specific populations, assessing the sample purity or determining cell size and volume. This is done by analyzing suspended samples on a single event basis, usually as the final step following specific biological staining and selection protocols. The FC uses 3D hydrodynamic focusing and injects the suspended sample through a nozzle into a capillary where a buffer is used to focus the stream into a thin thread. The sample is then passed by one (or several) laser sources where each cell/bacteria is excited by the laser and at the same time scatters the laser light. Three types of light are usually detected; fluorescent light (FL), forward scattered light (FSC) and sideways scattered light (SSC) [17]. This basic principle is shown in figure 4.1.

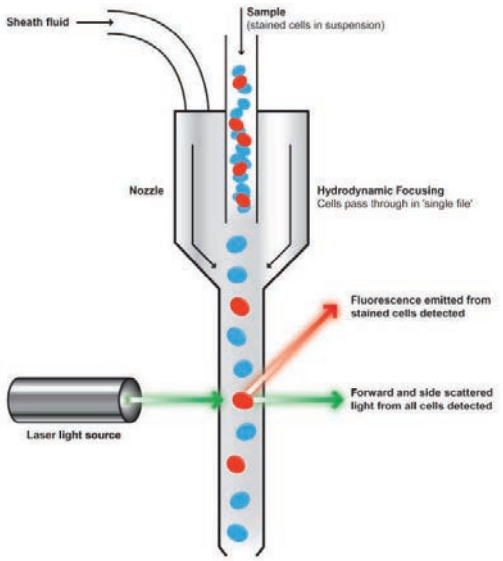

Figure 4.1: Schematic drawing showing the basic working principle of flow cytometry.

All emitted and scattered light is then collected (as discussed in section 2.2) and can then be analyzed to give a complete, although complex, picture of the investigated sample. In general, the optical signals contain the following information [17]

- FSC - This signal correlates mainly to the sample size.
- SSC - Depends on the sample density and contains information about granularity or homogeneity of the sample.
- Fluorescence - Depends entirely on use of fluorescent staining and can be used to identify specific targets via DNA or anti-body stains. Staining with multiple fluorescent dyes are often used for more advanced measurements.

The optical signals for each individual sample are measured simultaneously (triggered electronically by either scatter signal) and thus require at least three separate detectors. Modern FC's have multiple laser sources and whole arrays of detectors for individual fluorescence lines and scatter signals. This requires advanced optical setups splitting the light correctly, similar to those described in section 2.2. Optical signals are converted into electrical ones using photo-multipliers, capable of detecting and amplifying single photons.

Commercial FCM uses advanced software for data analysis and signal plotting, utilizing gated signals to compare and distinguish samples [17]. Figure 4.2 shows an example obtained on a commercial FC.

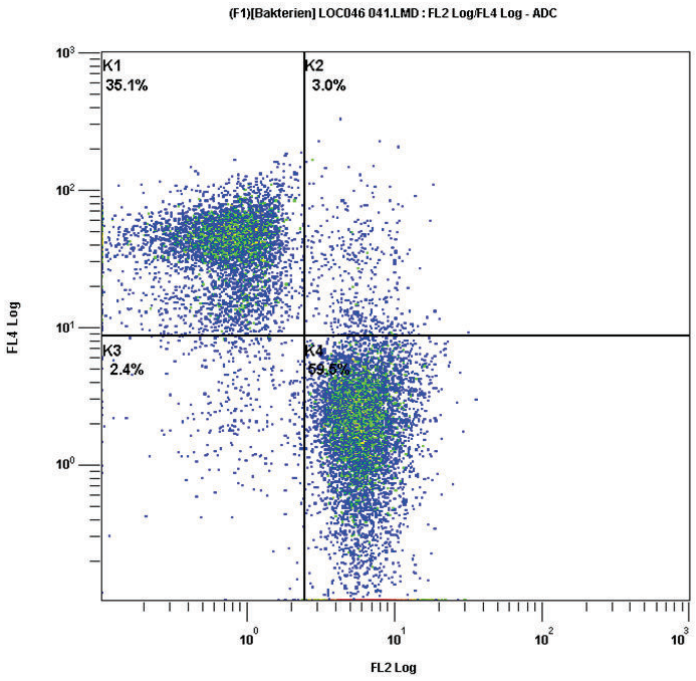

Figure 4.2: FC measurement on Listeria bacteria, performed on a commercial FC, showing two sample populations separated by their fluorescence and scatter signals. By Jan Lenke, FH-Flensburg.

While the optical setup used in this work is in principle similar to that used commercially, it is limited to one laser source and correspondingly one fluorescence signal. Furthermore, due to the unique 2D detection setup in the LOC device itself (described in detail in section 2.2), only one mixed scatter signal is obtained. Since the pickup optical fiber is positioned at an angle to the optical axis, the signal measured is not simply FSC. Since it is also not positioned perpendicular to the sample flow, the signal is also not SSC. In effect, the scatter signal measured by the photo-diode in the LOC setup is a mixed signal containing both information about the size of measured samples, but also to some degree density and granularity information.
In the following sections results are presented for various samples types, all obtained using the microfluidic device and optical setup described in chapter 2.

4.2 Polymer Beads

Fluorescent beads are stained polymer spheres (most often poly-styrene (PS)) used in commercial FCM or other scientific methods requiring narrow and precise size distribution and emission wavelengths. These beads are characterized by very high fluorescent intensities as the fluorescent molecules are embedded throughout polymer spheres. A number of different beads are available for experiments and are used for initial testing of the microfluidic FC setup developed in this work.

Two distinctly different bead-types are used in the first experiment. Mainly, $6\mu m$ wide PS fluorescent coated beads are use (*Red Fluorescent Polymer Microspheres*, Duke Scientific Corp.). They are easily excited by the $488nm$ laser light and emit strong yellow fluorescence (centered around $550nm$). A dilute solution is prepared (concentration unknown), by mixing the beads (in powder form) in water that contains 5% *Tween-20*. This is a surfactant that helps prevent the polymer beads from sticking together and to the PDMS channel walls. The solution is sonicated for $10min$ to break up any larger aggregates. The sample is delivered to the microfluidic chip via a $1mL$ syringe. Two $5mL$ syringes containing pure DI water (also with 5% *Tween-20*) are used as sheath fluids. Sample and sheath volume flows are controlled seperately using two syringe drivers. The second sample is prepared in a similar way and consists of $8\mu m$ PS beads with no added fluorescence (*PPS* $8\mu m$ *- PS Microparticles*, G. Fisker Gbr.).

A design similar to *design 29* (see figure 2.22) is used hereafter. The chip contains three inlets (one sample, two sheath flow) and guiding channels for input and output fibers. According to the results in section 2.2, the optical output channel is angled with respect to the optical axis, and a separate channel system allows for injection of index matching liquids to increase the amount of detected light.

The sample is dispersed at $10\mu l/min$ and sheath flows at $30\mu l/min$, resulting in a flow ratio of $r = 3$, which should yield proper hydrodynamic focusing. Due to the sensitive nature of the detection setup and its electronics, great care must be taken to optimize signals before each experiment. Most importantly, the optical input fiber that guides the laser light, has a $4\mu m$ wide core, and thus must be aligned very precisely to avoid any drift in the signal during measurements.

Figure 4.3 shows the scatter-plots obtained for both types of PS beads. The plots are superimposed for easier comparison. Around 1000 points are plotted for each measurement and the count rate for each run is between $30Hz$ and $50Hz$. Figure 4.4 shows the same data presented as histograms.

Firstly, when comparing the photo-diode signal (measuring the scattered

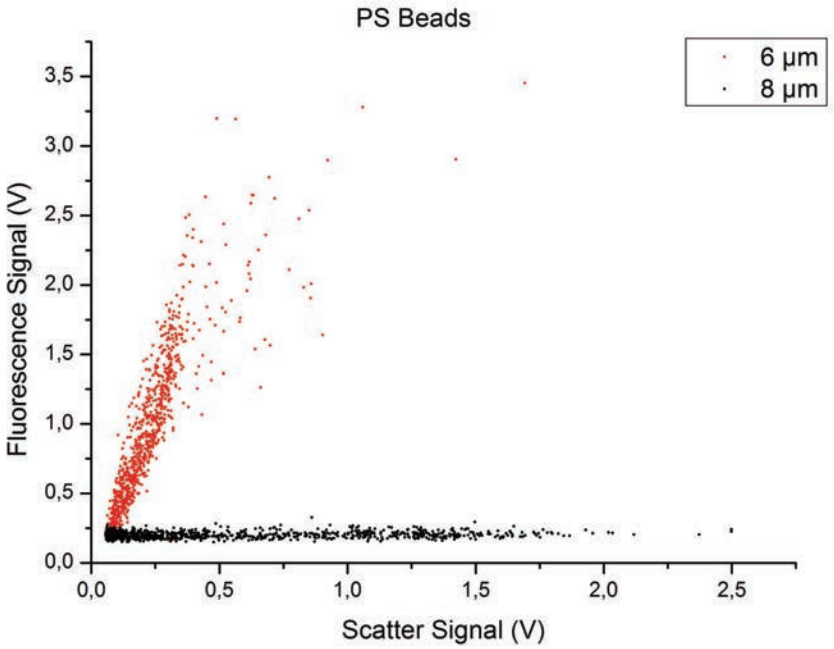

Figure 4.3: Superimposed scatter plot of two types of PS beads ($6\mu m$ fluorescent and $8\mu m$ non-fluorescent).

laser light), a clear difference is observed. Since the measured signal is a mix of both FSC and SSC, it potentially contains a lot of information. However, as both samples consist of PS beads, their density and granularity can be assumed to be similar and the difference in signal strength is only an effect of the difference in size. As expected, the bigger $8\mu m$ wide PS beads result in a bigger scatter signal, due to a 42% bigger volume. Quite a big spread in signal is observed, especially for the larger $8\mu m$ beads.
As for the fluorescence signal, the non-stained $8\mu m$ beads show a very low signal, indicating a complete lack of fluorescence from the beads apart from background noise. The stained $6\mu m$ beads on the other hand, show a large fluorescence signal on the PMT. Even though the signal has some spread, it is still quite distinct, especially when compared to the non-fluorescent $8\mu m$ beads.
As a further test of the system the two solutions of beads are now mixed together in a $1:1$ ratio and run through the setup using the same parameters as above. The resulting measurement is shown in figure 4.5. On the plot, two distinct populations are clearly visible, corresponding fairly well in both size and shape to the two superimposed measurements in figure 4.3. While a bigger spread is noticeable on the fluorescence and scatter signal, the overall

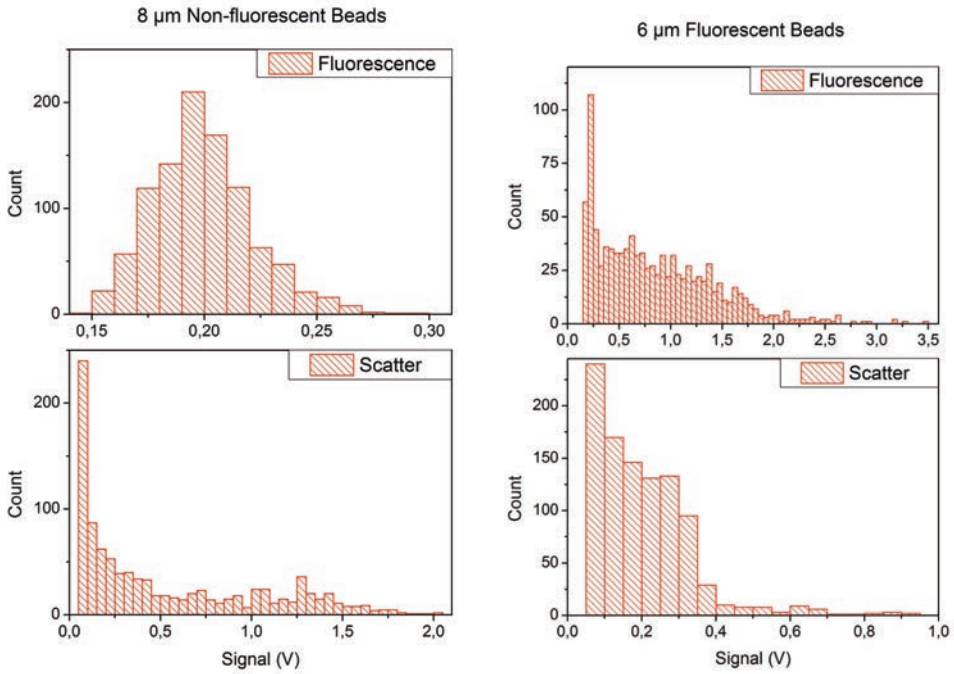

Figure 4.4: Histograms showing the fluorescence *(top)* and scatter *(bottom)* signals from PS bead measurements ($8\mu m$ - *left* and $6\mu m$ - *right*).

picture is quite clear and based on the measurements it is possible to distinguish the larger $8\mu m$ non-fluorescent beads from the fluorescent $6\mu m$ beads. From the plot it can be deduced that the $1:1$ mixture contains more $6\mu m$ than $8\mu m$ beads.

4.2.1 Calibration Beads

In order to test the relative sensitivity of the setup, flow cytometry is also conducted on commercial calibration beads (*Sphero FITC Cablibration Particle Kit*). These beads contain a certain specified amount of fluorescent dye (in this case *fluorescein isothiocyanate*(FITC)) and is therefore a better test of the system sensitivity compared to the previous experiment, which is purely a positive/negative result. Similar concentrations of bead solutions are prepared by adding two drops of concentrated bead-solution to $1mL$ DI water containing 5% Tween-20. The two solutions (labelled *Peak 2* and *Peak 4*) are then mixed $1:1$ and investigated in the experimental microfluidic FC setup. As in the previous experiement, sheath flows of 5% Tween solution is used, at a flow ratio of $r = 4$. The measured result is plotted in figure 4.6.

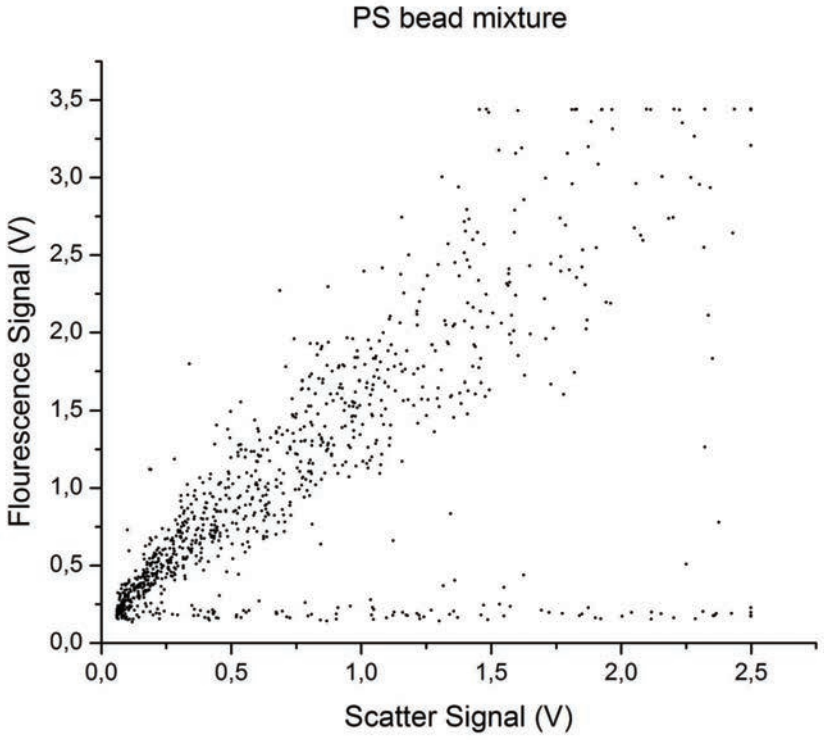

Figure 4.5: Scatter plot showing FC measurement on mixture of $6\mu m$ and $8\mu m$ PS beads.

The results are plotted on a double log-scale for easier comparison. Two populations are clearly distinguishable in the plot, both with comparable scatter signals. This is expected as the two bead types are identical in size $(3 - 3.4\mu m)$, shape and density. The difference in fluorescence signal is significant. One population spans a range of $0.5 - 1V$, while the other ranges from $2.5V$ to $5V$. Figure 4.7 *(left)* shows the peak intensities provided by the manufacturer, and shows the signal intensity difference between peak 2 and 4 are about one order of magnitude. A histogram showing the same peaks from the FC measurement is plotted for comparison (figure 4.7 *right*). While the difference between the two measured peaks are slightly less than an order of magnitude, the difference is still quite large, and confirms that the microfluidic FC setup is capable of distinguishing different levels of fluorescence from a single sample.

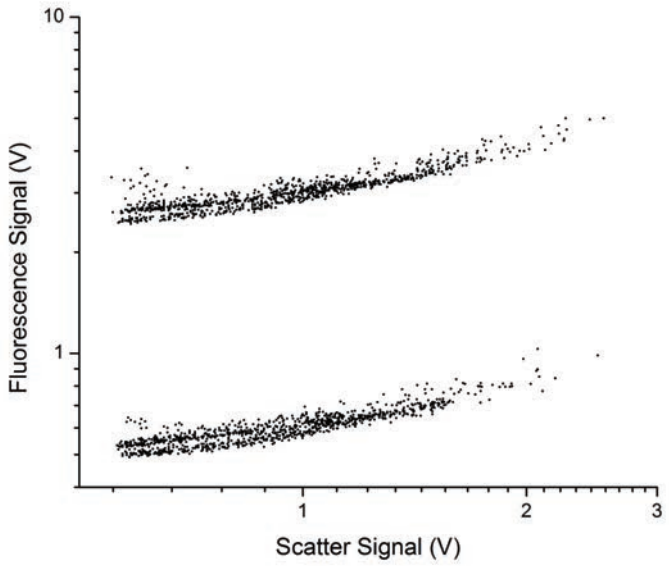

Figure 4.6: Scatter plot showing the results from FC measurement on commercial calibration beads with two distinct fluorescence populations.

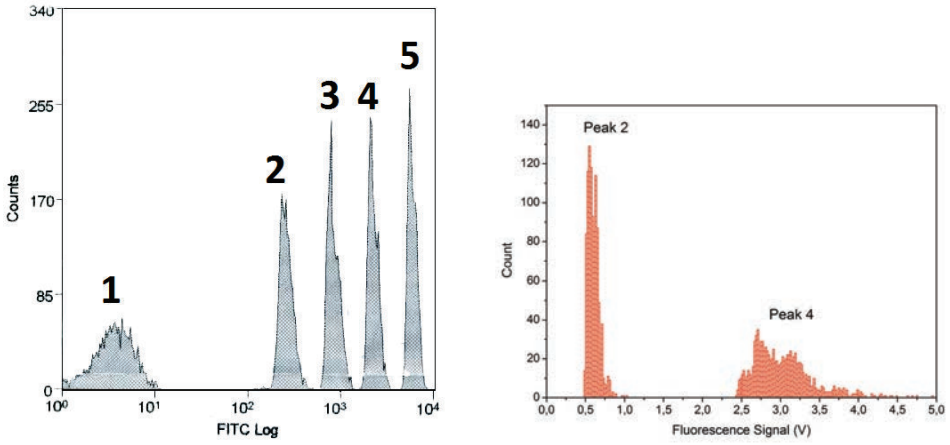

Figure 4.7: Fluorescence peak values provided by manufacturer *(left)*, compared to measured results *(right)*.

4.3 Bacteria and Micro-organisms

4.3.1 Yeast Cells

To test the setups ability to detect and distinguish biological samples such as bacteria, yeast cells are as an initial model system. Yeast is an extremely well understood and described family of eukaryotic micro-organisms that form unicellular cultures. Baker's yeast is selected as it is easily attainable and completely harmless. Baker's yeast has a typical size of $5\mu m$ for a single cell and is provided in an active dry form. To activate the yeast-cells for use, $70mg$ is added to $10mL$ lukewarm $(30 - 40°C)$ water, along with $200mg$ of white sugar. The solution is then mixed on a vortexer and allowed to rest for at least $15min$ for the yeast to become properly active.
A $1mL$ sample is delivered to the system using pure DI water as sheath fluids. In the first experiment the effect of hydrodynamic focusing on detection signals, is tested. Figure 4.8 shows the photo-diode signal intensity, giving the scatter spread on a unfocused *(left)* and focused *(right)* measurement. In both cases the sample flow is $10\mu L/min$, and in the focused run, a flow ratio of $r = 4$ is used. For both measurements around 50000 events are recored. The results clearly show the positive effect of using hydrodynamic

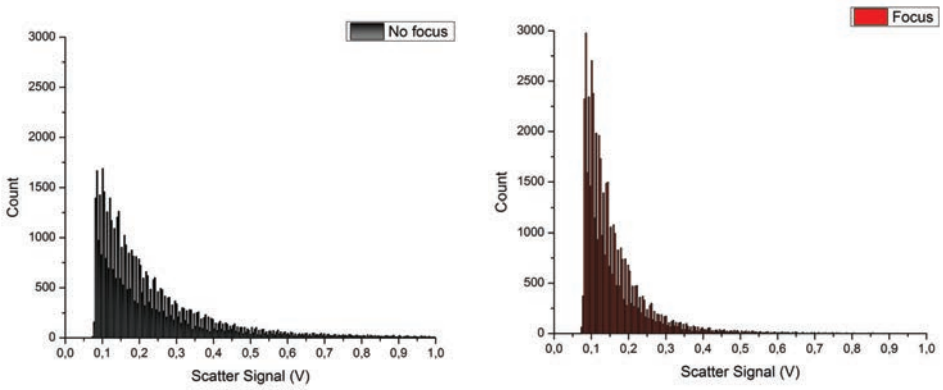

Figure 4.8: Histograms obtained from FC measurements of unstained yeast cells, showing the effect of unfocused flows *(left)* vs. hydrodynamic focusing *(right)*.

focusing, resulting in a narrower and more well-defined scatter peak. Figure 4.9 shows a typical scatter plot for a sample containing unstained yeast cells (with hydrodynamic focusing).
In order to fully test the setup with biological sameples, the yeast cells are stained with a fluorescent dye. Propidium iodide (PI) is used for this purpose. PI has red fluorescence when excited by $488nm$ light and is a DNA-stain.

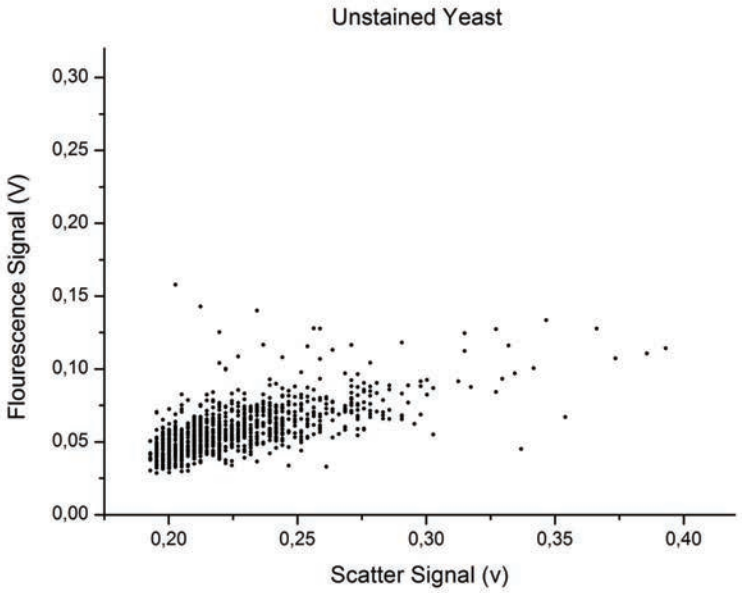

Figure 4.9: Scatter plot of FC measurement of unstained yeast cells.

This means that it is typically used for vitality-stains, since only non-vital cells have open membranes that allow the PI to enter the nucleolus and stain the DNA contained within [17]. To lyse the yeast cells and stain with PI, the following procedure is used (for $0.5mL$ activated yeast solution)

1. Mix with $0.5mL$ cold ethanol (96% C_2H_6O) and sonicate for $5mins$
2. Centrifuge for $5min$ at $2000rpm$ and dispose of supernatant
3. Re-suspend in $1ml$ $50mM$ Na-citrate ($Na_3C_6H_5O_7$) + $25\mu l$ PI (final concentration of PI $0.125mg/ml$)
4. Vortex and rest for at least $5min$

For comparison a $1:1$ mix of stained and unstained yeast cells are made. Figure 4.10 shows a microscope image containing the cells. The red PI fluorescence is excited by a Hg-lamp. While a faint blue auto-fluorescence is detectable from the unstained yeast-cells, the red stained cells clearly stand out. As the Hg-lamp has a lot lower intensity than any laser, the images are obtained using considerably long integration time ($> 5s$).
To establish a connection to the results from the previous section, a comparison is now made with the fluorescent PS beads. This is done by attaching a spectrometer on the optical filter cube, replacing the PMT. The filters ensure that only the fluorescent signal is measured. A solution containing stained

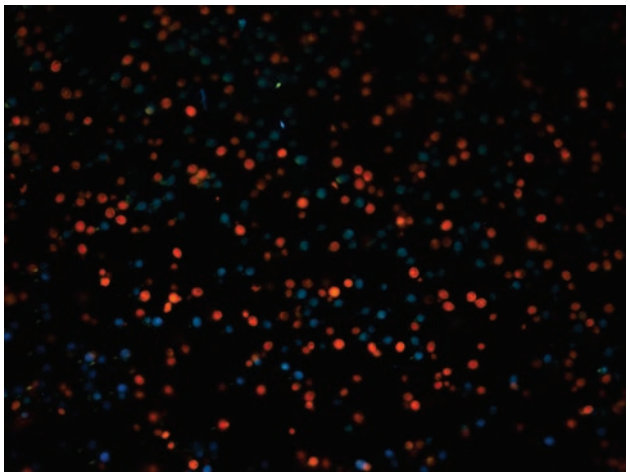

Figure 4.10: Microscope image showing stained (red PI) and unstained yeast cells mixed together. $50x$ zoom, obtained at long integration time ($> 5s$).

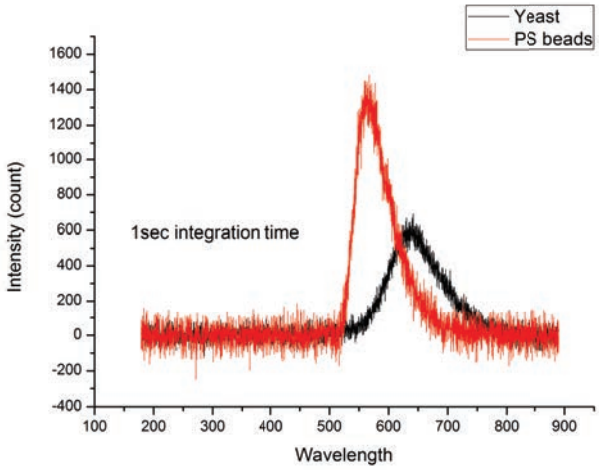

Figure 4.11: Fluorescent spectrum of PI stained yeast and fluorescent $6\mu m$ PS beads. $1s$ integration time.

yeast and fluorescent beads is measured at $10\mu L/min$, with no sheath flows, and the spectrum obtained. Figure 4.11 shows the superimposed results for a $1sec$ integration time (average over 10 measurements).
While both samples have slightly different fluorescence peaks ($565nm$ for beads and $640nm$ for yeast), the intensity is the more interesting factor. The fluorescent intensity from the PS beads is almost twice as big as the PI stained yeast (1310 counts against 585), even though the PI is designed for the $488nm$ laser light.

To further test the system with biological samples, a mixture is prepared of unstained yeast and fluorescent PS beads. The beads are chosen due their higher fluorescence signal. Both samples are measured individually before mixing. Figure 4.12 *(left)* show the superimposed results. Both plots are similar to those previously obtained for the respective samples. Even though

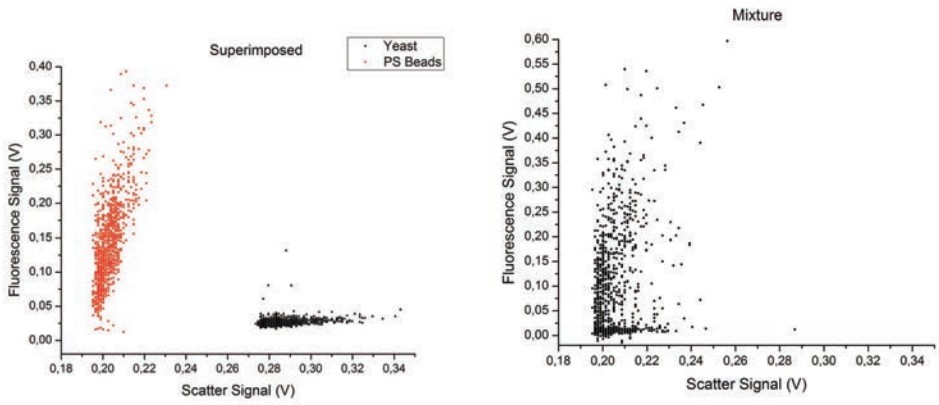

Figure 4.12: Superimposed scatter plots of unstained yeast cells and fluorescent PS beads *(left)*. Scan on mixture of the same two samples *(right)*.

the two samples are of comparable size, the yeast gives a higher scatter signal. Since the scatter measures a mixture of both FSC and SSC, it is possible that the granularity and big variation in density of the yeast cells is the cause of the bigger signals. As expected, the fluorescence is much higher for the PS beads. The overall count rate for both samples are also similar (around 30 per second), indicating a similar concentration. The two samples are now mixed and run through the setup. The resulting measurement is displayed in figure 4.12 *(right)*. When directly comparing the two plots, two distinct populations are still noticeable. While the fluorescent signals are virtually unchanged and helps identify the PS beads, the low-fluorescence signals from the yeast cells have also been reduced in scatter, with values comparable to the PS beads. This effect will be discussed later in the next section.

4.3.2 Listeria Bacteria

Moving towards more realistic samples, bacteria of the listeria family is now investigated. The *Listeria Monocytogenes* genus is a major human pathogen and source for a high percentage of yearly human food poisoning cases [54]. It is usually the causative agent of the bacterial disease, *listeriosis*, a serious infection caused by eating food contaminated with the bacteria. Its wide range of temperature tolerance is the main cause of its danger and extra care in food processing and storage is needed to prevent infection.
This species is however very dangerous to work with and requires special laboratories and expert personnel for handling. As a substitute, the genus *L. innocua* is used instead. This species is non-pathogenic but have similar physical properties (size, granularity etc). Typical size of the listeria bacteria is $0.4\mu m$ by $1 - 1.5\mu m$ (rod-shaped).
To prepare the samples, the bacteria are first incubated for $20hours$ in *BHI-medium* at 37° and then dispensed in a 1 : 200 working solution in an appropriate buffer (0.9% $NaCl$). These steps are done by *Jan Lenke*, *FH-Flensburg*, who has the appropriate experience and equipment. The bacteria are furthermore tested in a commercial FCM (*FC 500, Beckman Coulter GmbH*) to test viability and that staining protocols are working correct. All experiments are done using PBS buffer (phosphate buffered saline) for sheath flows.

Measurements are first conducted on pure unstained listeria, see figure 4.13 *(left)*. These results are quite similar to the results obtained on unstained yeast cells (see figure 4.9). Figure 4.13 *(right)* shows the results of a FC

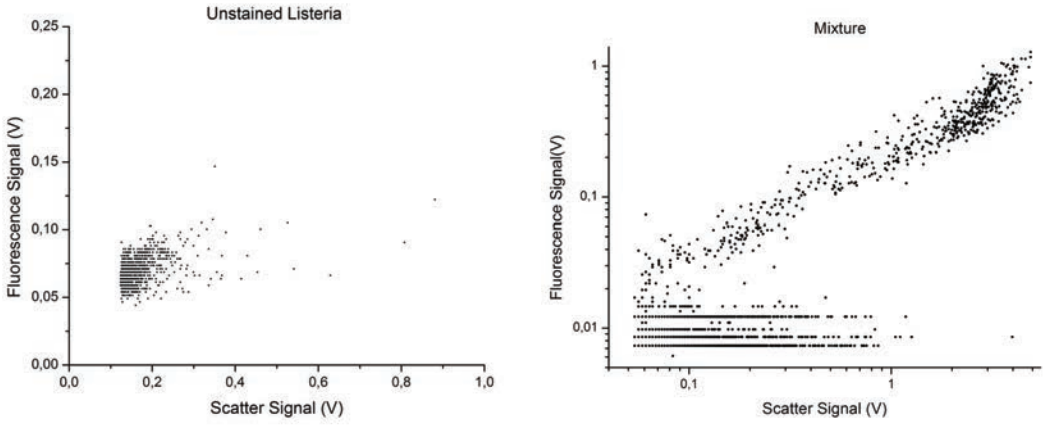

Figure 4.13: Scatter plot from unstained listeria bacteria *(left)* and mix of listeria and $6\mu m$ fluorescent PS beads *(right)*.

measurement on a mixture of unstained listeria and the $6\mu m$ fluorescent PS beads. This plotted data confirms that the listeria are still distinguishable in a mixture.
A sample of listeria is now stained with PI and investigated. As PI is a DNA stain, these bacteria have been autoclaved at $121°C$ for $20min$ to ensure lysis [17]. To stain the sample, $0.5ml$ bacteria working solution is mixed with a PI solution ($2.5\mu l$ pure PI in 10% DMSO). The result of the scan is plotted in figure 4.14 *(left)*. The plot shows a large and clear fluorescent signal (some

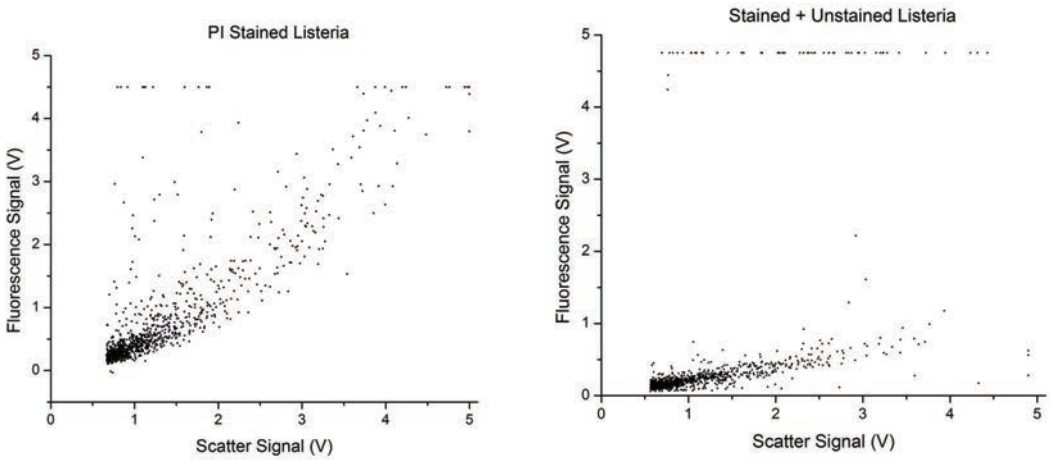

Figure 4.14: Scatter plot showing PI stained listeria *(left)* and mix of unstained and PI stained listeria *(right)*.

events even saturate the PMT channel), while the scatter signal is somewhat more spread out compared to the unstained sample. Lysed samples can, however, contain quite a large amount of partial cells, debris and other micro-structures that can lead to a bigger spread in scatter signal [17].
Finally, a sample containing both stained (lysed) and unstained (viable) bacteria is prepared by mixing the two previously prepared samples. The resulting plot is shown in figure 4.14 *(right)*. The results are quite similar to the sample containing purely stained listeria. While the scatter signals are almost identical (as the spread from the lysed cells carry over into the mixture), there is a reduction in the fluorescence signal. These low values makes it very hard to distinguish a population of unstained bacteria from the stained ones.
This signal overlap may be caused by a number of reasons. Firstly, PI stains, while easy to perform and handle, form fairly weak interactions with the sample (DNA and RNA sequences) [17]. Adding an additional volume of unstained bacteria alters the concentration of dye in the solution causing a

reduction in the amount of PI bound to the satined sample. The sample is essence diluted as the overall amount of PI is distributed in a larger volume. Furthermore, as the unstained sample can contain considerable amount of dead cells [17], the effect is enhanced as more PI binding sights are introduced. Figure 4.15 shows the signal from the fluorescent channel for the stained *(left)*, and mixed sample *(right)*. The data confirms the assumptions

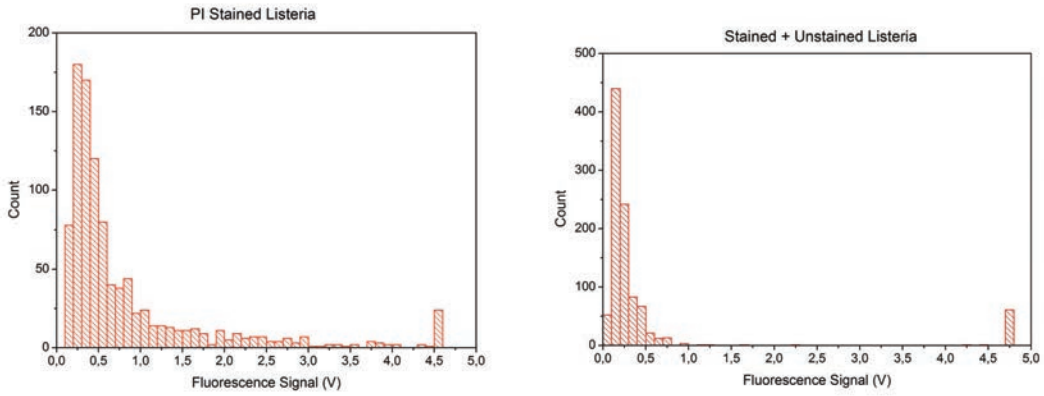

Figure 4.15: Histograms of fluorescent signals for unstained listeria *(left)* and PI stained listeria *(right)*.

as a significant reduction (at least 50%) of fluorescence is observed. This cross-staining and dilution of fluorescence would not normally be an issue in a commercial FCM where an entire sample is analyzed in under a minute [17]. In the microfluidic setup, however, a $1mL$ sample is delivered at a typical speed of $1 - 10\mu L/min$, giving most of the sample volume ample time to reduce the PI gradient and establish a new equilibrium.
Furthermore, it is believed that the fluorescence signals from the investigated sample is simply below the sensitivity of the system in its current state. While signals are indeed obtained on the PMT, this is done at quite high sensitivity. This is less of an issue when comparing unstained bacteria or cells to fluorescent PS beads (like figure 4.13 *(right)* or 4.11), where only low sensitivity is needed on the PMT. This is because the fluorescent PS beads have orders of magnitude higher fluorescence than stained samples [17].
The fluorescence sensitivity issue is also observed when considering measurements on the calibration beads (figure 4.7). While it is clear that the setup is indeed able to distinguish the two fluorescent intensity levels, they are not as high as the supplied values indicate they should be. The intensity from the *peak 2* beads are barely higher than zero, meaning that anything in the sample with a lower intensity will also be measured zero.

Lastly, the general large spread in signals can perhaps be attributed to the optical measurement volume. As calculated in section 3.3.4, the crossover between the laser light cone and focused flow is only 50% of the total sample volume. This can result in many partial scatter and fluorescence events where a bacteria only crosses part of the laser beam, thus creating a correspondingly lower signal.
The above mentioned issues are a fundamental limitations of the setup in its current state that requires further technological improvement of the FC microfluidic LOC setup. On the electronics side, the introduction of a logarithmic amplifier on the PMT output would ensure a much bigger dynamic signal range that will hopefully make it possible to detect both very low, and also high signals. As for improving flow focusing, recent advances in microfluidic chip design has enabled the production of 2D planer structures in which true 3D hydrodynamical focusing is possible [55]. If this design can be realized, a 100% overlap between focused flow and laser beam can be achieved, and no samples will be missed or partially measured. Lastly, on the optical side, even more work could be put into enhancing the amount of collected fluorescent light. An obvious avenue to re-visit is the in-plane lenses that in theory works, but requires refinement of the production steps.

4.4 Oil Droplets

This last section is concerned with using the FC setup in a slightly unconventional way. As mentioned in the introduction, oil droplets are used as model systems for protocells and a major goal of this project is to create a microfluidic platform able to generate and manipulate these droplets. Furthermore, the droplet system can be integrated into the microfluidic FCM setup and used to detect and investigate the droplets.
For this purpose, FCM is applied to preformed populations of oil droplets. Two distinct populations are created (the process is discussed in detail in the next chapter), one containing regular dye (*Sudan Black*), another containing a fluorescent dye (*Nile Red*). The droplets are formed by *Nitrobenzene* and stabilized in $40mM$ oleate at pH 11. The same continuous phase is used as sheath fluids and the droplets are dispersed in the flow cytometer chip at $5\mu L/min$, with a flow ratio of $r = 3$. Figure 4.16 *(left)* shows superimposed measurements of the two individual droplet populations. The fluorescent signal from the droplets stained with Nile Red is very intense and easily distinguishable from the non-fluorescence of the Sudan Black stained droplets. In most cases the Nile Red droplets saturate the PMT (signal at $5V$), even at low amplification. As for the scatter signals, two things are worth notic-

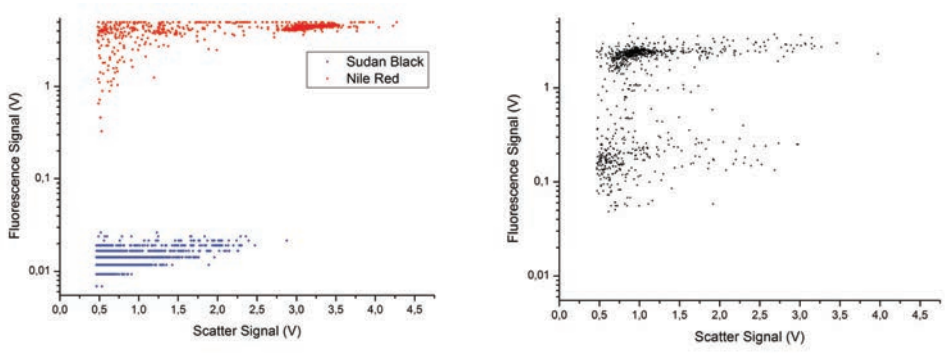

Figure 4.16: Superimposed scatter plots showing FC on preformed fluorescent (Nile Red) and non-fluorescent (Sudan Black) NB droplets *(left)* and plot showing the result of a mix of the two populations *(right)*.

ing. Firstly, both populations span a very wide range; in the case of the Nile Red droplets, almost the entire $0 - 5V$ output range. This indicates a wide spread in droplet sizes. Secondly, the non-fluorescent droplets clearly have less size-spread, and only span roughly half the entire range.
The two droplet populations are now mixed $1 : 1$ and run through the setup. The resulting plot is also shown in figure 4.16 *(right)*. Again, using the intensity of the fluorescent signal, the two populations are clearly distinguishable. Through the microscope mounted above the chip setup, video segments are obtained of the droplets passing by the optical fibers in the chip. Figure 4.17 shows frames containing no droplet, a non-fluorescent droplet (blue) and a fluorescent droplet (red), respectively. The images clearly show the difference in emitted and scattered light and support the FCM plots presented above.

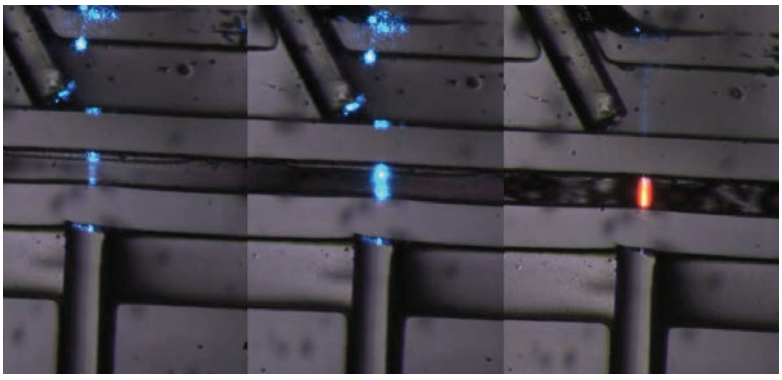

Figure 4.17: Microscope images of optical detection area, showing scatter (blue - *middle*), fluorescence (red - *right*) and no droplet *(left)*.

In conclusion, the results strongly indicate that the microfluidic FC setup

can also be used to track and measure oil droplets based protocells, which opens for interesting new experiments in the direction of microfluidic based protocell life cycles. The topic will be discussed further in the following chapter.

Chapter 5

Droplet based Protocells

In this chapter the work concerned with oil droplets used as protocell containers, is presented. Traditionally for these types of experiments, oil droplets are generated manually or by bulk methods. A goal in this project is therefore to develop a microfluidic platform, capable of creating large populations of mono-dispersed droplets, with desired composition and controllable sizes. On-chip droplet generation methods will be discussed in the first section.
An important step in the protocell life-cycle is droplet splitting. Methods for inducing oil droplet splitting will be presented in the second section along with a theoretical framework regarding the driving mechanisms behind the process.
Feeding resources to maintain a metabolism or inducing changes inside the droplet based protocell, is another important aspect. In the third section, droplet fusion is investigated as a method for delivering the content of one droplet to another.
Based on external input (such as the droplet FC presented in the previous chapter) differentiation of droplets is another interesting aspect of the protocell behavior. By using these inputs, it is possible to actively decide if a certain droplet fulfills a set criteria (size, charge etc.). Based on this, sorting of droplets can take place. This can be done either automatically or actively. In the last section, an active sorting scheme is presented and tested.

5.1 Droplet Formation

When two immiscible liquids are mixed, a phase separation occurs. When oil (or any non-polar organic solvent) is added to an aqueous phase, an interface is formed between the phases. While water has a highly polarized molecular structure, most organic solvents consists of long chains of unpolarized

carbon molecules. For lipids, which contain polar head-group, in aqueous solution, the system will try to minimize surface energy, by rearranging itself to minimize direct interaction between polarized water molecules and the non-polarized carbon chains. This leads to formation of 3D spherical structures or droplets. Figure 5.1 shows the traditional formation of lipid molecules in aqueous solutions.

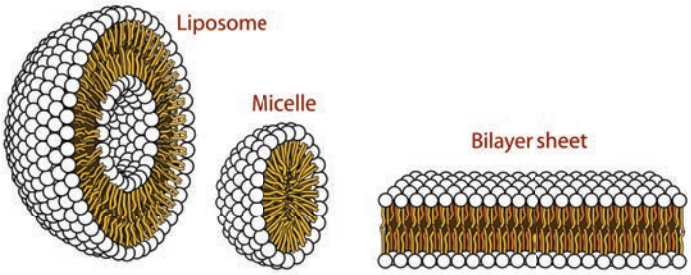

Figure 5.1: Typical lipids formations in aqueous environment, formed by self-assembly.

For all three structures, the head-groups arrange to protect the chains by facing them away from the water. Size and exact membrane composition depend greatly on the exact chemistry of the system. In a real system, such as a microfluidic one, the chemistry of the chip itself also plays an important role. If the chip material itself is hydrophobic (as in the case of PDMS), the organic phase will attract to the chip walls to minimize exposed surface to the aqueous phase (wet the walls). As discussed later in this section, this can be prevented by inducing surfactant molecules that acts to lower surface energy in the interface and consequently make droplets more stable.
In order to form droplets in a microfluidic system, external work is needed to overcome the laminar flows found at low Reynolds numbers. In the following section the basic physics defining the problem of droplet formation, will be investigated.

5.1.1 Formation Mechanisms

In a physical sense the main addition that droplets bring to single phase microfluidic system, come from the introduction of interfacial tension. Interfacial tension is an energy per unit area (J/m^2) that acts to minimize the total surface area to reduce the free energy of the interface. The minimum area for a given volume is a sphere, which is the shape taken by isolated droplets. Confined droplets on the other hand, must adapt their shape to

the presence of channel walls, while still curving their interface. The curvature introduces a pressure difference, known as the Laplace pressure. The pressure between the inside and the outside of a droplet can expressed by the Young-Laplace equation

$$\Delta p = \gamma \left(1/R_1 + 1/R_2\right) \tag{5.1}$$

where R_1 and R_2 are the two principal radii of curvature of the interface and γ is the surface tension. The pressure difference is determined locally at each position of the interface. Since R_1 and R_2 can vary in space, this can induce pressure variations within a droplet that is important for droplet formation [44].
When considering small Re systems (where inertia is negligible)m the main effects acting on an interface is viscosity μ and surface tension γ. The relative strength of these two parameters is given by the Capillary number $Ca = \mu V_0/\gamma$, where V_0 a characteristic velocity of the flows. A low value of Ca indicates that the stresses due to interfacial tension are strong compared to viscous stresses. Drops flowing under such a condition minimize their surface area by producing spherical ends. In the opposite situation of high Ca, viscous effects dominate and large deformations of droplets can be observed [44].

When designing microfluidic systems for droplet formation, these devices should be able to form regular and stable mono-disperse populations, but also need to be flexible enough to provide droplets of desired volume, at a controllable rate. To this end, three main approaches have emerged based on different physical mechanisms. These are best described by the flow topology in the vicinity of the droplet production zone [56]:

- (i) breakup in co-flowing streams (nozzle inside capillary)
- (ii) breakup in cross-flowing streams (T-junction)
- (iii) breakup in elongational strained flows (hydrodynamic flow focusing)

In all three cases, the phase to be dispersed is driven into a microchannel, where it encounters the immiscible carrier fluid that is driven independently. The junction where the two fluids meet must be designed to optimize the reproducibility of droplet formation. The geometry of the junction, together with the flow rates and the physical properties of the fluids (interfacial tension and viscosities) determine the local flow, which in turn deforms the interface and eventually leads to droplet pinch off if the conditions are right. The size

of the droplet is controlled by a competition between the external pressure (from side flows) and the resulting viscous shear stresses, on the one hand, and the capillary pressure (from surface tension) resisting deformation on the other. For this reason, the most important dimensionless number when trying to predict droplet formation behavior is Ca. Other important dimensionless numbers include

- Fluid flow ratio $r = Q_s/Q_i$
- Viscosity ratio $\beta = \mu_{in}/\mu_{out}$
- Geometry ratios, such as channel widths ($x = w_{in}/w_{out}$)

While the physics at the origin of droplet production in co-axial injectors (i) is easily identified as related to the Rayleigh-Plateau instability, the cylindrical geometry of the injector is a serious obstacle to its implementation in PDMS LOC devices [57]. In contrast, the two alternative geometries of (ii) and (iii) are well suited to planar geometries, but present more complex fluid dynamics.

Cross-Flowing Streams

Droplet formation in a T-shaped device was first reported by Thorsen *et al.* [58], who used pressure controlled flows in micro-channels to generate droplets of water in a variety of different oils.
In general, three flow regimes can be defined according to the T-junction channel geometry, specifically, the channel width ratio $x = w_i/w_o$ (see figure 5.2). When $x \ll 1$ droplets are emitted before the block the entire channel

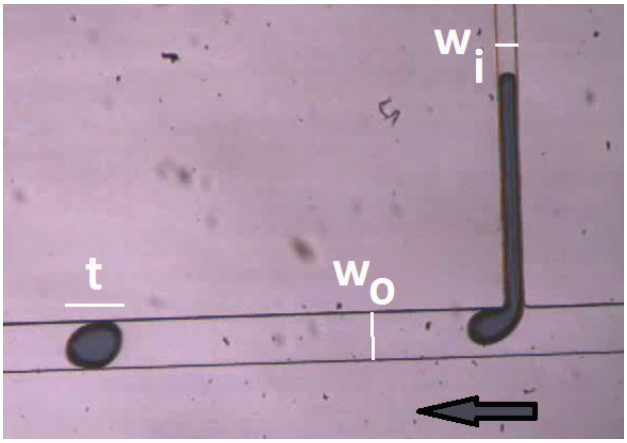

Figure 5.2: Microscope image showing droplet breakup in T-junction geometry.

and formation is purely due to shear stress (*dripping regime*). Droplets break off when the viscous shear stress overcomes the interfacial tension [59]. For $x \sim 1$ (the *squeezing regime*), the droplet obstructs the channel as it grows, restricting the flow of the continuous phase around it. This reduction in the gap through which the continuous phase can flow, leads to a dramatic increase in the dynamic pressure upstream of the droplet, thus forcing the interface to neck and pinch off into a droplet [59]. The squeezing regime further evolves into the formation of *stable parallel flowing streams* when the dispersed phase flow rate becomes larger than the continuous phase flow rate [60].
In the squeezing regime, the drop length t decreases linearly with the flow-rate ratio (faster cross-flow leads to smaller droplets) and droplet length is independent of the continuous phase viscosity [59]. On the other, hand in the intermediate regime ($x < 1$) the viscosity ratio β has been found to be very important for the droplet formation process, where both shear stress and confinement strongly influence the shape of the emerging droplet [59, 61, 62].
While simpler to implement in a 2D structure, the T-junction method has one major drawback specific for the PDMS microfluidic system. Contact between channel walls and dispersed phased is much larger due to the simpler design, which increases the wetting of the dispersed organic phase onto the hydrophobic PDMS walls. It is, however, ideal for the splitting of already stable droplets (discussed later), where the scaling laws can be directly applied.

Flow Focusing

A flow focusing design is preferable in PDMS chips since channel wall contact is minimized by the two symmetric side flows containing the continuous phase, which squeezes the dispersed phase into a narrow stream. Flow focusing geometries was first proposed by Anna *et al.* [63] and Dreyfus *et al.* [64] in 2003. A typical droplet formation design using flow focusing is shown in action in figure 5.3.
Even though several distinct droplet formation regimes can be determined [65], the large number of geometrical aspect ratios characterizing flow-focusing devices has prevented the determination of simple scaling laws to predict the droplet size, distribution and rate of formation as a function of any key parameters [66]. Indeed, three new lengths are introduced to the problem in addition to inlet channel sizes (w_{in} and w_{out}), which are, the width of the aperture D_a and its length L_a, as well as the expanded channel width w_{exp} (see figure 5.3).
The general principle can, however, be explained principally by a two-phase

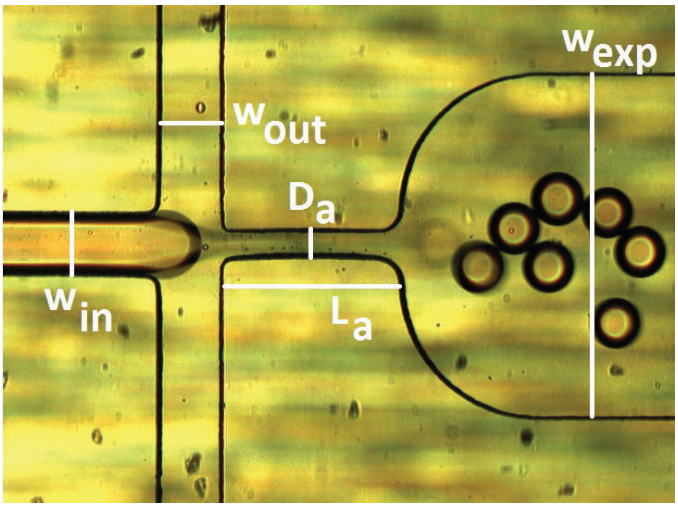

Figure 5.3: Microscope image showing droplet formation in flow focusing structure.

sequence. In the first phase *(squeezing)*, the dispersed phase is quasi-statically thinned down by hydrodynamic focusing. The duration of this phase can be related to the aspect ratio of the channel. As the squeezed thread becomes similar in size to the depth of the channel, it adopts a cylindrical shape and then rapidly becomes unstable due capillary instability (Rayleigh-Plateau). This is an effect of the dispersed liquid trying to minimize its surface area due to surface tension. This then eventually causes droplet breakup [67].
As already mentioned, there are no available clear-cut scaling laws for the transitions between various formation regimes, nor for the size and rate of production of droplets. Recent velocity field measurements suggest that the squeezing phenomenon is governed by the build up of a pressure difference, as the advancing finger partially blocks the outlet channel [68]. Other reports, however, state that squeezing/dripping droplet breakup depends solely on the upstream geometry and associated flow field, and not on the geometry of the channel downstream of the flow focusing orifice [69]. By contrast, the elongation and breakup of the fine thread during the thread formation mode of breakup depends solely on the geometry and flow field in the downstream channel.
In light of this recent research and despite the widespread use of flow-focusing devices, it is clear that the understanding of their detailed dynamics still warrants further research that is beyond the scope of this work.

5.1.2 Organic Compounds and Surfactants

Two different types of organic solutions are used in these experiments. *Mineral oil (MO)* is an organic compound consisting on light alkanes ($C_{15} - C_{40}$) and has a density of $800kg/m^3$ and is therefore slightly lighter than water [70]. *Nitrobenzene (NB)*, on the other hand has a density that is slightly higher than water ($1199kg/m^3$) and sinks in aqueous solutions [70]. NB has the chemical formula $C_6H_55NO_2$ and is a cyclic benzene with an amine group (see figure 5.4 *left*).

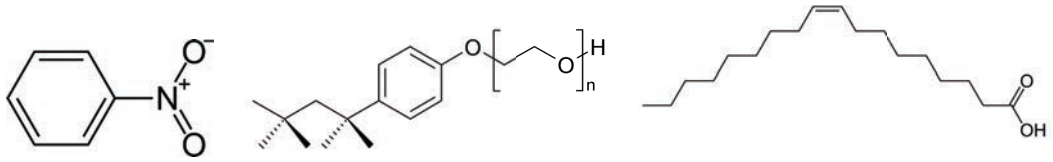

Figure 5.4: Chemical structure of Nitrobenzene *(left)*, Triton X-100 *(middle)* and Oleic acid *(right)*.

As mentioned earlier, creating droplets requires a lot of added energy to a system. This can for instance be added via mechanical work (macroscopic emulsions etc). An issue with this approach is that the created droplets might not be stable if the surface tension is too high. When this is the case, droplets will start to coalesce on contact (with both container or other droplets), to minimize their surface and, hence, energy.
To prevent this, surfactants can be introduced to the system. Surfactant molecules typically have a lipid-like structure, with a polarized head-group and a non-polarized tail. These molecules will attached themselves on oil-water interfaces and shield the droplet. By doing this, the overall surface energy is lowered and the droplets become more stable. The droplets may now be quite hard to destabilize again, as more energy might be required to overcome the local energy-minimum created.
Many different types of surfactants exist and they are generally categorized according to their chemical nature. *Triton X-100* ($C_{14}H_{22}O(C_2H_4O)_n$) (TX) is a nonionic surfactant and a common detergent in lab environments (see figure 5.4 *(middle)*). Its nonionic structure makes the molecules stable towards changes in the chemical environment (such as pH) [71].
Oleic acid (OA) is a naturally occurring mono-unsaturated fatty acid (see figure 5.4 *(right)*). It is soluble in an aqueous base to give soaps called oleates, which serve as surfactant molecules [70]. In contrast to TX, OA is a quite sensitive surfactant, as the carboxylic acid head-group needs to be deprotonated in order to interact properly with water molecules.

When using surfactants to stabilize organic compounds, the critical micelle concentration (CMC) is an important effects characteristic of a surfactant. Above the critical micelle concentration the surfactant saturates the solution and start forming micelles. Before reaching the CMC, the surface tension changes strongly with the concentration of the surfactant. After reaching the CMC, the surface tension remains relatively constant. The value of the CMC for a given dispersant in a given medium depends on temperature, pressure, pH, and (sometimes strongly) on the presence and concentration of other surface active substances and electrolytes [72].

Mineral Oil Droplets in Triton X-100

Using the described surfactants, oil droplet formation is now investigated in microfluidics devices. The most simple model system available consists of mineral oil dispersed in water. While it is possible to form droplets of mineral oil (see figure 5.5 *topleft*), the droplets are not stable enough and coalesce on contact with each other or the channel walls (see insert).
Triton X-100 is added to the system to stabilize the droplets. By adding 0.5% TX to the water-phase it is possible to form stable droplets (figure 5.5 *topright*). By adding 1% TX (figure 5.5 *bottomleft*), or even 5% TX (figure 5.5 *bottomright*) even more stable droplets are formed. An added advantage of adding 1%, or more, TX is that the droplet formation itself is more stable. At low concentrations, the oil-phase wets the PDMS channel walls easily. This enhances sticking of even more oil and thus creates laminar phase-seperated flows that are hard to break. At high concentrations of surfactants the channel walls themselves becomes coated and wetting is prevented.

NB Droplets in Oleate

Nitrobenzene (NB) and oleate forms a slightly more complex system, but the effect is very much the same as observed above for mineral oil and TX. The oleate molecules cover the non-polarized NB molecules and increases solubility in the water phase. By forming a charged layer around the NB droplets, the oil phase is repelled by itself and consequently prevents coalescence. A working surfactant concentration is determined by simple dish experiments. Figure 5.6 shows two NB droplets (volume $2\mu l$) created manually by pipetting into pure water. Less than $1s$ after adding the second droplet, fusion occurs, indicating that the droplets are not stable enough. Oleate is added until stable droplets are observed (no fusion after $15min$). Figure 5.7 shows NB droplets (both $5\mu l$ and $2\mu l$) in $20mM$ oleate where no fusion occurs.

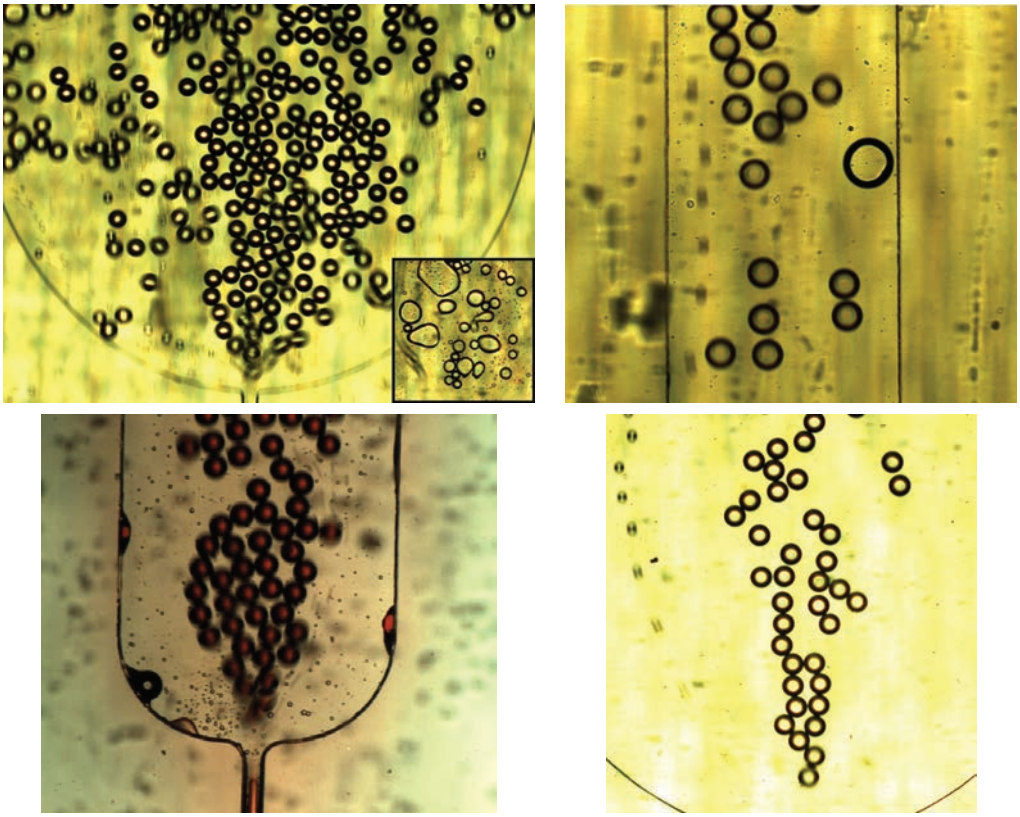

Figure 5.5: Microscope images show droplet formation of mineral oil in aqueous solution. No surfactant *(topleft)*, 0.5% Triton X-100 *(topright)*, 1% Triton X-100 *(bottomleft)* and 5% Triton X-100 *(bottomright)*.

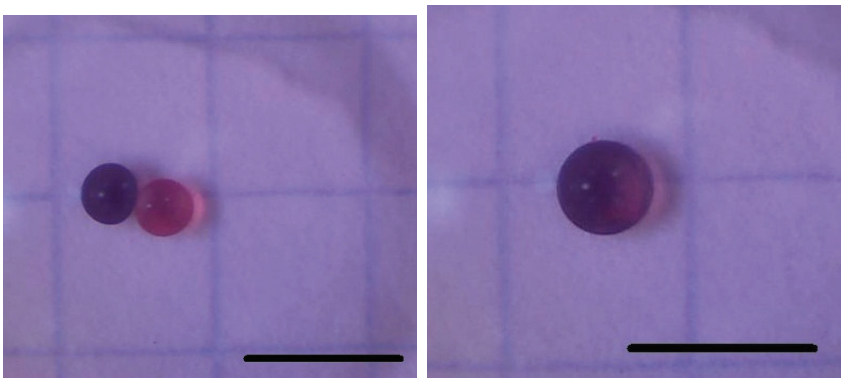

Figure 5.6: Video frames showing NB droplets in water ($2\mu L$), before *(left)* and after *(right)* spontaneous fusion. Scalebar $5mm$.

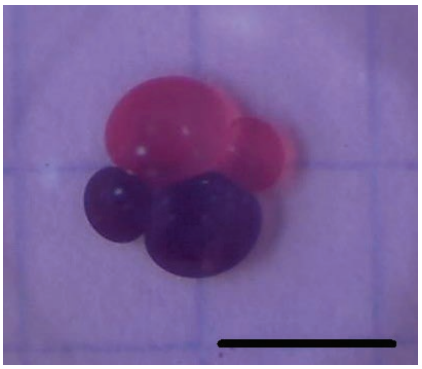

Figure 5.7: NB droplets ($5\mu L$ and $2\mu L$) in $20mM$ oleate after $10min$. Scalebar $5mm$.

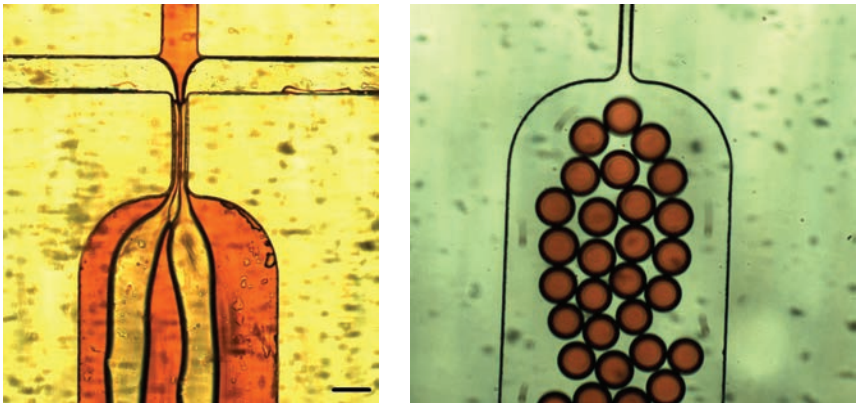

Figure 5.8: Microscope image showing NB droplet formation in $20mM$ *(left)* $40mM$ oleate *(right)*.

This system is, however more sensitive than the MO/TX system and when is is the tested in a microfluidic chip (see figure 5.8 *(left)*) droplet formation is not possible, due to wetting of the chip surface and walls. Increasing the oleate concentration to $40mM$, stable droplets is achieved (figure 5.8 *(right)*). As it is important to keep the oleic acid deprotonated, all solutions containing oleate surfactants are kept at $pH11 - 12$. This is achieved by adjusting with $NaOH$. From a protocell point-of-view, NB the more interesting system, for two main reasons. Firstly, the oleate system is sensitive to chemical changes and can be manipulated easier by external or internal means. Secondly, fatty acids can be metabolized as part of the protocell life cycle and therefore represent a more realistic model system.

From the above two droplet formation experiments it is clear that results from *in-vitro* experiments are not always directly translatable into microfluidics. This is mainly due to increased surface area (and hence surface interactions) as well as the fact that droplet structures are in a more stressed state due to the channel heights, which leads to increased surface area.

5.1.3 Automated Droplet Tracking

As droplet formation is performed on chip and in great numbers, it is desirable to have a system for automatic tracking and size measurement. This ensures good statistical significance and lessens manual measuring significantly.
For most experimental purposes, it is preferable to record video-segments of droplet formation and manipulation using the microscope setup and then do data treatment subsequently. When possible, video-segments are obtained using the maximum frame rate of the camera ($50FPS$), while still ensuring high enough exposure times. After recording, the video segments are cut, edited and compressed using *Virtual Dub*, which is also used to extract every frame of the segment.
Using *Vision Assistant 2011* (part of National Instruments' *LabView*) each frame is then analyzed according to a custom made image-treatment sequence. After adjusting color planes and setting intensity thresholds (which identifies droplets as dark objects), a built-in routine tracks and measures circular objects. Figure 5.9 shows a frame before *(left)* and after *(right)* the identification routine. Batch-processing can be set up for all frames of the video-segment and droplet sizes are saved to a data-file that can then be further processed.

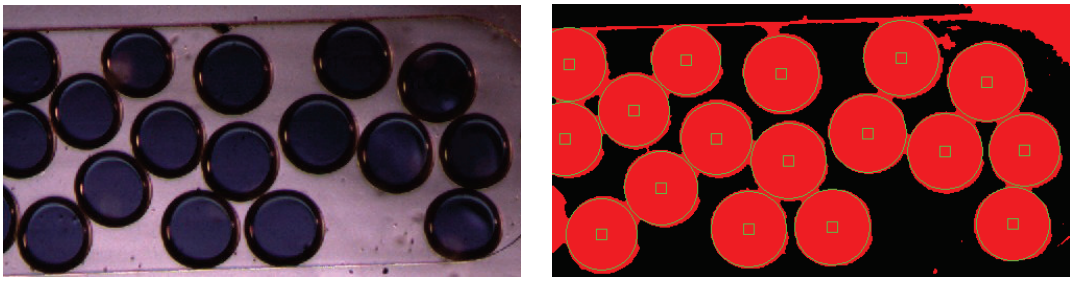

Figure 5.9: Video frame containing NB droplets, before *(left)* and after *(right)* being processed by the custom made LabView droplet tracking routine.

5.1.4 Flow Ratio and Volume Flow

While surfactant concentration and general chemical compatibility determines the stability of formed droplets, outer physical parameters determines size distribution and formation frequency. As discussed earlier, flow focusing is used to form droplets, and therefore the same parameters that control formation, as controls hydrodynamic focusing (discussed in section 3.3).
To investigate the influence of flow ratio r, NB droplets are generated using $40mM$ oleate as surfactant in a flow focusing junction. Video-segments are recorded for a wide range of volume flows and ratios and analyzed to get a droplet size distributions.
In three sets of measurements the NB flow is kept constant (at either 1, 3 or $5\mu L/min$) and the side flow speed is varied to obtain different flow ratios (from $r = 1$ to $r = 30$). Averaged droplet sizes are calculated based on obtained video-segments. The results are displayed in figure 5.10. The results

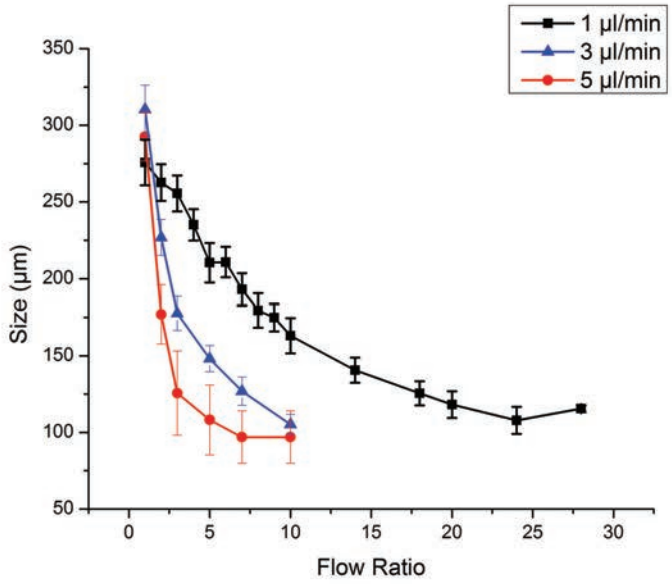

Figure 5.10: Plot showing droplet size as function of flow ratio r, for three different sample volume flows.

indicate that a certain flow ratio does not result in a certain droplet size, but is strongly dependent on the total volume flow.
Figure 5.11 shows selected frames for each of the three sample flow rates, for two different flow ratios ($r = 3$ and $r = 10$).
Clearly, by comparing the images and the error bars on figure 5.10 (standard

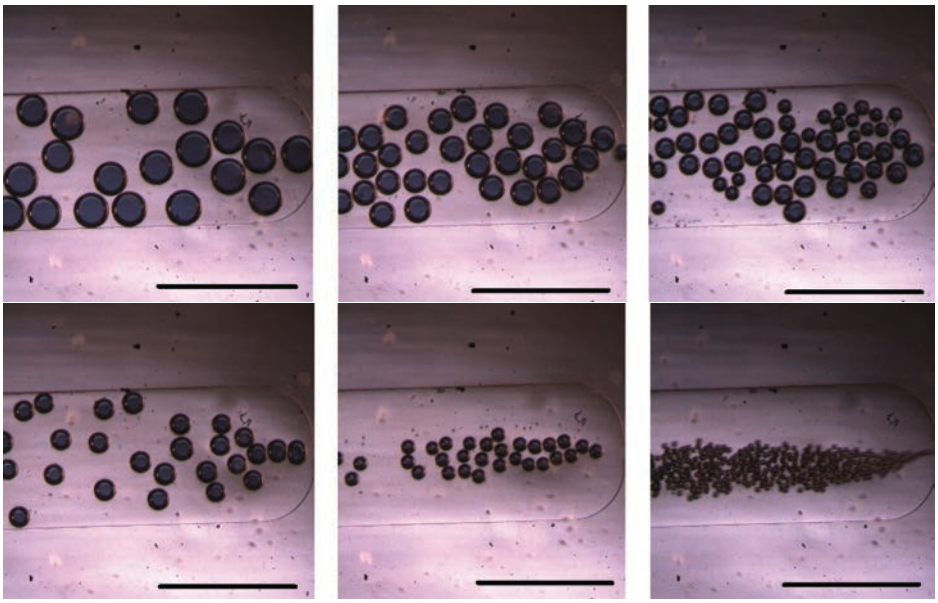

Figure 5.11: Microscope images showing NB droplets formed under different flow ratios (*top* $r = 3$; *bottom* $r = 10$) and oil (NB) flows $1\mu m/min$ *(left)*, $3\mu m/min$ *(middle)* $5\mu m/min$ *(right)*. Scalebar $600\mu m$.

deviation), the droplets become less mono-disperse for higher total volume flows. As the total flow speed increase and the liquids move faster and faster, the system has less time to revert to a quasi-stable state before new droplets are formed and therefore more variation is induced.
In order to investigate the influence of total volume flow, seven experiments are conducted with varying total volume flow, but a constant ratio of $r = 1$. The size distribution results of the measurements are plotted in figure 5.12 *(left)*. Sizes are measured manually using *ImageJ, NIH*.
The same experiment is done for a large number of droplets using the video droplet tracking routine and the size distributions are plotted in figure 5.12 *(right)* for three different total volume flows. For comparison around 30 droplets are measured manually, while over 20000 are tracked and measured from a $30s$ video fragment. Figure 5.13 show the measured mean droplet size for each flow ratio. Two things are worth noticing from these results. Firstly, as the results in figure 5.10 also show, not only flow ratio but also the total volume influences droplet size, although concrete scaling laws are hard to determine based on the data. Furthermore, the results suggest that the automated tracking method, while fairly consistent with manually measured results, does have a tendency to measure droplets slightly smaller.

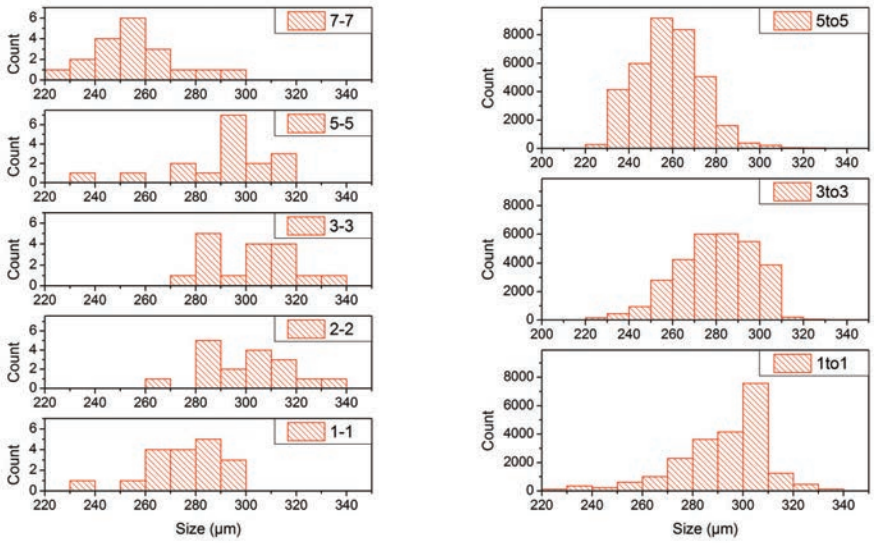

Figure 5.12: Histograms showing size distributions for various total volume flows (with $r = 1$). Measured manually *(left)* and measured from video frames using automatic LabView tracking routine *(right)*.

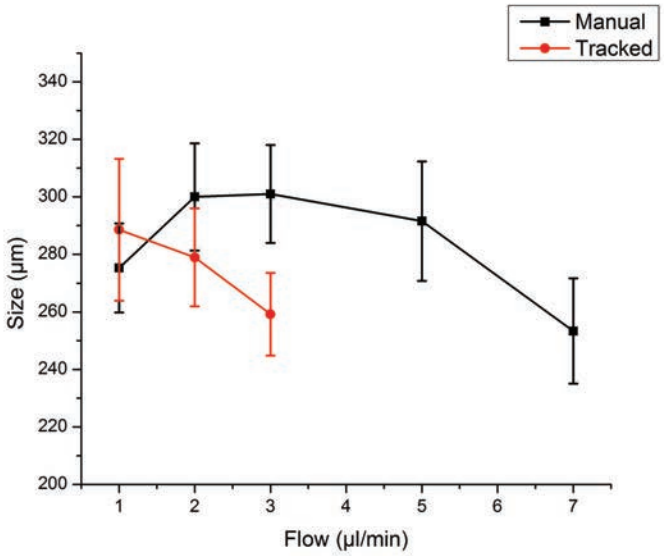

Figure 5.13: Plot showing the droplet size dependency of total volume flow for $r = 1$, measured manually and by video tracking. Errorbars indicate standard deviation.

5.1.5 Droplet Stability and Harvesting

Long time stability of the droplet formation process is investigated with a simple experiment. Using the same setup as above, the flow rates are set to $5\mu l/min$ for both the dispersed and continues phase. Using the camera on the setup, images are obtained every few minutes over a $40min$ period of time. These images are then analyzed and the droplet sizes are obtained. Figure 5.14 shows the average size for each frame obtained at a specific time. Each frame contains between 27 and 30 droplets. The plot shows stable droplet

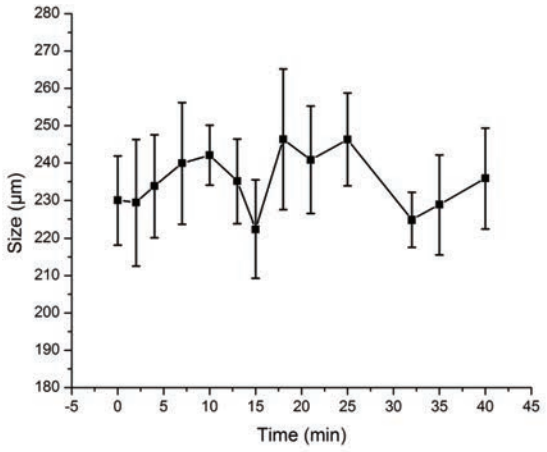

Figure 5.14: Plot showing droplet size measured over time (in the microfluidic chip).

sizes over time, with only minor variations. Error bars indicate standard deviation and these are within 7% for every measurement. The average droplet size is $235\mu m$ in diameter.
To test droplet harvesting, droplet samples are extracted every so often in the same experiment. This is done using a thin (I.D. $200\mu m$) FEP tube connected directly to the chip output. The droplets are collected in a petri-dish and images of the collected droplets are obtained. Figure 5.15 *(left)* shows an example of collected droplets. The hexagonal packing is an effect of the curved bottom of the dish and NB being heavier than water.
Droplet sizes are measured and plotted (see figure 5.15 *(right)*). Again, all standard deviations are within 7.5% and average size (over time) is $234\mu m$. The results correspond very well with those measured in the microfluidic chip and show that the droplets are very stable, even during and after harvesting. Even after a week or longer, the droplets are still stable.

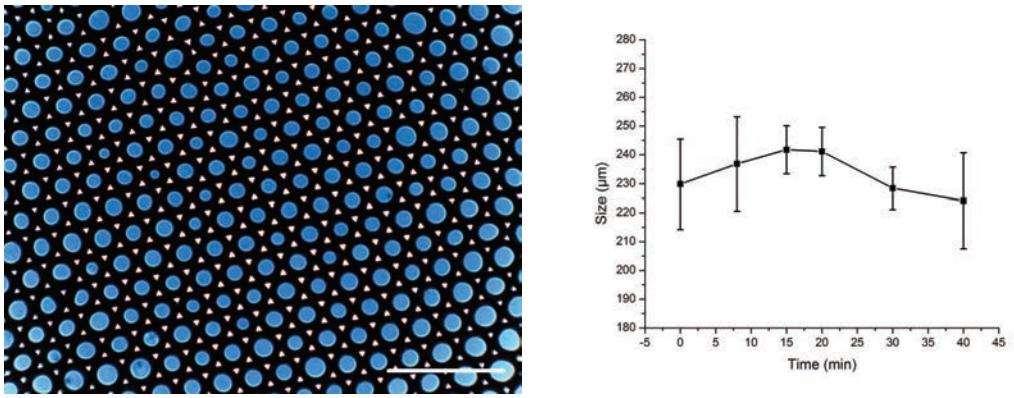

Figure 5.15: Microscope image showing harvested droplets collecting at the bottom of a petri-dish *(left)*. Scalebar $1mm$. Plot showing average droplet size over time *(right)*.

5.2 Droplet Splitting

Protocell splitting is an essential step in the protocell life cycle. In the complete and fully functional life cycle, the protocell will metabolize container molecules (fatty acids for surfactant) while obtaining oil molecules from the surrounding media. In the simple droplet based model system there is, however, no metabolic step and alternative methods for splitting must be investigated. As an alternative to metabolizing the surfactant molecules, these can be added directly to the system. Adding fatty acids to the system will lower droplet surface tension and under correct conditions induce splitting as the droplet glow. The exact mechanisms for this will be discussed later.
While this method is a purely chemical (and in effect thermodynamical) effect, more direct methods for splitting are also available [73]. One of these is demonstrated. Using the laminar flows in the microfluidic chip it is possible to shear droplets into smaller segments. This works essentially like droplet formation in a T-junction structure. If the droplets initially are stable and enough surfactant is available, the new smaller droplets will also remain stable. This method is also investigated later.

5.2.1 Droplet Thermodynamics

In this section a short thermodynamical treatment of oil droplet stability is presented. This is done by considering the Gibbs free energy of a closed system. The system consists of N oil molecules (with total volume V), which are split into n identical droplets. The oil is slightly denser than the aque-

ous phase and rests on the bottom of a dish. Each droplet is assumed to maintain a spherical shape with radius r and volume $v = V/n$. The energy of each droplet consists of a contribution from the surface tension ϵ_S that is proportional the surface area $a(n)$ with the surface tension γ, and a gravity contribution ϵ_G.
The total surface energy for all droplets can be expressed as

$$E_S(n) = \gamma \left(3V(4\pi)^{1/2}\right)^{2/3} n^{1/3} = \gamma C_2 n^{1/3}, \tag{5.2}$$

where C_2 is defined by droplet geometry. Using the gravitational force acting on the center of mass (found at height r) of a droplet, the total gravitational energy of all droplets can be written as

$$E_G(n) = \hat{\rho} V g \left(\frac{3V}{4\pi}\right)^{1/3} n^{-1/3} = C_4 n^{-1/3}, \tag{5.3}$$

where $\hat{\rho} = \rho_{oil} - \rho_{water}$ is the density difference between the oil and water phase.
Looking at the entropy of the system, this can be considered as consisting of an internal (S_i) and external part S_e. The internal part depends on how the molecules of each droplets arrange internally and is simply, so $S_i = ns_i$. This can be approximated to [74]

$$S_i(T, V, N) = k_B N(\ln\left(\frac{V}{N v_0(T)}\right) + 1), \tag{5.4}$$

where $v_0(T)$ is the size of a oil molecule. Note that this contribution does not depend on the number of droplets n. The external entropy contribution S_e depends on how the droplets arrange in the dish and can be expressed as [74]

$$S_e(T, A, n) = k_B n(\ln\left(\frac{4A}{C_2}\right) - 1/3\ln(n)), \tag{5.5}$$

where A is the dish surface area.
Gibbs free energy for the system consisting of N oil molecules in n droplets can now be written as

$$\begin{aligned} G(T, V, A, N, p, n) &= \gamma C_2 n^{1/3} + C_4 n^{-1/3} && (5.6)\\ &- k_B T n(\ln\left(\frac{4A}{C_2}\right) - 1/3\ln(n)) && (5.7)\\ &- k_B T N\left(\ln\left(\frac{V}{N v_0(T)}\right) + 1\right) && (5.8)\\ &+ pV - wN, && (5.9) \end{aligned}$$

where w is the energy required to move an oil molecule into the water phase and p is the system pressure [74]. The external entropy contribution (equation 5.7) is negligible, since the number of droplets n is infinitesimally compared to the number of molecules N.
If the system now is changed by reducing the surface tension γ, the droplet equilibrium will be disturbed and the system will seek a new equilibrium by spontaneously splitting the droplets [74]. Any spontaneous process at constant pressure and temperature, tries to minimize Gibbs free energy, in this example with respect to n. Only the first two first terms (equation 5.6) of the the Gibbs free energy depends on n, so the rest can be ignored in this context. When these two terms are equal, G at minimum. The number of oil droplets in thermal equilibrium after the system change ($n*$) can therefore be approximated by [74]

$$n* = \left(\frac{C_4}{\gamma C_2}\right)^{3/2}. \tag{5.10}$$

Note that $n*$ has to be rounded to the nearest integer for the equation to make sense.
Using equation 5.10, it is now possible to estimate in what range of γ a droplet of certain size (giving C_2 and C_4) will split, or what size of droplets will split for a given value of γ. In either case, $n*$ is set to 1.5, which rounds to 2. This is the minimum number one droplet can split into. Figure 5.16 *(left)* shows a plot of $n*$ as a function of droplet size for NB in water ($\hat{\rho} = 200kg/m^3$) containing $40mM$ oleate. The surface tension of this system has been measured (with a tensiometer, *PAT-1 Profile Analysis, SINTERFACE*) to $\gamma = 2.9mN/m$. These results indicate that chemical splitting is only possible for droplets larger than $5mm$ (in diameter). On the other hand, by setting $n* = 1.5$ it is possible to calculate the surface tension required to split droplets of a certain size. The results of this are plotted in figure 5.16 *(right)*, for sizes from $10\mu m$ to $500\mu m$ (in diameter), which are realistic sizes for droplets created in the microfluidic device. As the plot shows, a surface tension between $0.01mN/m$ and $0.12mN/m$ is required to split these small droplets. Comparing this with the current value of the system $2.9mN/m$ (which is already quite low) it is obvious that other methods are necessary in order to split droplets in this size-range, as the surface tension can not realistically be reduced by a factor of 30 or more.

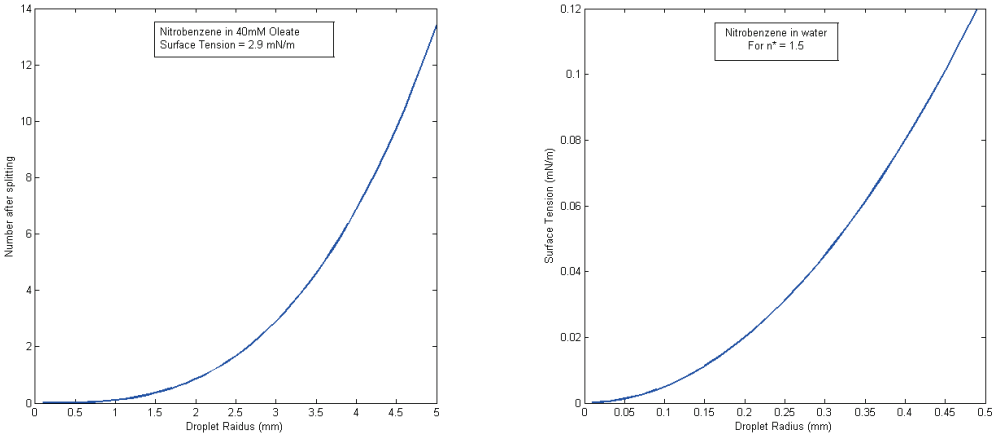

Figure 5.16: Predicted spontaneous droplet splitting ratio for various droplets sizes at $\gamma = 2.9mN/m$ *(left)* and required surface tension γ to split small ($10\mu m$ to $500\mu m$) droplets *(right)*.

5.2.2 Spontaneous Splitting

Even though the above system (NB in $40mM$ oleate) is too stable for spontaneous splitting, it is still possible in similar systems as demonstrated here. Using a slightly modified system, consisting of $20mM$ *CTAB* (*cetyltrimethylammonium bromide*) in NB, added to a $5mM$ oleate solution (at *pH* 12), splitting can be demonstrated. Figure 5.17 shows a $5\mu L$ droplet split into two droplets, while figure 5.18 shows a $10\mu L$ droplet split into at least five smaller droplets. For droplets smaller than $5\mu L$ no splitting occurs, only slight twitching and movement of the droplet. On the other hand for, droplets above $10\mu L$, splitting into multiple droplets occur. With respect to reaction time, the splitting process itself takes a comparable amount of time for different sizes, while the initial destabilization process takes longer for larger droplets.
During the splitting process, two things happen. The interfacial tension becomes very low transiently when the NB droplet is introduced and then slowly rises again as the system approaches equilibrium (destabilization). This alone is, however, not enough to split the droplet. The second component influential on splitting, is formation of fluid flow structures at the surface and inside the droplet. These flows are enough to distort and break the droplets apart [75].

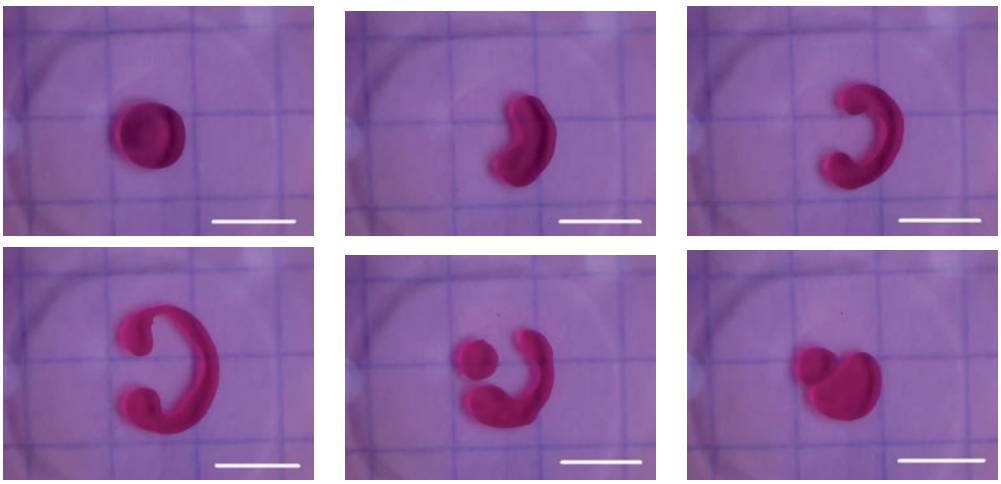

Figure 5.17: Selected video frames showing $5\mu L$ NB droplet added to $5mM$ oleate and subsequent splitting. After $40s$ splitting starts and after $20s$ the droplet is completely split. Scalebar $5mm$.

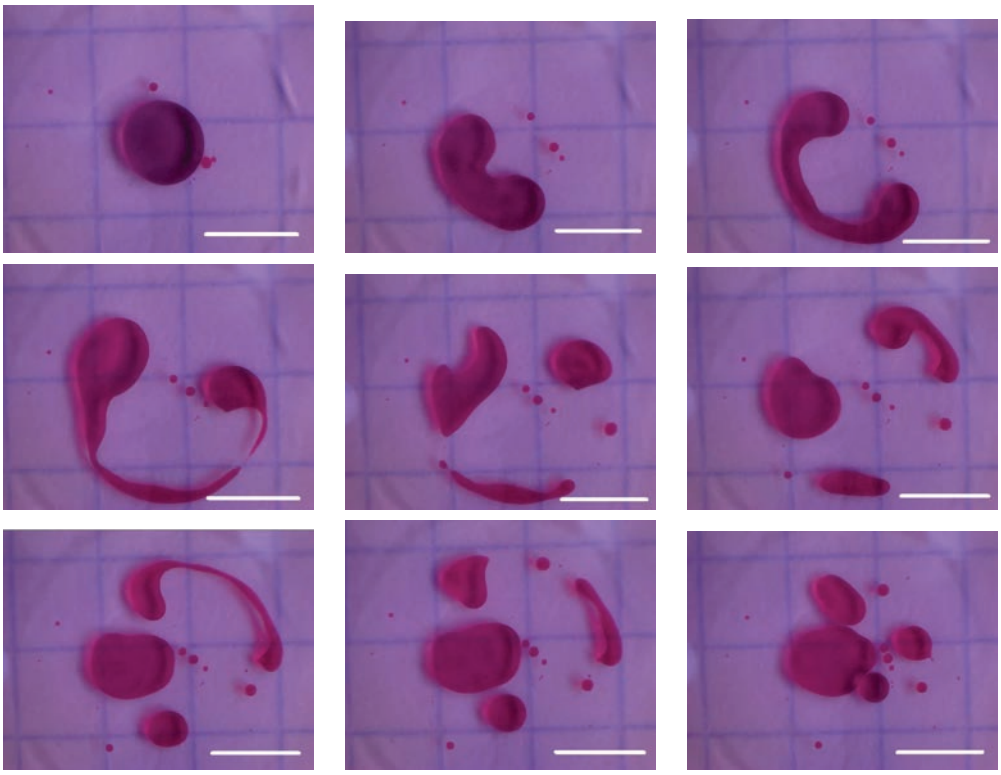

Figure 5.18: Selected video frames showing $10\mu L$ NB droplet added to $5mM$ oleate and subsequent splitting. After $75s$ splitting starts and after $25s$ the droplet is completely split. Scalebar $5mm$.

5.2.3 Splitting in T-Junction

As the thermodynamic calculations in section 5.2.1 indicate, the NB droplets formed earlier are too stable to spontaneously split. This is confirmed in section 5.2.2, where no spontaneous splitting occurs for droplets smaller than $5\mu L$ (even in systems with lower surface tension).
However, as discussed in section 5.1.1, a T-junction geometry can be used to break of droplets if channel dimensions are correct. This can be adapted to split larger droplets into smaller ones as the mechanism is the same [76]. In a region where the channel width ratio (x) is smaller than or close to 1 (the intermediate regime between *squeezing* and *dripping*), the droplet size is expected to decrease linearly with increasing cross-flow speeds.
Based on these considerations a microfluidic chip is designed (see figure 5.19 *left*), to facilitate droplet splitting.. The chip contains one droplet forma-

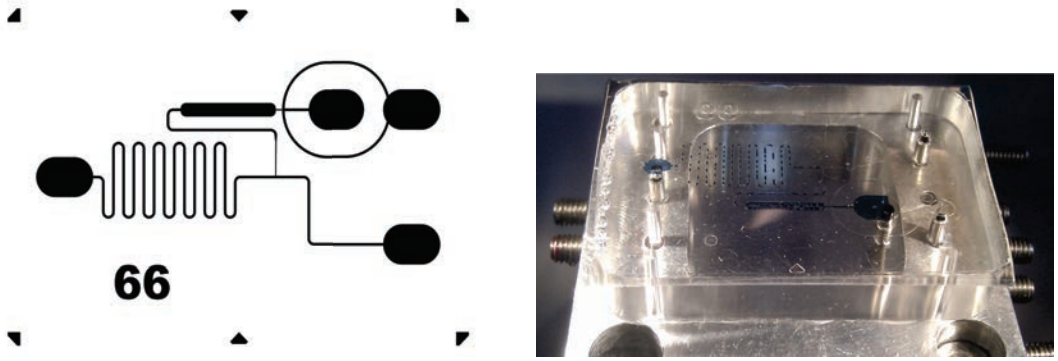

Figure 5.19: Chip design 66 used for splitting droplets in a T-junction *(left)* and picture of the system in operation *(right)*.

tion junction (flow focusing), followed by a channel that slowly narrows to a size of $100\mu m$. This channel forms a T-junction with a separate $200\mu m$ wide channel (resulting in $x = 0.5$). When a large droplet is elongated in the narrow channel it can then be broken into smaller droplets by the crossing (*chopper*) flow. Figure 5.19 *right* shows a picture of the chip in operation using NB (blue).
To investigate droplet splitting and the influence of chopper flow on resulting droplet size, video segments are obtained from both droplet formation junction, and the T-junction for different flow speeds and compared. These segments are analyzed to obtain size distributions before and after splitting. $40mM$ oleate solution is used for both flow focusing, and in the chopper flow to ensure that there is sufficient surfactant available to keep newly formed smaller droplets stable.

For a chopper flow speed of $10\mu l/min$, no real splitting is observed, as figure 5.20 *(left)* confirms.

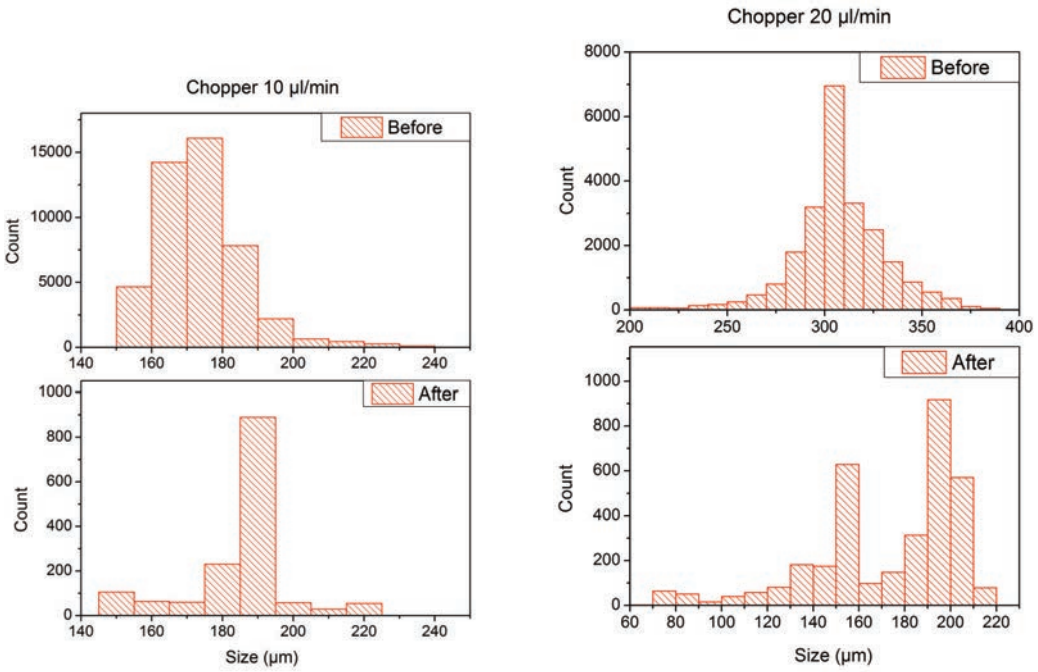

Figure 5.20: Histograms showing droplet size distribution before and after splitting, using chopper-flow of $10\mu L/min$ *(left)* and $20\mu L/min$ *(right)*.

For a chopper flow speed of $20\mu l/min$ there is a clear shift in the size distribution, see figure 5.20 *(right)*. For $30\mu l/min$, the shift is even bigger (see figure 5.21 *left*), while finally a maximum shift is obtained for $50\mu l/min$ (figure 5.21 *right*).
Figure 5.22 shows an example of droplet splitting in a video-segment (six consecutive frames). The video is recorded at $50FPS$ resulting in a time difference between each frame of around $20ms$.
Based on measured average size (diameter D) of the droplet, the average volume can also be calculated (droplets are assumed to be oblate spheroids, all $100\mu m$ high). By comparing this to the calculated volume of the split droplets, an average splitting ratio ($SR = V_{before}/V_{after}$) can be established for each chopper flow (V_c).

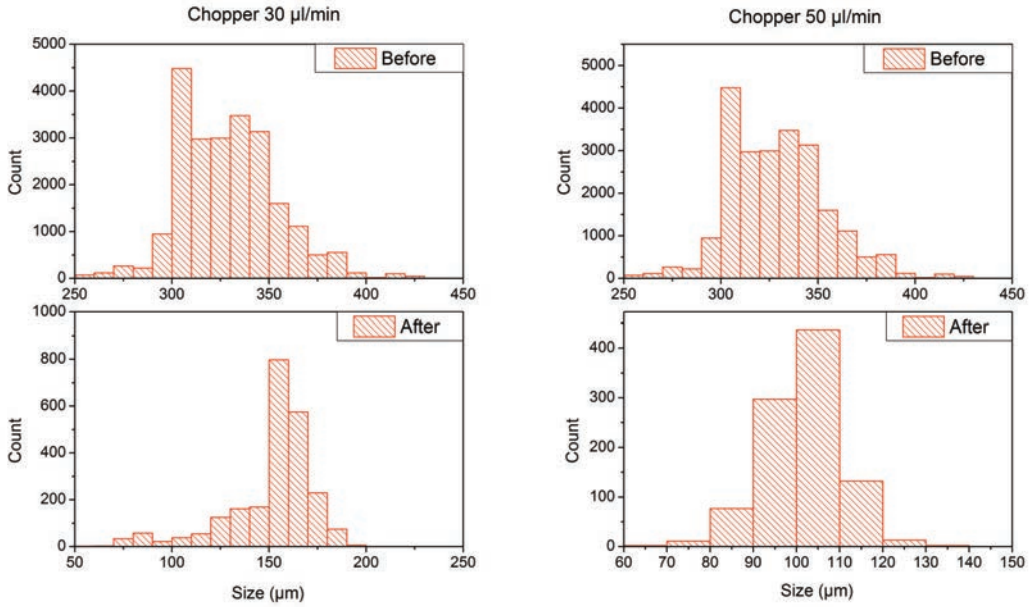

Figure 5.21: Histograms showing droplet size distribution before and after splitting, using chopper-flow of $30\mu L/min$ *(left)* and $50\mu L/min$ *(right)*.

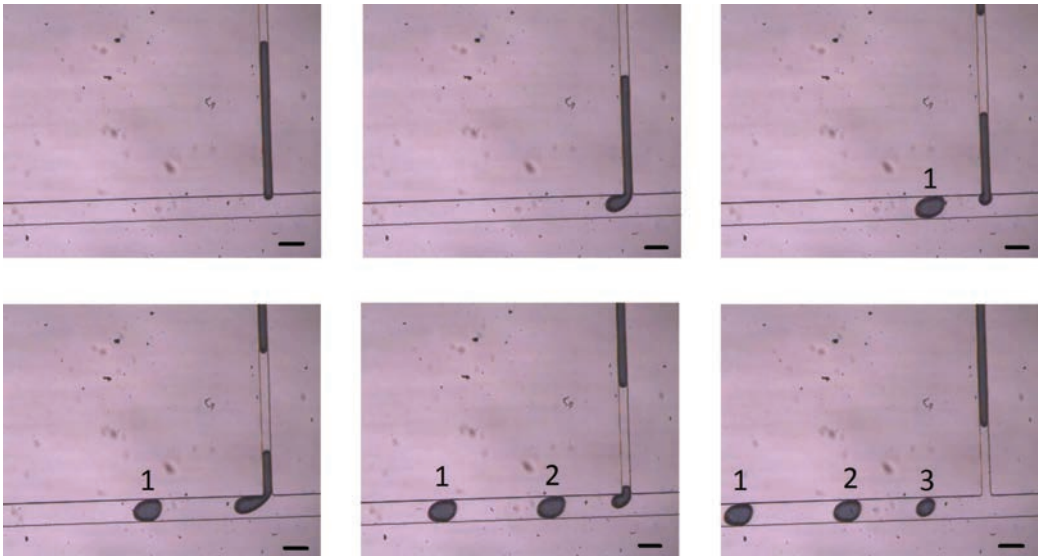

Figure 5.22: Selected video frames illustrating droplet splitting in T-junction. Chopper flow $20\mu L/min$. Scalebar $200\mu m$.

V_c $(\mu l/min)$	D_{before} (μm)	V_{before} (nL)	D_{after} (μm)	V_{after} (nL)	SR
20	294	4.525	172	1.549	2.92
30	299	4.681	152	1.209	3.87
50	299	4.681	103	0.556	8.42

Table 5.1: Average droplet size (and volume) before and after splitting. Splitting ratios (SR) calculated based on volume ratio.

The result clearly show that SR increases for increasing V_c up a value of over 8 for the fastest cross-flow. A this point the CCD can no longer obtain useful video-segments, but the trend is expected to continue for even higher values. Certainly, the method proves successful at splitting larger droplets, while creating stable smaller ones in the progress and therefore seem promising for further use in the protocell life cycle.

5.3 Droplet Fusion

In this section, droplet fusion is investigated as a method for delivering the content of one droplet to another. In protocell life cycle, this is an interesting approach to the issue of how to bring nutrients or resources to an already existing system. A wide range of methods are available for droplet fusion, including optical [77], electrical [78, 79, 80], thermal [81] or chemical methods [82].
A chemical method has been selected for use in this work as it can be utilized together with the properties of the droplet based protocell system. A system relying on the pH sensitivity of the surfactant molecules is proposed and demonstrated.

5.3.1 In-Vitro Fusion

As the droplet stability is dependent on the oleate surfactant being protonated, the most straightforward way to fuse droplets by chemical means is to reduce the pH, which will destabilize droplets enough for them to fuse on contact. Below, dish experiments performed on three different droplet sizes are presented. All droplets are created manually by adding the desired volume of NB to $150\mu L$ $40mM$ oleate at $pH12$ in a glass petri dish. $1M$ HCl is used as fusagen and is added in a small volume to change the pH. Video-segments are recorded as the droplets react and fuse.

$0.5\mu L$ droplets

These are the smallest possible droplets that can be created using a manual pipette. Four droplets are created (two red and two blue). These automatically collect at the bottom of the dish in an organized pattern. Even though in close contact, the droplets does not fuse.
Figure 5.23 shows video frames from before (as the fusagen is added), and after for both $0.5\mu L$ (top) and $2\mu L$ (bottom) $1M$ HCl. For the low con-

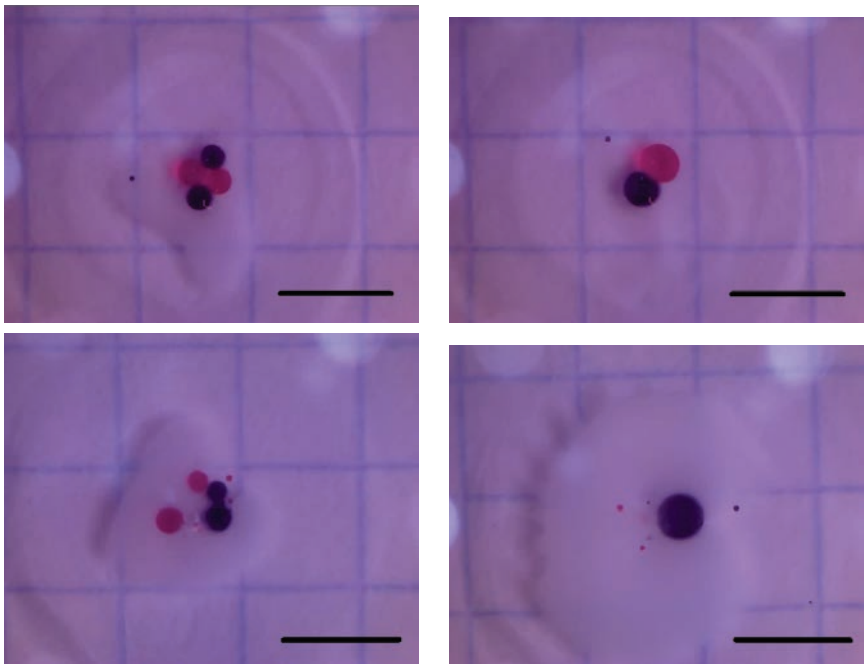

Figure 5.23: Video frames showing droplet fusion of four $0.5\mu L$ NB droplets by adding $0.5\mu l$ *(top)* or $2\mu l$ HCl *(bottom)*, before *(left)* and after *(right)*. Scalebar $5mm$.

centration ($0.5\mu L$) the droplets fuse slowly. Two droplets fuse after $30s$, the other two after another $40s$, while the two big ones do not fuse at all (even after $5min$. At higher added volume of fusagen ($2\mu L$), the four NB droplets fuse in less than $2s$.

$2\mu L$ droplets

Four $2\mu L$ droplets are prepared as in the previous section, and fusagen is added. Figure 5.24 show video frames from before and after addition of fusagen, for both $2\mu L$ (top) and $5\mu L$ (bottom). At $2\mu L$ added HCl, the

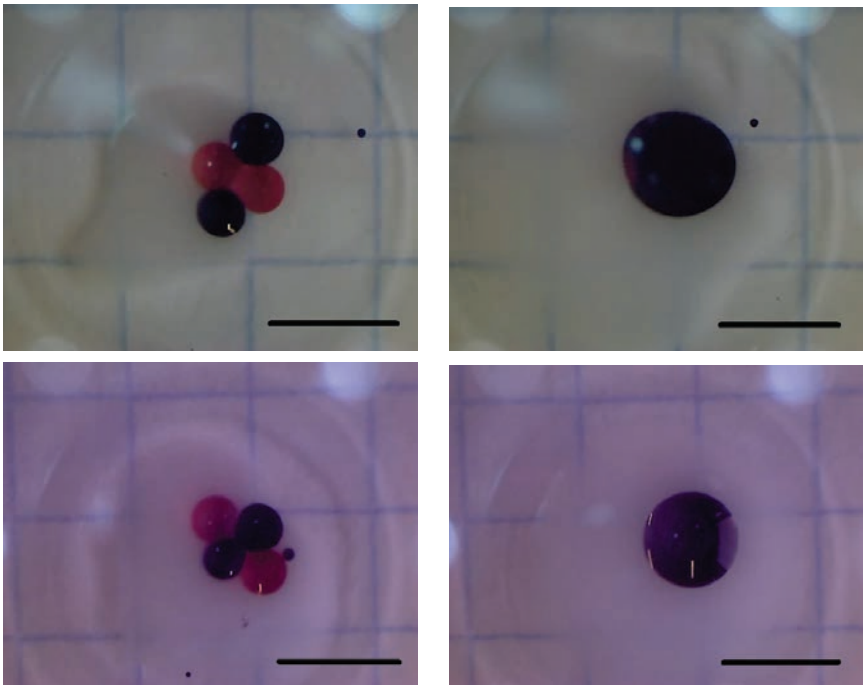

Figure 5.24: Video frames showing droplet fusion of four $2\mu L$ NB droplets by adding $2\mu l$ *(top)* or $5\mu l$ *HCl (bottom)*, before *(left)* and after *(right)*. Scalebar $5mm$.

droplets fuse fairly slowly, only starting after $17 - 24s$ (for two droplets), then another $10s$ before the two large formed droplets fuse. For $5\mu L$ added HCl, all four droplets fuse in less than $2s$.

$5\mu L$ droplets

Finally, four $5\mu L$ droplets are created in the dish and the fusagen added by hand. Figure 5.25 show video frames from before and after addition of the HCl, for both $2\mu L$ (top) and $5\mu L$ (bottom) added. At $2\mu L$ added fusagen,

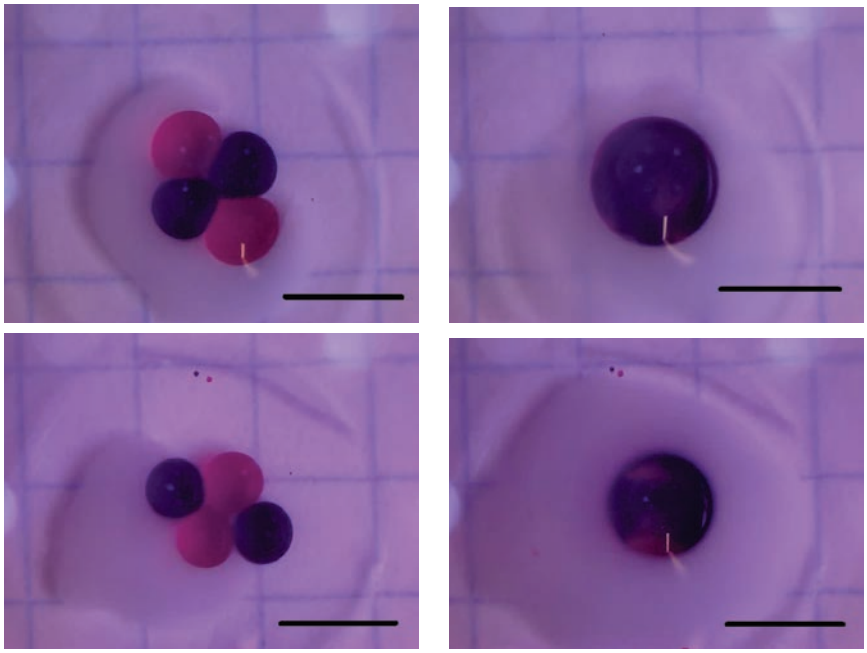

Figure 5.25: Video frames showing droplet fusion of four $5\mu L$ NB droplets by adding $2\mu l$ *(top)* or $5\mu l$ HCl *(bottom)*, before *(left)* and after *(right)*. Scalebar $5mm$.

the $5\mu L$ droplets fuse fairly slow, the process starting only after $35-42s$ (for two droplets pairwise). After another $7s$ the two larger droplets fuse together and finish the event. For $5\mu L$ added HCl all four droplets fuse in less than $2s$, but only after $30s$ with some twitching and movement of the droplets.

As noted in the three previous sections, the fusion speed varies, depending on the amount of added fusagen. In table 5.2, the droplet and added fusagen volume is listed along with the relative concentration (volume of HCl relative to total volume of NB). The observed fusion times are also shown for comparison. Comparing the relative concentration with the observed reaction times, there is a clear correlation between time and fusagen concentration. The more fusagen added the faster the reaction, as would be expected. This knowledge can be used to dose the fusagen to control fusion rates.

Droplet Vol. (μL)	Added HCl (μL)	Rel. Conc. (%)	Fusion Time (s)
0.5	0.5	25	70
0.5	2	100	2
2	2	25	40
2	5	62.5	2
5	2	10	50
5	5	25	30

Table 5.2: Table showing total volume of NB droplets and added fusagen, along with the relative fusagen concentration and fusion times.

The white milky liquid that forms when HCl is added to the dish (notable on some images) is light being scattered by colloidal emulsions in the the aqueous phase, formed by the oleate. When acid is added, the pH is lowered locally and the oleic acid is protonated. Since oleic acid is not soluble in water it will form microscopic oil droplets. As the acid spreads and the solution equalizes the pH rises slightly again and the emulsion dissolves once again.

Preformed Droplets

A $5\mu L$ solution containing pre-collected NB droplets is added to the dish to ensure the method works on droplets orders of magnitudes smaller. Figure 5.26 shows images from before and after $2\mu L$ HCl is added. The images

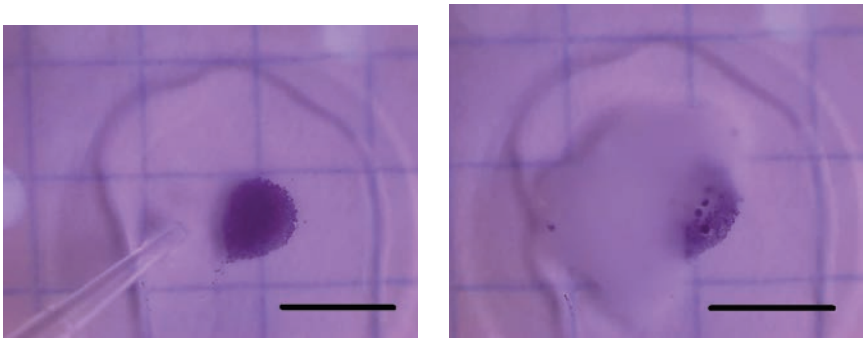

Figure 5.26: Selected video frames showing fusion of preformed NB droplets by adding $2\mu L$ $1M$ HCl, before *(left)* and after *(right)*. Scalebar $5mm$.

show that the system works and droplets do fuse, however, in a slightly slower fashion. Some droplets also destabilize and starts wetting the bottom of the dish. None the less, the principle works and will be explored further in the next few sections.

5.3.2 Droplet Separation

As the *in-vitro* results indicate, the change in pH is a very fast and effective way of fusing droplets together. However, since the method changes the surface tension of the entire system, care must be taken to ensure that mixing occurs under controlled conditions. It is necessary to organize droplets locally and keep them physically separated in order to prevent surfactant destabilization in the entire system. For this purpose, microfluidic devices prove a powerful tool. Many systems have been investigated, but the most effective way to separate oil droplets in a microfluidic environment is by using air bubbles as separators. While there is more elegant chemical solutions (such as ionic liquids), air has the advantage of being chemically inert (towards the used solutions), while also unmixable with both aqueous and organic liquids due to the difference in physical phases.
To test air bubble separation, two principle design ideas are investigated. Figure 5.27 shows four suggested designs, all relying on direct input of air (and in most cases, added inlets for fusagen). All four designs have two modified droplet formation structures (using one sheath inlet each to reduce number of inputs) as well as a meander structure. The purpose of this is to

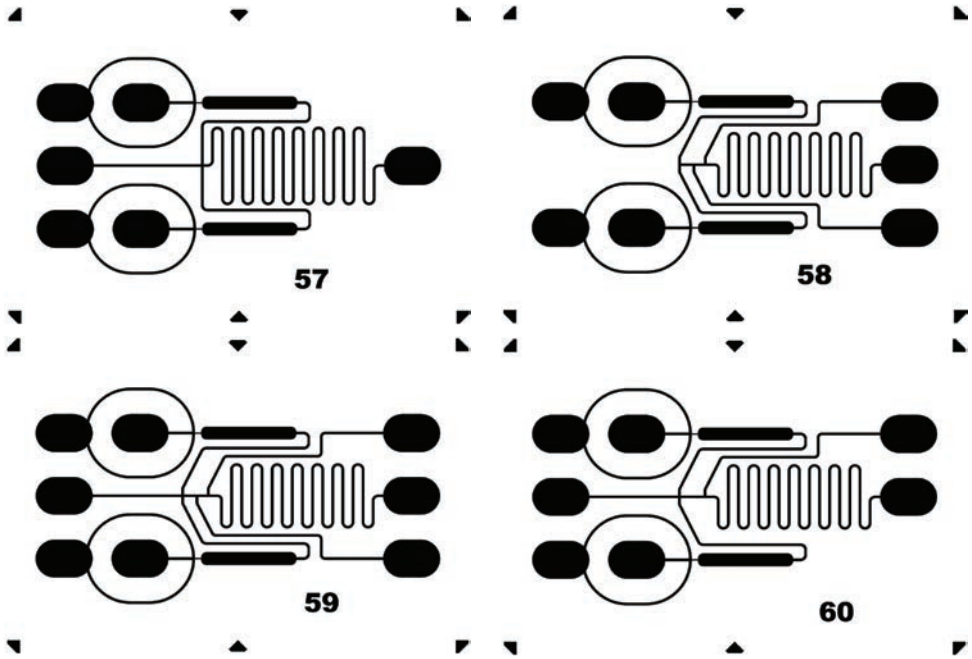

Figure 5.27: Chip design 57, 58, 59 and 60 used for droplet separation. The designs all contain two droplet makers and either one, two or three air/fusagen inlets.

increase the flow path and the time droplets spend in the chip. This is done to allow easier visual investigation and time for any chemical reactions to take place. All designs (apart from 57) have at least one T-junction inlet, while all but 58 feature a cross-shaped junction. The two independently controlled droplet makers allow for a wide range of different droplet populations that can vary in chemical composition and size. The two populations are brought together at opposite entries in the cross-junction where the remaining inlets also are located. Figure 5.28 shows an example of *design* 57 in use. Two NB

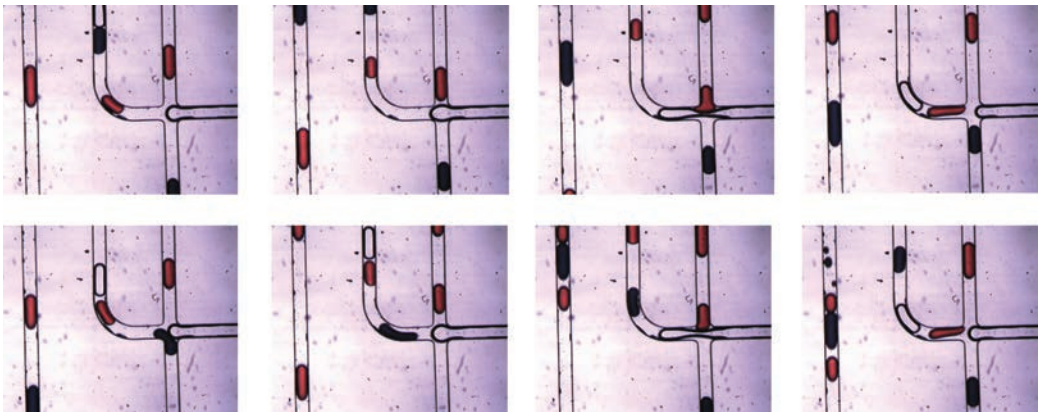

Figure 5.28: Eight consecutive video frames show separation of oil droplets (red and blue) using air bubbles. $20ms$ between each frame. All channels are $200\mu m$ wide.

droplet populations are formed (colored red and blue) and air is introduced. This is done by using an empty syringe that is otherwise controlled exactly like the other liquids. The eight images in figure 5.28 are successive frames from a video-segment obtained at the cross junction in chip *design* 57. The separation events consist of the following steps:

- Frame 1-2: Two droplets arrive at the junction, slightly out of sync.
- Frame 3-4: The red droplet interacts with the air stream *front* and pinches off a bubble.
- Frame 5: The blue droplet reaches the junction and squeezes past the air stream *front* that is slowly growing.
- Frame 6: The air front grows while new droplets approach.
- Frame 7-8: A new red droplet approaches and tears a new air bubble off.

The cycle is then repeated. The system works in similar ways for the other designs, where additional channels allow for introduction of the fusagen.
For both droplet and bubble formation, there is a certain latency between events. In this period, the stream snaps back and requires some time to reestablish the flow that reaches into the constriction. This latency time will depend on the overall flow rates of the system. As seen in the video-segment frames this affects air bubble formation. Once a bubble is detached some hundred milliseconds pass before the pressure has built up enough to extend the volume and create a new bubble. This phenomena is the main disadvantage of this type of system, as very precise synchronization between droplets (and therefore bubble break-off) is required. Figure 5.29 illustrates what occurs when droplets are out of sync with the air stream. In this case, the air

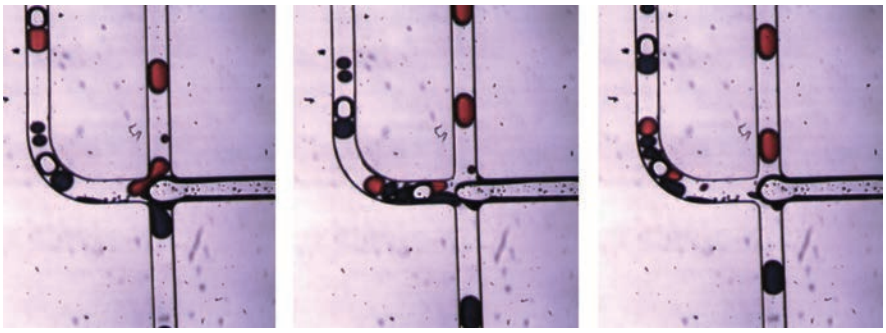

Figure 5.29: Three consecutive video frames showing air bubbles splitting NB droplets (red and blue) due to lack of synchronization. All channels are $200\mu m$ wide.

stream is not stretched enough for the droplet to shear it, so the droplet itself is instead sheared into smaller droplets. This happens for both droplets and the two droplets are split into five instead.
A general issue with the increasing amount of inlets in these structures is that the complexity of the flows also increase. This means that changes in one flow influences all flows and can easily interrupt flow focusing or similar. By being careful with major adjustments of flow rates and waiting some time for the system to equilibrate, most of these effects can be avoided.
To minimize some of these synchronization issues, a different chip layout is designed based on results reported by Whitesides *et al.* [83]. The general design is shown in figure 5.30. This layout has three flow focusing junctions positioned directly next to each other and is designed to utilized the local pressure differences that occurs during droplet formation. These pressure fluctuations are a result of the Laplace pressures caused over the oil-water interface. Effectively, this means that while one droplet is being formed,

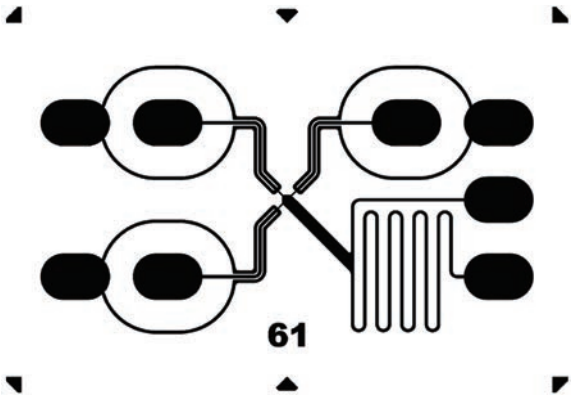

Figure 5.30: Chip design 61 containing three droplet makers. Based on [83].

the increased pressure temporarily blocks the remaining droplet makers. By using this design, droplets (and air bubbles) are automatically synced with each other, as droplet formation follows a certain pattern under stable conditions. The design also has a meander structure for visual inspection and an additional inlet for fusagen.
Figure 5.31 illustrates the self-synchronization principle in two different flow conditions. In contrast to *design* $57 - 60$, this design also uses a focusing

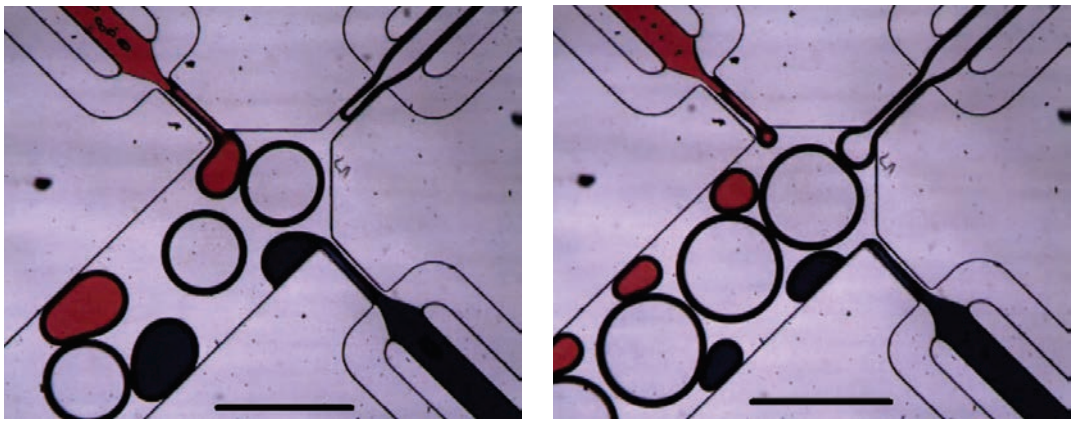

Figure 5.31: Microscope images showing complex foams of air and NB droplets (red and blue) created in chip design 61. Scalebars $800\mu m$

structure on the air inlet, which allows for better control of formation and removes the dependence on the oil droplets shearing the air stream into bubbles. The main downside of this design is the additional inlets that require more syringe drivers to control individually. This can, however, be partially resolved by using y-splitters on inlet tubes and share flows between inlets.

5.3.3 Fusion with HCl

A system for chemically induced *in-vitro* droplet fusion has now been established, along with a method for separating droplets using air bubbles. By reducing the pH of the system, by adding of a small amount of acid ($1M$ HCl), droplets are easily destabilized and fused. Initial experiments are conducted on a chip with design 60. Even though design 61 proves more promising with regard to regular droplet separation, the chip infrastructure demands too many individually controlled syringe drivers. *Design* 60 is therefore chosen as a compromise.
When introducing acid directly into the system (through the T-junction) the chemical system proves to be too effective. The droplets are completely destabilized and start wetting the chip channel walls (see figure 5.32). Additional

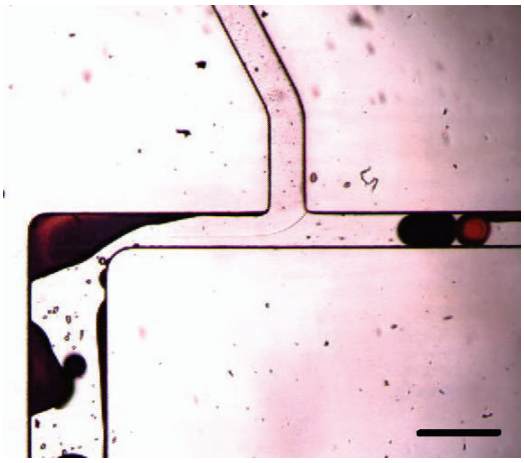

Figure 5.32: Microscope image showing droplet fusion using HCl. The fusagen is added from the top channel, while droplet pairs enter from right. Fusion is very fast and the NB wets the PDMS walls forming a continuous phase. Scalebar $400\mu m$.

drops are also destabilized and everything fuses into a continuous flow that runs along the channel wall into the output.
To reduce the amount of added acid, a new design is adapted (see figure 5.33 *(right)*). In this design air droplets are still introduced along with the droplets in the cross-junction, but the acid is now introduced further along the channel, halfway through the meander. The acid inlet has an additional T-junction that also introduces air. These air bubbles serves to create separated doses of acid, along with additional air bubbles to help keep droplets separated. Figure 5.33 *(left)* shows a droplet pair moving toward the acid inlet (left channel) and another fused pair leaving. The droplets are clearly

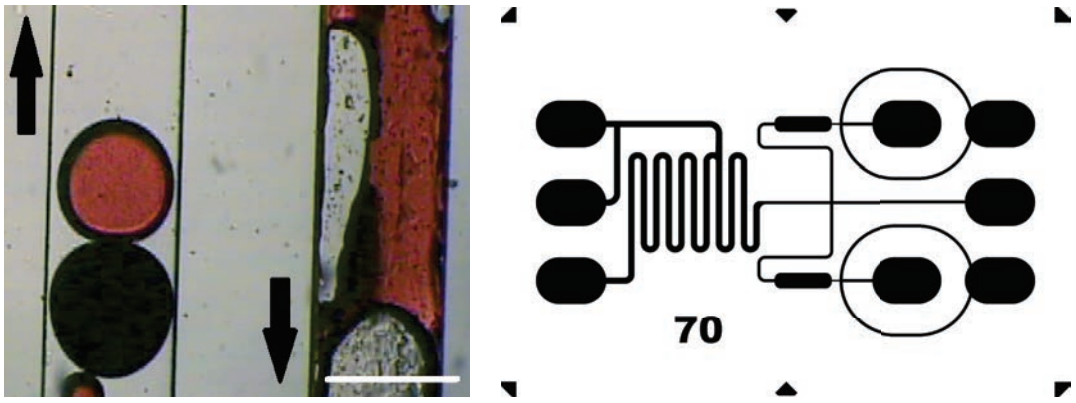

Figure 5.33: Chip design 70 *(right)* and NB droplet fusion in the channels *(left)*. Arrows indicate flow direction. Scalebar $400\mu m$

separated by air bubbles (bottom right), but do still have a strong tendency to wet the channel walls. At the chip output no stable droplet structures remain.
It is clear that while the chemistry works, the destabilization of the surfactant is too extreme, which prevent any droplets from maintaining their shape. This effect is only enhanced by the presence of the channel walls, which offer a hydrophobic surface that the oil can wet.

5.3.4 Fusion by Dilution

For a more gentle approach, an alternative to pH induced fusion is investigated. The key element is the surfactant. By slowly diluting the aqueous phase, the NB droplets destabilize, but the oleate is not inactivated completely as with the acid.
To investigate this a diffusive mixer chip is designed and investigated. The chip is designed to take advantage of the fact that smaller molecules diffuse faster than big ones. When two laminar flows (sample and diluter) run along each other, the small surfactant molecules will diffuse along the concentration gradient, while the much bigger droplets are caught in the streamlines. The structure is repeated five times to maximize time for diffusion. The design of the structure is shown in figure 5.34 *(left)*. The structure is based on a simple 2D COMSOL simulation *(right)*, which ensures correct flow of the sample through the chip (illustrated by the red color). Fresh diluter is added at every H-junction to ensure a large concentration gradient.

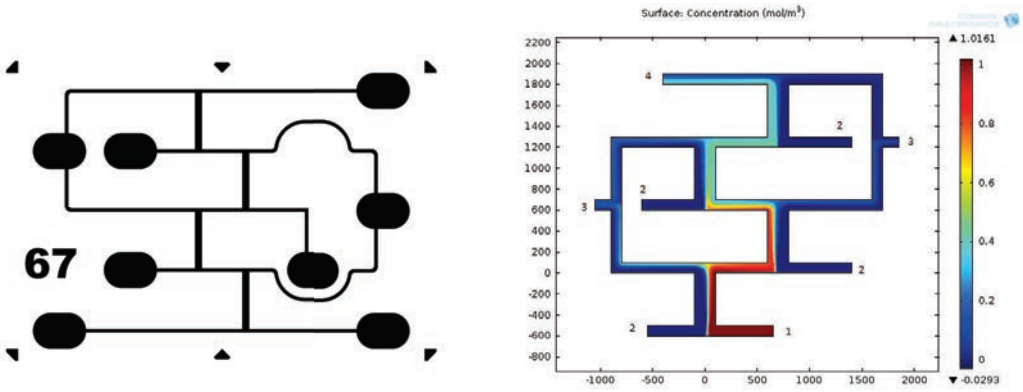

Figure 5.34: Chip design 67 containing five H-junctions (left). 2D COMSOL simulation illustrating dilution of artificial sample *(right)*. Numbers indicate (1) Sample inlet (2) Diffuser inlets (3) Diffuser outlets and (4) Sample outlet.

As the chip has no room for a droplet maker, preformed droplets are injected into the system, along with various concentrations of oleate to determine when fusion starts to occur. Figure 5.35 *(top)* shows the inlet and outlet of the first H-junction with $10mM$ of oleate added. No fusion occurs. When introducing $5mM$ of oleate instead, diffusion starts to occur in the second H-junction. Figure 5.35 *(bottom)* shows two successive frames where droplets start to fuse and wet the wall. Enough surfactant is present to prevent the droplet from completely sticking. Furthermore, not all droplets fuse, indicating that the concentration brings the system to the limit of droplet stability.

To test this approach properly, chip *design* 60 is once again used. Two populations of NB droplets are created (red and blue) and air is introduced to ensure separation. Diluted oleate solutions are added while the pH is monitored. This is because too low pH induces complete fusion, regardless of oleate concentration. At a oleate concentration of $1mM$ ($pH8$), controlled fusion without complete wetting can finally be observed. Figure 5.36 shows six consecutive frames from a video-segment illustrating droplet fusion. Figure 5.37 also shows several fused droplets (purple) further along the meander channel, indicating that droplets have fused but are not wetting the walls. Instead, the droplets flow along with other unfused colored droplets and remain just as stable. Despite the fact that individual droplet fusion has been demonstrated, many droplets still make it through the system without being fused, while others fuse multiple times.

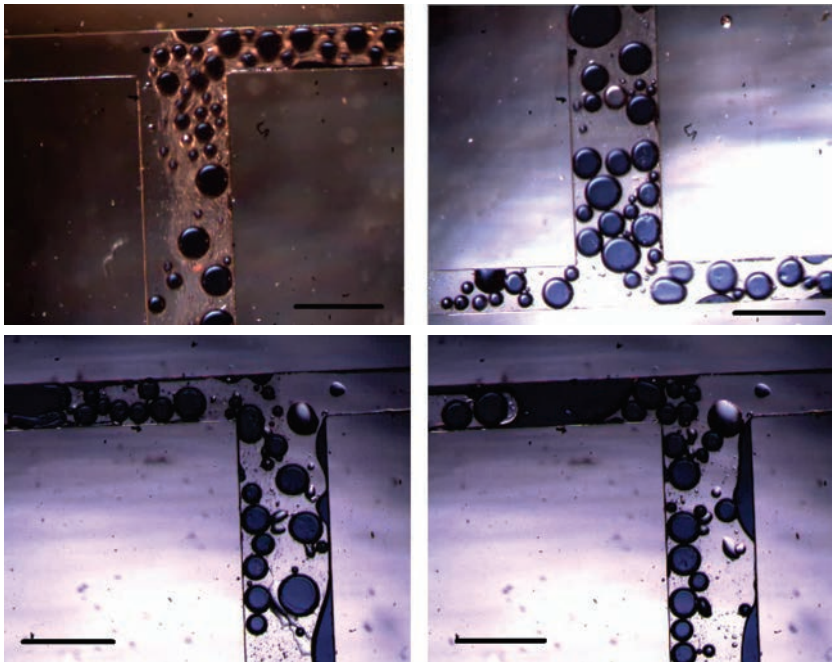

Figure 5.35: Microscope images showing preformed NB droplets in chip 67. Diluter containing $10mM$ oleate *(top)* causes fusion in first H-junction, while $5mM$ oleate *(bottom)* causes slower fusion in the second H-junction. Scalebar $400\mu m$

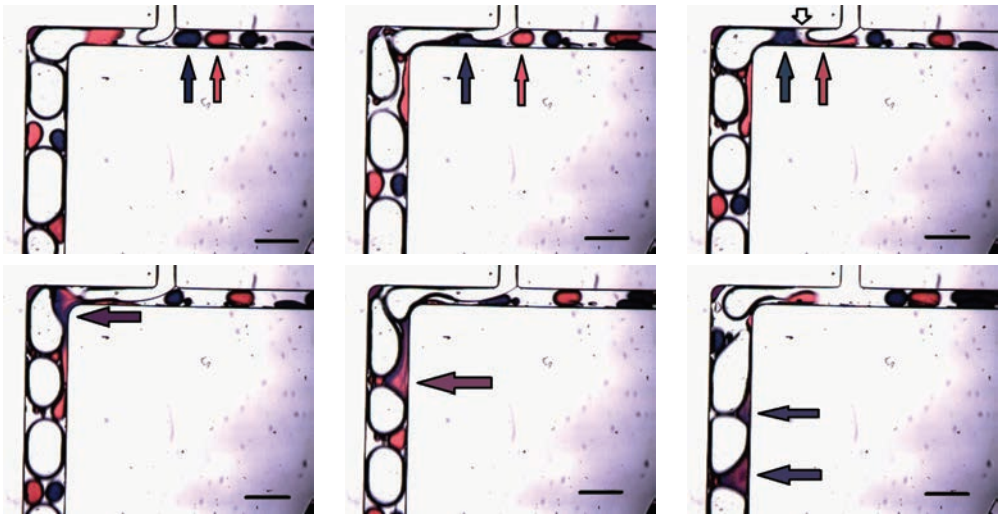

Figure 5.36: Selected video frames showing a fusion event between red and blue NB droplets. Arrows indicate the respective droplets. Scalebar $400\mu m$

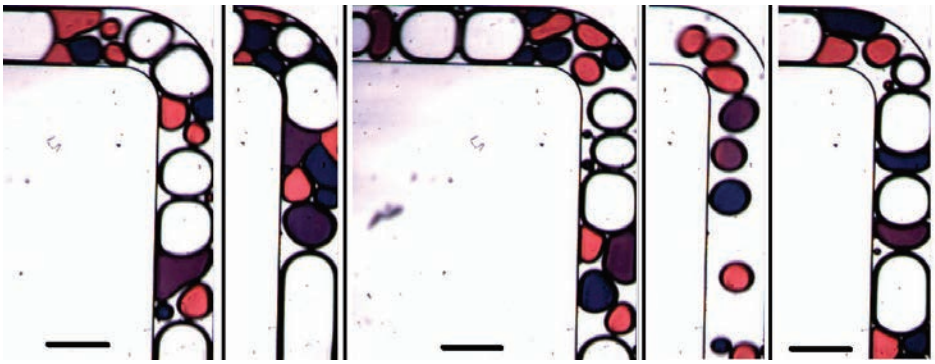

Figure 5.37: Selected microscope images showing fused NB droplets along with unfused ones (red and blue). Scalebars 400μm.

5.4 Droplet Sorting

Another important feature of the integrated microfluidic LOC system for protocell life cycles, is a sorting mechanism. Based on either external inputs (obtained by e.g. FCM), or internal parameters (size, charge etc.), it is desirable to be able to separate droplet populations according to some control values.
The most simple sorting systems are passive in nature and rely entirely on either surface chemistry, geometry [84] (narrow channels that only allow certain size) or other similar mechanics. The main problem with passive systems is the lack of control and flexibility. Both geometry and chemical properties of channel surfaces are intrinsic properties of the chip and not easily changed during operation.
Active systems on the other hand, rely on external inputs, usually in the form of physical forces. These can be either optical [85], electrical [86], mechanical [87] or a range of other options. Some methods require additional features built into the microfluidic system (such as electric fields), while others can manipulated entirely externally (e.g. optical methods).
Asymmetric hydrodynamic focusing is a very simple method that requires no additional modifications to the microfluidic setup and the understanding of hydrodynamic focusing obtained in chapter 2, can easily be adapted here. By having a non-equal side flow rate in a flow focusing junction, the position of the central focused stream can be controlled. Figure 5.38 shows a simple 2D COMSOL simulation where one side flow is five times bigger than the other. Hydrodynamic focusing still takes place, but the focused stream is displayed away from the stronger flow.
A simple chip design is made to test asymmetric focusing for droplet sorting (see figure 5.39). The design contains three inlet channels (*right*) for hy-

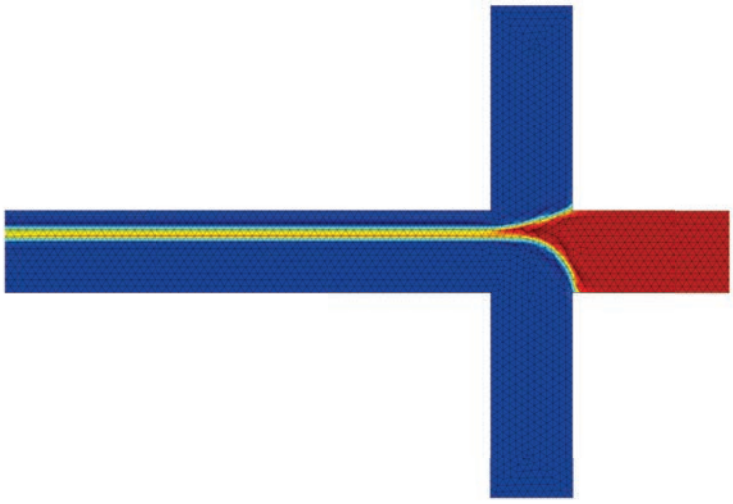

Figure 5.38: 2D COMSOL simulation illustrating asymmetrical flow focusing. Sample flow $30\mu L/min$ and side flows $200\mu L/min$ and $40\mu L/min$. Channels are $200\mu m$ wide.

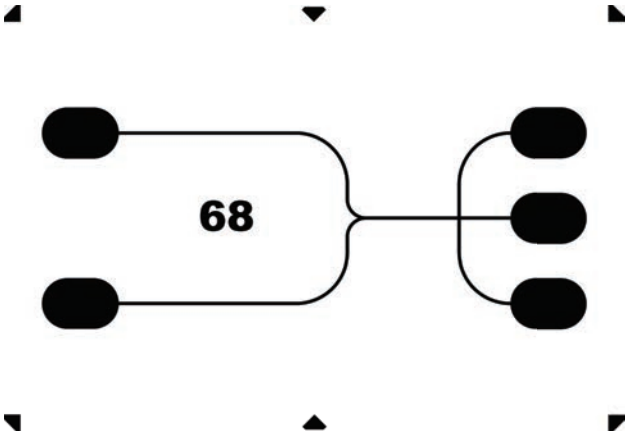

Figure 5.39: Chip design 68 containing a simple y-shaped sorting junction and one flow focusing droplet formation junction.

drodynamic focusing, and two outlets (*left*). The idea is that by externally changing flow rates in the side channels, the central focused flow (which contains droplets) can be directed into either of the two outlets.
Pre-collected NB droplets are used for sample flow, while the two side flows contains $40mM$ oleate to ensure the droplets remain stable. All three inlets are controlled independently via three syringe drivers. First, the ability to control and switch flows are tested.

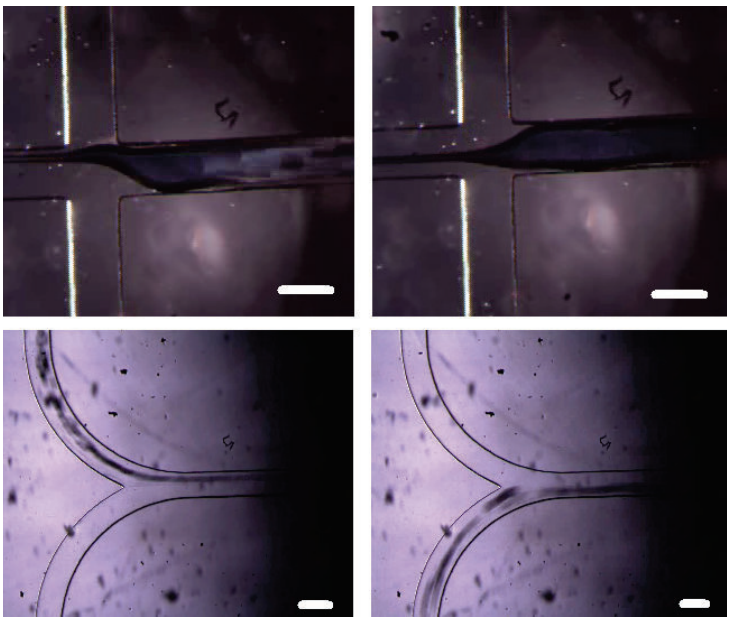

Figure 5.40: Selected video frames showing flow switching using preformed NB droplets. Focusing junction *(top)* and sorting y-junction *(bottom)*. Assymetrical focusing switched between *left* and *right* takes around 100 frames, which equals $2s$.

Figure 5.40 shows two sets of frames from a video-segment (focusing junction *top*, sorting junction *bottom*). The sample flow is only $3\mu l/min$, while side flows are $5\mu l/min$ and $50\mu l/min$, respectively. This clearly shows that switching is indeed possible. The *left* and *right* pair of frames marking the transition from one output channel to the other are roughly $2s$ apart. Going to higher ratios (up to $5\mu L/min$ vs $80\mu L/min$) is also possible and does decrease this transition time slightly. The droplet movement does however become to fast to track on the CCD. A major issue of the method is, however, that transition is continuous, which might cause issues since droplets continue to flow into either channel until the new asymmetric flow is established.

In order to better evaluate the sorting mechanism, some of the obtained video segments have been investigated using the droplet tracking method as earlier. The first video shows symmetric focusing with both side flows at $10\mu l/min$. For comparison, the highly asymmetric flow shown in figure 5.40 is analyzed. Figure 5.41 shows histograms of droplet sizes collected from the $30s$ videos, measured for top and bottom channel respectively. For the equal flows *(left)*, the total droplet count is 3548 for the top channel and 2822 for the bottom. For the strongly shifted flow *(right)*, the count is 628 for the top channel and 3652 for the bottom. The results indicate that the method is

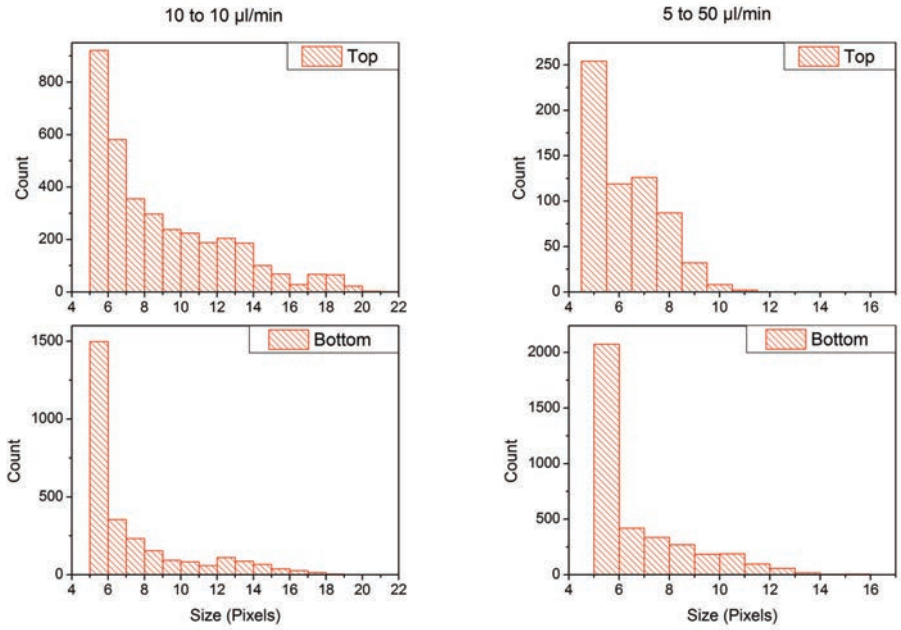

Figure 5.41: Histograms showing droplet size distributions in upper and lower arm of the y-junction for symmetrical flow ($10 : 10\mu L/min$ - *left*) and asymmetrical ($5 : 50\mu L/min$ - *right*) flow.

not entirely reliable, as around 17% of the droplets still pass into the wrong outlet, even in a highly asymmetrically focused flow. It is possible that less droplets would end up in the wrong channel at even higher asymmetric ratios, but they are not reliably trackable.
In conclusion, while this sorting method is easy to implement, it is neither precise nor fast enough be properly implemented in an integrated system where, for instance, the FCM setup is capable of measuring around 100 events per second. Faster methods are available in literate and could prove promising in future applications.

Chapter 6

Conclusions and Outlook

In this project the development of a microfluidic optical LOC platform has been developed. The main areas of focus have been LOC chip development, optical and fluidic optimization, which have been used to establish a LOC flow cytometry setup. Measurements on polymer beads and microbial samples have been performed. Furthermore, a range of LOC devices have been developed for oil droplet based protocells. Here, droplet formation, splitting, fusion and sorting have been demonstrated as well as successful distinction of droplet populations in the flow cytometry setup.
In the following sections, the main results in these areas are summarized.

6.1 LOC Development

The first major goal of this is to develop a fast and flexible microfluidic LOC platform. A novel approach to photolithographic masks has been demonstrated by the use of photonegative films. Developed under correct conditions, contrast ratios near 1 : 1000 are reached while UV transmission is maintained at over 70%. By using these masks in a standard clean-room process, SU8 structures with feature sizes down to $50\mu m$ have been demonstrated.
By using these SU8 master structures in a simple replication process, PDMS microfluidic devices have been realized. As a result of flexible mask design and rapid prototyping of PDMS chips, LOC devices can be realized from initial design in the course of a single day.
Using the novel chip-chuck interconnection system, the LOC device can be interfaced to a full fluidic setup, both easily and fast. The system utilizes the soft PDMS material to create simple push-fit water tight seals.

6.1.1 Optical System

In extension of the LOC system, an optical detection system has been established to create a sensing platform in the form of a microfluidic flow cytometer. This is realized by molding guiding channels directly into the chip and using these to position optical fibers directly near the measurement volume of the sample. The fibers serve to excite and detect via fluorescence.
Detection of laser induced fluorescence signals have been optimized by several approaches. First, it has been demonstrated that output fibers angled with respect to the optical axis are preferable for light collection as less laser light is directly coupled from the laser source. By introducing liquids with matching refractive index to PDMS, waveguiding of fluorescent signals has also been demonstrated, most successfully for gelatin solutions.
Finally, it has been demonstrated that by adding an adjustable pinhole in the optical detection block, unwanted high angle scattered laser light can be eliminated, preventing false signals in the PMT.

6.1.2 Fluid Dynamics

To properly control liquid flows in the developed microfluidic LOC system, laminar flows and hydrodynamic focusing have been investigated. Both experimental results and FEM simulations show a non-linear relation between flow focusing and flow ratios. It has also been demonstrated that the angle between inlet channels in the flow focusing junction influences both the flow focusing effect and the long range behavior of the focused flow. Finally, 3D FEM simulations are presented that suggest a non-uniform flow profile under high flow rate conditions ($Re > 100$).

6.2 Flow Cytometry

Using the developed microfluidic LOC FCM setup, a number of successful measurements have been presented, demonstrating the systems ability to distinguish a range of different samples based on fluorescence and light scattering. Firstly, measurements on PS bead mixtures have demonstrated the ability to distinguish different artificial microparticles. Further measurements have additionally demonstrated distinction of beads with different levels of fluorescence.
Measurements on biological samples have also been presented, demonstrating distinguishable results from mixtures of both yeast and listeria with fluorescent PS beads. Lastly, preliminary experiments on purely biological samples

have been presented, along with possible suggestions for improving the detection limit for fluorescence of the current setup.

6.3 Droplet Based Protocells

As an extension of the microfluidic LOC platform, a wide range of devices have been developed for investigations on oil droplet based protocells. Formation of Nitrobenzene droplets has been described theoretically and demonstrated in both dish experiments and microfluidic devices, where a certain amount of surfactant is required to produce stable droplets. Investigations on mono-disperse populations are presented and show interesting relations between droplet sizes and flow focusing conditions.
Droplet splitting is an essential step of the protocell life cycle and has been demonstrated as well. For certain systems, splitting can be induced by altering the surface tension as is demonstrated in dish experiments and discussed thermodynamically. For more stable droplets, mechanical splitting in T-junction structures haw been demonstrated with success, showing a higher splitting ratio for faster flowing cross flows.
Droplet fusion is proposed as a suitable mechanism for delivering resources to protocell systems and has been demonstrated in pH dependent systems. By lowering the pH of the system, the surfactant is destabilized and fusion occurs. This has been demonstrated in both dish experiments and in the microfluidic LOC system. To prevent extensive wall wetting and continuous fusion, air bubbles are demonstrated to function as separators and thereby compartmentalize smaller droplet populations. Finally, controlled droplet fusion is demonstrated on-chip using low surfactant concentration flows to slowly destabilize the droplets.
The final droplet based LOC device demonstrated is a simple flow sorting chip, which uses asymmetrical flow focusing the guide flows of droplets into the desired channels. While the principle of the sorting works, the process has a rather slow reaction time and thus has limited use as an active sorting mechanism.

6.4 Outlook

For further development of the microfludic LOC system it would be interesting to expand its capabilities by introducing a multicomponent chip system, consisting of simple individual chip elements, internally connected. This can be done either by multiple chip-chucks and thin polymer tubes, or alternatively a larger chip-chuck where several chucks can be mounted and interconnected freely with u-shaped steel tubes, much like an electronic breadboard. A potential use for such a system could be FCM investigations on bacterial samples, with separate chips for cell staining, enrichment, incubation and finally flow cytometry measurements. A system is currently under development that utilizes immuno-magnetic-separation (IMS) to trap and stain biological samples on a microfluidic chip containing $1m$ long channels.
Further improvements on the optical setup have mostly already been discussed and are tied closely to the results of the FCM measurements on biological samples. A logarithmic amplifier on the PMT signal would improve the dynamic range on the setup greatly, while in-plane lenses would be interesting to revisit with alternative production methods, as they are expected to improve the amount of light collected considerably.
For further advancement in the microfluidic based protocell life cycle, some improvements could prove very helpful. While both droplet formation and splitting are well understood and characterized, droplet fusion could still be developed further. Using the adapted design to form complex foams [83] together with the fusion dilution scheme, truly organized and well behaved droplet fusion is believed to be obtainable. Once such a system is established, a range of interesting experiments can be conducted, investigating chemical reactions on a droplet to droplet basis.
On a slightly longer timescale, true life cycle implementation should be possible. This can be done using the above mentioned multicomponent LOC system, with each separate device fulfilling specific functions such as formation, fusion, splitting, detection and sorting (as discussed in the chapter 1). The main missing link in this context is the droplet sorting, for which a better concept must be developed. Such a system could be based on electric fields as some experience with electrode implementation on LOC devices is already available.

Appendix A

Publication List

The list is ordered chronologically by date of publication.

- Chip-Chuck: Push-fit modular opto-microfluidic system, J. Hoyland, C. Kunstmann-Olsen and H.G. Rubahn, Danish Patent Application, 2010.
- Influence of geometry on hydrodynamic focusing and long-range fluid behavior in PDMS microfluidic chips, C. Kunstmann-Olsen, J.D. Hoyland and H.G. Rubahn, Microfluidics and Nanofluidics, 12: 795-803, 2012.
- Simple photolithographic rapid prototyping of microfluidic chips, Microelectronic Engineering, MNE 2011 Special Issue, *Accepted*.
- Modular Microfluidic droplet based Protocell life cycle, C.Kunstmann-Olsen, M. Hanczyc, J.D. Hoyland, H.G. Rubahn and S. Rasmussen, *In preparation*.
- Index matching and waveguiding of fluorescent and scattered light in PDMS microfluidic flow cytometer, C.Kunstmann-Olsen, J.D. Hoyland and H.G. Rubahn, *In preparation*.
- High-efficiency immunomagnetic separation of bacterial cultures in fractal microfluidic structures, J.D. Hoyland, C. Kunstmann-Olsen, J. Lenke, H. Erdmann and H.G. Rubahn, Special Scandinavian Issue - Lab Chip, *In preparation*
- Fluorescence diffusion reduction with ZnO coatings in PDMS microfluidic chips, S. Habouti, J. Lenke, C. Kunstmann-Olsen, J.D. Hoyland, M. Es-Souni, H. Erdmann and H.G. Rubahn, *In preparation*

Bibliography

[1] S. Rasmussen & L. Chen & M. Nilsson & S. Abe. Bridging nonliving and living matter. *Artificial Life*, 9:269–316, 2003.

[2] John Vardalas. Twists and turns in the development of the transistor.

[3] G. E. Moore. *Electronics*, 38:114, 1965.

[4] S.C Terry & J.H. Jerman & J.B. Angell. A gas chromatographic air analyzer fabricated on a silicon wafer. *IEEE Transactions on Electron Devices*, 26:1880–1886, 1979.

[5] A. Manz & N. Graber & H. Widmer. Miniaturized total chemical analysis systems: a novel concept for chemical sensing. *Sensors and Actuators*, B1:244–248, 1990.

[6] J.J. Agrestia & E. Antipovc & A.R. Abatea & K. Ahna & A.C. Rowata & J.-C. Barete & M. Marquezf A.M. Klibanovc & A.D. Griffithse & D.A. Weitz. Ultrahigh-throughput screening in drop-based microfluidics for directed evolution. *PNAS*, 107:4004–4009, 2009.

[7] M.A. Burns & B.N. Johnson & S.N. Brahmasandra & K.Handique & J.R. Webster& M.Krishnan & T.S. Sammarco & P.M. Man & D. Jones & D. Heldsinger & C.H. Mastrangelo & D. T. Burke. An integrated nanoliter dna analysis device. *Science*, 282:484–487, 1998.

[8] Pieter Telleman Oliver Geschke, Henning Klank. *Microsystem Engineering of Lab-On-A-Chip Devices*. Wiley-VCH Verlag GmbH, 2008.

[9] D.C Duffy & J.C.McDonald & O.J. A. Schueller & G.M. Whitesides. Rapid prototyping of microfluidic systems in poly(dimethylsiloxane). *Analytical Chemistry*, 70:4974–4984, 1998.

[10] Malcolm. P. Stevens. *Polymer Chemistry - An Introduction*. Oxford University Press, 3. edition, 1999.

[11] J.C. McDonald & G.M. Whitesides. Poly(dimethylsiloxane) as a material for fabricating microfluidic devices. *Accounts of Chemical Research*, 35:491–499, 2002.

[12] B.H. Jo & L.M. van Lerberghe & K.M. Motsegood & D.J. Beebe. Three-dimensional micro-channel fabrication un pdms elastomer. *Journal of Microelectrochemical Systems*, 9:76–81, 2000.

[13] S.K Sia & G.M. Whitesides. Microfluidic devices fabricated in poly(dimenthylsiloxane) for biological studies. *Electrophoresis*, 24:3563–3576, 2003.

[14] J.N. Lee & C. Park & G.M. Whitesides. Solvent compatibility of poly(dimethylsiloxane)-based microfluidic devices. *Analytical Chemistry*, 75:6544–6554, 2003.

[15] Richard A. Zsigmondy. Properties of colloids. Nobel Lecture, December 1926.

[16] A. Moldovan. Photo-electric technique for the counting of microscopical cells. *Science*, 80:188–189, 1934.

[17] Howard M. Shapiro. *Practical Flow Cytometry*. Wiley-Liss, 4. edition, 2003.

[18] D. Huh & W. Gu & Y. Kamotani & J.B Grotberg & S. Takayama. Microfludics for flow cytometric analysis of cells and particles. *Physiological Measurement*, 26:R73–R98, 2005.

[19] C. Kunstmann-Olsen & J.D. Hoyland & H.G Rubahn. Influence of geometry on hydrodynamic focusing and long-range fluid behavior in pdms microfluidic chips. *Microfluidics and Nanofluidics*, 12:795–803, 2012. 10.1007/s10404-011-0923-1.

[20] J. Comas-Riu & N. Rius. Flow cytometry applications in the food industry. *Journal of Industrial Microbilogy and Biotechnology*, 36:999–1011, 2009.

[21] M.D. Zordan & M. M.G. Grafton & G. Acharya & L.M. Reece & C.L. Cooper & A.I. Aronson & K.Park & J.F. Leary. Detection of pathogenic e. coli o157:h7 by a hybrid microfluidic spr and molecular imaging cytometry device. *Cytometry A*, 75A:155–162, 2009.

[22] Stephen Hawking. *The Universe in a Nutshell*. Bantam Spectra, 2001. Quoted in.

[23] P.A. Monnard & D.W. Deamer. Nutrient uptake by protocells: A liposome model system. *Origins of Life and Evolution of Biospheres*, 31:147–155, 2001.

[24] M.M Hanczyc & J.W. Szostak. Replicating vesicles as models of primitive cell growth and division. *Chemical Biology*, 8:660–664, 2004.

[25] M.M. Hanczyc & S.M. Fujikawa & J.W. Szostak. Experimental models of primitive cellular compartments: Encapsulation, growth, and division. *Science*, 302:618–622, 2003.

[26] Stephen D. Senturia. *Microsystem Design*. Kluwer Academic Publishers, 2002.

[27] MicroChem. *SU-8 2000, Permanent Epoxy Negative Photoresist, Processing Guidelines*, 2012.

[28] Michael Langford. *Basic Photography*. Focal Press, 7. edition, 2000.

[29] J.D. Hoyland & C. Kunstmann-Olsen & H.G. Rubahn. Simple photolithographic rapid prototyping of microfluidic chips. *Microelectronic Engineering*, 2012. Accepted.

[30] L. St Clair. *MEMSCYCLOPEDIA.ORG - SU-8: Thick Photo-Resist for MEMS*. http://memscyclopedia.org/su8.html, 2012.

[31] Dow Corning. *Information about Dow Corning Brand Silicone Encapsulants*, 2012.

[32] J.Hoyland & C. Kunstmann-Olsen & H.-G. Rubahn. Microfluidic chip and connector, 2010.

[33] J.M.K. Ng & I. Gitlin & A.D. Stroock & G.M. Whitesides. Components for inetraged poly(dimenthylsiloxane) microfluidic systems. *Electrophoresis*, 23:3461–3473, 2002.

[34] M.L. Chabinyc & D.T. Chiu & J. C. McDonald & A.D. Stroock & J.F. Christian & A.M. Karger & G.M. Whitesides. An integrated fluorescence detection system in pdms for microfluidic applications. *Analytical Chemistry*, 73:4491–4498, 2001.

[35] Z. Wang & J. El-Ali & M. Engelund & T. Gotsaed & I. R. Perch-Nielsen & K. B. Mogensen & D. Snakenborg & J. P. Kutter & A. Wolff. Measurements of scattered light on a microchip flow cytometer with integrated polymer based optical elements. *Lab Chip*, 4:372–377, 2004.

[36] S. Camou & H. Fujita & T. Fujii. Pdms 2d optical lens integrated with microfluidic channels: principle and characterization. *Lab Chip*, 3:40–45, 2003.

[37] K.B. Mogensen & J.El-Ali & A. Wolff & J.B. Kutter. Integration of polymer waveguides for optical detection in microfabricated chemical analysis systems. *Applied Optics*, 42:4072–4079, 2003.

[38] F. Schneider & J. Draheim & R. Kamberger & Ulrike Wallrabe. Process and material properties of polydimethylsiloxane (pdms) for optical mems. *Sensors and Actuators A: Physical*, 151:95–99, 2009.

[39] A.K. Manocchi, P. Domachuk, F.G. Omenetto, and H. Yi. Factile fabrication of gelatin-based biopolymeric optical waveguides. *Biotechnology and Bioengineering*, 103:725–732, 2009.

[40] Miles V. Klein & Thomas E. Furtak. *Optics*. Wiley, 2. edition, 1986.

[41] Richard P. Feynman. *The Feynman Lectures of Physics Vol II*. Addison-Wesley, 1694.

[42] I. Moreno & J. J. Araiza & M. Avendano-Alejo. Thin-ïňĄlm spatial ïňĄlters. *Optics Letters*, 30:914–916, 2005.

[43] A.A. Friesem & U. Levy. Parallel image transmission by a single optical fiber. *Optics*, 2:133–135, 1978.

[44] Henrik Bruus. *Theoretical Microfluidics*. Oxford University Press, 2008.

[45] K. S. Surana & S. Allu & P. W. Tenpas & J. N. Reddy. k-version of finite element method in gas dynamics: higher-order global differentiability numerical solutions. *International Journal for Numerical Methods in Engineering*, 69:1109–1157, 2007.

[46] K. Avila & D. Moxey & A. de Lozar & M. Avila & D. Barkley & B. Hof. The onset of turbulence in pipe flow. *Science*, 333:192–196, 2011.

[47] Christie John Geankoplis. *Transport Processes and Separation Process Principles*. Prentice Hall, 4. edition, 2003.

[48] D. Gobby, P. Angeli, and A. Gavriilidis. Mixing characteristics of t-type microfluidic mixers. *Journal of Micromechanics and Microengineering*, 11(2):126–132, March 2001.

[49] Jun Yang, Xitian Pi, Liguo Zhang, Xiangshao Liu, Jing Yang, Yi Cao, Wenxian Zhang, and Xiaolin Zheng. Diffusion characteristics of a t-type microchannel with different configurations and inlet angles. *Analytical Sciences*, 23(6):697–703, June 2007.

[50] G. B. Lee, C. C. Chang, S. B. Huang, and R. J. Yang. The hydrodynamic focusing effect inside rectangular microchannels. *Journal of Micromechanics and Microengineering*, 16(5):1024–1032, May 2006.

[51] David R. & Kennedy Matthew J. & Golden Joel P. & Ligler Frances S. Nasir, Mansoor & Mott. Parameters affecting the shape of a hydrodynamically focused stream. *Microfluidics and Nanofluidics*, 11(2):119–128, August 2011.

[52] Y. Yamaguchi & F. Takagi & K. Yamashita & H. Nakamura & H. Maeda. 3-d simulation and visualization of laminar flow in a microchannel with hair-pin curves. *American Institute of Chemical Engineers Journal*, 50:1530–1535, 2004.

[53] G. B. Lee, C. C. Chang, S. B. Huang, and R. J. Yang. The hydrodynamic focusing effect inside rectangular microchannels. *Journal of Micromechanics and Microengineering*, 16(5):1024–1032, May 2006.

[54] V. Ramaswamy & V.M Cresence & J.S. Rejitha & M.U. Lekshmi & K.S. Dharsana & S.P. Prasad & H.M. Vijila. Listera - review of epidemiology and pathogenesis. *Journal of Microbiological Immunological Infect.*, 40:4–13, 2007.

[55] C.C. Chang & Z.X. Huang & R.J. Yang. Three-dimensional hydrodynamic focusing in two-layer pdms microchannels. *Journal of Micromechanics and Microengineering*, 17:1749–1486, 2007.

[56] C.N. Baroud & F. Gallaireb & R. Danglaa. Dynamics of microfluidic droplets. *Lab Chip*, 10:2032–2045, 2010.

[57] D.T. Papageorgiou. On the breakup of viscous liquid threads. *Physics of Fluids*, 7:1529–1545, 1994.

[58] T. Thorsen & R.W. Roberts & F.H. Arnold & S.R. Quake. Dynamic pattern formation in a vesicle-generating microfluidic device. *Physical Review Letters*, 86:4163–4166, 2001.

[59] P. Garstecki & M.J. Fuerstmann & H.A. Stone & G.M. Whitesides. Formation of droplets and bubbles in a microfluidc t-junction - scaling and mechanism of break-up. *Lab Chip*, 6:437–446, 2006.

[60] P.Guillot & A.Colin. Stability of parallel flows in a microchannel after a t-junction. *Physical Review E*, 72:066301–1–4, 2005.

[61] M.D. Menech. Modeling of droplet breakup in a microfluidic t-shaped junction with a phase-field model. *Physical Review E*, 73:031505, 2006.

[62] V. van Steijna & M.T. Kreutzerb & C.R. Kleijna. u-piv study of the formation of segmented flow in microfluidic t-junctions. *Chemical Engineering Science*, 62(24):7505–7514, 2007.

[63] S. L. Anna & N. Bontoux & H. A. Stone. Formation of dispersions using flow-focusing in microchannels. *Applied Physics Letters*, 82:364–366, 2003.

[64] R. Dreyfus & P. Tabeling & H. Willaime. Ordered and discordered patterns in two phase flows in microchannels. *Physical Review Letters*, 90:144505, 2003.

[65] T. Cubaud & T.G. Mason. Capillary threads and viscous droplets in square microchannels. *Physics of Fluids*, 20:053302, 2008.

[66] P. Garstecki & H. A. Stone & G. M. Whitesides. Mechanism for flow-rate controlled breakup in confined geometries: A route to monodisperse emulsions. *Physical Review Letters*, 94:164501, 2005.

[67] B. Dollet & W.van Hoeve & J.P. Raven & P. Marmottant & M. Versluis. Role of the channel geometry on the bubble pinch-off in flow-focusing devices. *Physical Review Letters*, 3:034504, 2008.

[68] D. Funfschilling & H. Debas & H. Z. Li & T. G. Mason. Flow-field dynamics during droplet formation by dripping in hydrodynamicfocusing microfluidics. *Physical Review E*, 80:15301, 2009.

[69] W. Lee & L. M. Walker & S. L. Anna. Role of geometry and fluid properties in droplet and thread formation processes in planar flow focusing. *Physics of Fluids*, 21:032103., 2009.

[70] William M. Haynes, editor. *CRC Handbook of Chemistry and Physics*. CRC Press, 2011.

[71] Sigma Aldrich Inc. *Triton X-100 Product Information*.

[72] A. D. McNaught and A. Wilkinson. *IUPAC - Compendium of Chemical Terminology*. Blackwell Scientific Publications, 1997.

[73] H.W. Zhu & N.G. Zhang & R.X. He & S.Z. Li & S.S. Guo & W. Liu & X.Z. Zhao. Controllable fission of droplets and bubbles by pneumatic valve. *Microfluidics and Nanofluidics*, 10:1343–1349, 2011.

[74] Paolo Sibani & Steen Rasmussen. Oliedraabers termodynamik. Lecture Notes for FY520 course on Thermodynamics, 2011.

[75] M.M. Hanczyc & T. Toyota & T. Ikegami & N. Packard & T. Sugawara. Fatty acid chemistry at the oil-water interface: Self-propelled oil droplets. *Journal American Chemical Society*, 129:9386–9391, 2007.

[76] T. Moritani & M. Yamada & M. Seki. Generation of uniform-size droplets by multi-step hydrodynamic droplet division in microfluidic circuits. *Microfluidics and Nanofluidics*, 11:601–610, 2011.

[77] E. Fradet & C. McDougall & P. Abbyad & R. Dangla & D. McGloin & C.N. Baroud. Combining rails and anchors with laser forcing for selective manipulation within 2d droplet arrays. *Lab Chip*, 11:4228–4234, 2011.

[78] M. Zagnoni and J.M. Cooper. On-chip electrocoalescence of microdroplets as a function of voltage, frequency and droplet size. *Lab Chip*, 9:2652–2658, 2009.

[79] W. Wang & C. Yang & C.M. Li. On-demand microfluidic droplet trapping and fusion for on-chip static droplet assays. *Lab Chip*, 9:1504–1506, 2009.

[80] M. Chabert & K.D. Dorfman & J.-L. Viovy. Droplet fusion by alternating current (ac) field electrocoalescence in microchannels. *Electrophoresis*, 26:3706–3715, 2005.

[81] J.Q. Yu A.Q. Liu J.B. Zhang Z.G. Li, K. Ando and C.D. Ohl. Fast on-demand droplet fusion using transient cavitation bubbles. *Lab Chip*, 11:1879–1885, 2011.

[82] J. Thiele A.R. Abate D.A. Weitz T. Liu, S. Seiffert and W. Richtering. Non-coalescence of oppositely charged droplets in ph-sensitive emulsions. *PNAS*, 109:384–389, 2010.

[83] M. Hashimoto & P. Garstecki & G.M. Whitesides. Synthesis of compostite emulsions and complex foams with the use of microfluidic flow-focusing devices. *Small*, 3:1792–1802, 2007.

[84] Y.C.Tan & J.S Fisher & A. Lee & V. Cristini & A.P. Lee. Design of microfluidic channel geometries for the control of droplet volume, chemical concentration, and sorting. *Lab Chip*, 4:292–298, 2004.

[85] C. McDougall & E. Fradet & C.N. Baroud & D. McGloin. Optical manipulation of "drops on rails" in two dimensional microfluidic devices. *Proceedings of SPIE*, 8097:809710, 2011.

[86] B. Ahn & K. Lee & R. Louge & K.W. Oh. Concurrent droplet charging and sorting by electrostatic actuation. *Biomicrofluidics*, 3:044102, 2009.

[87] J. Shemesh & A. Bransky & M.Khoury & S. Levenberg. Advanced microfluidic droplet manipulation based on piezoelectric actuation. *Biomedical Microdevices*, 12:907–914, 2010.